Synthetic Jet Flow and Heat Transfer for Electronics Cooling

A DISSERTATION
SUBMITTED TO THE FACULTY OF THE GRADUATE SCHOOL
OF THE UNIVERSITY OF MINNESOTA
BY

Longzhong Huang

IN PARTIAL FULFILLMENT OF THE REQUIREMENTS
FOR THE DEGREE OF
DOCTOR OF PHILOSOPHY

Dr. TERRENCE W. SIMON, ADVISOR
Dr. TIANHONG CUI, CO-ADVISOR

May, 2014

Acknowledgements

First of all, I would like to thank my advisors, Professor Terrence W. Simon and Professor Tianhong Cui for their enthusiastic guidance and support through my whole Ph.D study. I appreciate their advice on my research and life.

I would also like to thank Professors Richard J. Goldstein, Wojciech Lipinski, and Krishnan Mahesh serving in my committee.

I am grateful to my colleagues Youmin Yu, Min Zhang, Smita Agrawal, Taiho Yeom, Tao Zhang, Congshun Wang, and Xuelin Zhu who worked together for a long time.

Additionally, thanks go to Defense Advanced Research Projects Agency (DARPA) for their financial support and Minnesota Supercomputing Institute (MSI) at the University of Minnesota for their computational resources and technical support.

Finally, I would like give my gratitude to my parents for their endless support.

Abstract

The progressive increase of heat dissipation from modern electronics requires more and more powerful cooling systems. Various cooling technologies have been developed such as liquid cooling, micro-channel cooling, and active cooling. The present study focuses on applying a unique device called a synthetic jet to cool electronics. A synthetic jet is able to generate an unsteady flow with a simple structure that makes it effective in convective heat transfer. This study provides both practical and fundamental view of synthetic jets in the application of electronics cooling.

A mock-up synthetic jet is fabricated to study heat transfer and fluid mechanics of synthetic jet cooling. The scaled synthetic jet is geometrically and dynamically similar to the actual jet. The heat transfer performance characteristics of a synthetic jet impinging on a fin are tested with different operating frequencies and with different orifice shapes. Flow visualizations and detail flow field measurements of the impinging synthetic jet flow are documented to support the heat transfer experiment. The optimized parameters obtained from the scaled experiment are applied to the actual synthetic jet design. The actual synthetic jet is realized using a piezoelectric stack and applied on a cooling system based on a full-sized heat sink module. The cooling performance of the whole system is documented. The noise characteristics of the actual synthetic jet is tested and analyzed. A muffler with optimized parameters is found and used for noise reduction. Numerical simulation is used to find the optimal design for the synthetic jets. The computation is realized by the commercial software ANSYS Fluent. The numerical model is verified by

comparing the computational results with experimental results. A parametric study of heat transfer performance of synthetic jet cooling is documented.

Table of Contents

List of Tables

List of Figures

Nomenclature

a	peak-to-peak amplitude (mm)
A	total convective heat transfer area (m2)
cp	specific heat of air flow
C	sound speed (m/s)
d	orifice diameter (m)
D	fin tip diameter (m)
f	frequency of diaphragm movement (Hz)
F	force (N)
h_{avg}	average heat transfer coefficient (W/m^2K)
I	current (A)
K	thermal conductivity (W/m·K)
L	length of the fin (m)
m	Mass (Kg)
Nu	Nusselt number
p	static pressure (Pa)
p_{rms}	root-mean-square pressure (Pa)
p_{ref}	reference pressure (Pa)
P	power (W)
q	heat power input (W)
$\dot{Q}$	volumetric air flow rate
R	radius of the fin (m)

Re	Reynolds number
S	Stokes number
SPL	sound pressure level (dB)
t	time (s)
T	cycle time (s)
TL	transmission loss (dB)
Ts	surface temperature (°C)
Tair	Temperature of ambient air (°C)
U_{avg}	time average velocity during expelling phase (m/s)
U_{max}	spatially averaged peak jet velocity (m/s)
V	voltage(V)
W	width of the fin (m)
z	distance between orifice and fin tip (m)

Greek symbols

μ	dynamic viscosity of fluid ($N \cdot s/m^2$)
ν	kinematic viscosity of fluid (m^2/s)
ρ	density of fluid (kg/m3)
ω	angular velocity (rad/s)
η	efficiency

Subscripts

air_in	air flow at channel inlet
air_out	air flow at channel outlet
avg	average

c	cross section of the copper extension
Cu	copper
dia	diameter
fin_in	fin channel inlet
fin_out	fin channel outlet
jet	synthetic jet
rms	root-mean-square
ref	reference
s	fin surface
x	x-direction
y	y-direction
z	z-direction

Chapter 1 Introduction

Thermal management of electronic devices has become a progressively serious issue for thermal engineers due to miniaturization of electronic components and fast development of integrated circuits that cause the electronics to dissipate higher and higher power. According to Moore's law [1], the number of transistors on an integrated circuit doubles every 18 months and the transistor density is expected to be more than 10^{11} per die [2] by 2020. The anticipated power density will grow exponentially, as silicon microfabrication technology develops. It is estimated that the power dissipation will increase 13 times as the scales decrease from 90 nm to 15 nm [2]. The heat power has to be carried away by cooling devices to maintain the electronics at a temperature that allows the electronics to work properly [3-5].

Traditional steady air cooling systems such as air driven fan and heat sink assemblies have difficulty in dissipating the increasing heat fluxes of modern electronics. The widely-used methods for cooling high heat flux electronics include liquid cooling, micro-channel cooling, and active cooling with their own specific advantages and disadvantages as applied in various fields. Liquid cooling is a very effective cooling technology that is able to remove a high heat flux due to the higher heat conductivity and heat capacity of liquid compared to air [6-18]. As a result, the liquid cooling devices are generally used for electronics with very high heat flux (above 100 W/cm^2). Phase change cooling is one type of liquid cooling that involves liquid phase change to gas phase during the cooling process. The phase change absorbs a large amount of latent heat and

has high heat transfer performance compared to traditional liquid cooling [19-23]. However, cooling devices with liquids require high level of manufacturing to avoid leakage. The implementation of a liquid cooling system is also complex, causing the whole device to be costly compared to air cooled devices. The micro-channel cooling is another popular technology that is able to provide much higher heat transfer area than traditional heat sinks [24-32]. The channel dimension is usually on the micron scale and the total heat transfer area is generally several hundred times that of the traditional heat sink, in the millimeter or centimeter scale. However, the fabrication of micro-channel requires microtechnology or even nanotechnology, such as photolithography, wet etching, hot embossing, and electroplating, which make the micro-channel cooling device expensive. Also, the small scale of the channel dimension makes the pressure drop across micro-channels much higher than in the traditional channel causing higher pumping power.

Active cooling is one of the most interesting cooling technologies that have been developed recently. One type of device agitates or stirs the cooling flow and, thus, to enhances heat transfer. The most two popular active devices are piezoelectric fans and synthetic jets, which have been found to be effective in disturbing the flow and generating turbulence for enhancing heat transfer. A piezoelectric fan is generally composed of a thin plate with piezoelectric material bonded on it that, when energized with a fluctuating voltage, deflects continuously [33-44]. The fan movement generates vortices near its tip that are carried downstream to the surfaces being cooled [33]. This mechanism has been shown to enhance heat transfer to 375% of natural convection values. Kimber et al. [34-36] studied arrays of piezoelectric fans. They demonstrated the

importance of frequency, amplitude and geometry toward cooling performance. Liu et al. [37] studied flat surface cooling with piezoelectric fans. The entrained airflow generated by the piezoelectric fan was shown to be important for heat transfer enhancement. Yu et al. [44-51] studied the heat transfer enhancement of piezoelectric-driven agitators vibrating inside a channel. It was found that the agitator is very effective in agitating the channel flow. The heat transfer enhancement is linear with the peak moving speed of the agitator.

Synthetic jet impingent is another innovative method for active cooling. In a simple structure and with a low power requirement, the synthetic jet can produce unsteady, turbulent impinging flow. A synthetic jet is a zero-net mass-flux device widely used in boundary-layer separation control, jet vectoring, mixing enhancement in combustion, and turbulence generation. Glezer [53-55] is one of the first researchers to systematically study the fluidic characteristics of synthetic jets. Since then, more and more people focused on synthetic jets in different areas. A synthetic jet generally consists of a cavity with a driver attached on one side and an orifice on the opposite side. When the driver moves back and forth, the jet will generate an unsteady flow through the orifice and the flow will move downstream to a surface forming an impinging flow. When the jet is in the ejection cycle, the diaphragm will expel flow out from the orifice and form a vortex near the orifice. If the propulsion is large enough, the vortex will move downstream before the jet orifice flow reverses and starts to suck in flow. Utturkar et al. [56-57] proposed a criterion for the formation of the vortexes. These vortices are found to enhance mixing and turbulence, and thus, to augment heat transfer performance.

Numerous experimental and numerical studies have been conducted in the application of synthetic jets for cooling.

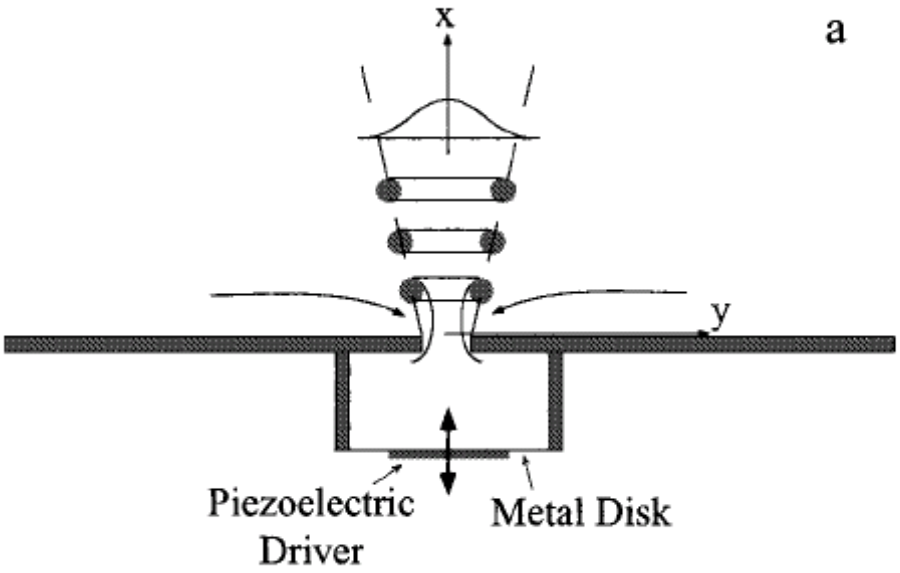

Figure 1.1 Schematics of a synthetic jet [55]

1.1 Experimental Study of Synthetic Jet Cooling

Chaudhari et al. [58] experimentally studied heat transfer characteristics of synthetic jet impingement cooling on a flat, heated wall using a speaker as the actuator [59]. Parametric studies of heat transfer coefficient have been conducted for various parameters, such as orifice diameter (5, 8, 14 mm), orifice thickness (1.6, 2.4, 5 mm), diameter of the cavity (110, 192.5mm), Reynolds number (1150-4180), and actuator frequency (100-350 Hz). It was found that the average heat transfer coefficient increased with an increase of the axial distance between the orifice plate and heated impingement block wall. Beyond a certain point it reduced. The maximum heat transfer coefficient was found to be 143 W/m^2k at the resonance frequency (250 Hz). They found that thinner and

shorter orifice plates exhibited higher heat transfer performance. Using the same test facility, Chaudhari et al. [60] further investigated the effect of orifice shape in synthetic impingement cooling. They conducted experiments by changing the aspect ratio (1-5.25) of rectangular orifices with the same hydraulic diameter (8mm) and found that the rectangular orifice with a higher aspect ratio generally exhibited lower heat transfer performance. Slit orifices with different hydraulic diameters (3.8, 5.58, 8mm) were also tested and average heat transfer coefficients were found to monotonically decrease with an increase of axial orifice-plate distance, a behavior that is different from the that of circular and square orifices. The heat transfer performances of four different orifice shapes (circular, square, rectangular, and slit) were compared and the square orifice shape was found to outperform the others. In addition, Chaudhari et al. [61] explored multiple orifice effects on the improvement of synthetic jet impingement. The heat transfer coefficients of the satellite orifices were measured with a larger circular orifice in the middle with several smaller circular orifices around it. A peak heat transfer coefficient (159 W/m^2k) was obtained with a 5 mm round orifice in the center and eight 3 mm round orifices around it. This was 30% higher than that of a single round orifice in the center. It was found that the heat transfer coefficient was characterized by two peaks with increases of axial distance for the satellite orifice, compared to the single orifice. By adding the fans in the duct, Chaudhari et al. [62] investigated heat transfer performance of synthetic jet impingement in cross flow. The width of the duct had little effect on the heat transfer performance. The maximum heat transfer coefficient (134 W/m^2K) was obtained with a combined cross flow and synthetic jet which was much higher than that with cross flow only, but lower than that with synthetic jet impingement only.

Pavlova et al. [63] fabricated a synthetic jet using a piezo disk with a diameter of 30.2 mm and studied the heat transfer characteristics of jet impingement cooling on a copper disk with a diameter of 12.7 mm and a thickness of 6 mm. It was found that high frequency jets (1200 Hz) were more effective at smaller axial distances between the orifice plate and the copper disk while lower frequency jets (420 Hz) were more effective at larger axial distance. They also compared synthetic jets to the continuous jets at the same Reynolds number and found that synthetic jets were three times more effective in cooling. Using the Particle Image Velocimetry, they claimed that this interesting phenomenon was associated with the accumulation of vortex rings and breakup to smaller structures.

Garg et al. [64] fabricated a meso-scale synthetic jet with a rectangular orifice of hydraulic diameter 0.85 mm. This jet can provide a maximum velocity of 90 m/s at a frequency of 4400 Hz. The cooling performance of the synthetic jet was tested at different frequencies using a square heater with dimensions of 14 mm × 14 mm. They found that the cooling performance did not change much with an increase of driving voltage (50, 70, 90 V_{RMS}). The maximum heat transfer coefficient they obtained was approximately 240 W/m^2K, which was about 10 times that obtained by natural convection. Utturkar et al. [65] studied the heat transfer performance of a pulsating jet with a peak velocity of 45 m/s at a resonance frequency of 4500 Hz. The measured coefficient of performance, COP, of the synthetic jet was found to be about 10.

Arik [66] measured local heat transfer coefficients of high-frequency synthetic jet impingement with a square orifice of 1 mm driven at a resonant frequency of 4500 Hz. It was applied to cool a flat surface. The heat transfer coefficients were found to be between

4 and 10 times those of natural convection. The noise of the jet was found to be as large at 73 dB, but it can be decreased to as low as to 30 dB using abatement techniques [67].

Wang et al. [68] presented a microelectromechanical system (MEMS) device used in the cooling of printed wiring boards (PWB). The device was able to provide a peak jet velocity of 14 m/s with a low actuator power of 60 mW. They [69] further investigated the heat transfer effect of different parameters such as fluidic channel dimensions, jet locations and Reynolds number. It was found that the measured heat transfer coefficient decreased with an increase of distances from the jet exit at different exit widths.

Go and Mongia [70] conducted heat transfer experiments of synthetic jets combined with a cross flow in a long duct. The width of the duct was fixed (85mm) with variable heights (7.5, 10 mm). A 5 × 5 array of 25 heaters was mounted downstream 360 mm from the exit. Each heater was 10 mm × 10 mm square with 5 mm gaps between them. It was demonstrated that the entrainment produced by the synthetic jet played an important role in slowing the bulk flow, causing "dead zones." The cooling performance was found to be enhanced by 25% with the synthetic jet. Qayoum et al. [71] reported detailed flow and heat transfer measurements of interactions between a synthetic jet and a laminar flow. A maximum heat transfer enhancement of 44% was obtained.

Valiorgur et al. [72] explored the mechanisms of synthetic jet impinging heat transfer for a small jet-to-surface spacing of about 2. The synthetic jet was designed with a circular orifice (diameter is 5 mm) driven by a speaker actuator. The average Nusselt number was described as a function of Reynolds number (1000-4300) and the constant value of Nu/Re^n was obtained where the exponent, n, was 0.32 ± 0.06. Gillespie et al. [73]

conducted heat transfer experiments of synthetic jets impinging on a constant flux flat plate (75 mm × 20 mm). The orifice of the synthetic jet was a 1 mm × 25 mm long slot driven at the frequency of 100-600 Hz. It was observed that the spanwise distributions of local time-averaged Nusselt numbers exhibited a Gaussian trend and became more flat with increasing jet-to-surface spacing. The synthetic jet was found to be less effective in the far-field due to the weakness of penetration of the boundary layer.

Mahalingam et al. [74-76] designed a synthetic jet ejector heat sink and tested its thermal performance. Thermal resistance of the heat sink can be reduce from 3.15 °C/W to 0.76 °C/W by adding the synthetic jet. It was found that the heat sink was able to dissipate heater power of 59.2 W with less than a 70°C temperature difference. The heat sink with a synthetic jet was measured to dissipate about 40% more heat compared to steady flow in the channel.

1.2 Numerical study of Synthetic Jet impingement Cooling

In addition to experimental studies on synthetic jets, numerous publications focused on numerical investigation of heat transfer introduced by synthetic jets using Computational Fluid Dynamics (CFD). Jagannatha et al. [77] presented a two-dimensional numerical model to study the unsteady behavior of synthetic jets using the commercial CFD solver Fluent. The oscillating diaphragm was defined as a moving wall with a turbulence model of shear-stress-transport (SST) k-ω. They compared the velocity distribution near the orifice with the experiment and found good agreement. In addition, computational results successfully predicted vortex formation and vortex shedding near the orifice. It was found that heat transfer performance of a synthetic jet was highly

dependent on the amplitude and frequency of diaphragm movement. Compared to natural convection, the heat transfer coefficients were about 20 to120 times higher with the application of synthetic jets. It was also found that synthetic jets outperformed continuous jets in the same Reynolds number with an increase of 30% in the cooling performance.

Navaratnam et al. [78] developed a novel moving-grid methodology to explore the interaction between one single synthetic jet and cross flow. The unsteady behavior of a single, two-dimensional synthetic jet interacting with a turbulent boundary layer was investigated by solving unsteady, Reynolds-averaged Navier-Stokes (RANS) equations. The numerical results were consistent with the experiments by NASA Langley Research Center and this methodology was said to be useful for investigating synthetic jet flow fields. Dghim et al. [79] numerically investigated the effect of the amplitude and frequency of synthetic jets in the application of boundary layer control. They used an unsteady realizable k-ε turbulence model in Fluent and found that the computational formation of the counter-rotating-vortex pair (CVP) was consistent with the experimental results. Zhou and Wang [80] explored the fluidic dynamic characteristics of synthetic jets using a two-dimensional Reynolds-Averaged Navier-Stokes model. It was indicated that the diameter of the orifice is an important parameter for a synthetic jet and the diameter of the cavity affects the decay of the jet centerline velocity. An optimum combination to obtain the maximum jet peak velocity was obtained between the orifice thickness and the cavity depth using this model.

Chandratilleke et al. [81] studied the thermal performance of a synthetic jet microchannel hybrid heat sink using unsteady Reynolds-Averaged Navier-Stokes (RANS) equations with the turbulence model of Shear-Stress-Transport (SST) k-ω. It was found

that the thermal enhancement by the synthetic jet showed an increasing trend with increases of the cross flow velocity. The heat transfer rate with a synthetic jet and cross flow was observed to be 60 times of that with pure natural convection in the channel and 4.3 times that with cross flow only.

Beratlis and Smith [82] proposed cooling of a one-dimensional Vertical Cavity Surface Emitting Laser (VCSEL) using a synthetic jet actuator. A MATLAB optimization routine was used to find the case having the best thermal performance. It was indicated that the optimum configuration results were about 49.2% higher than those of the original prototype for an operating frequency of 350 Hz.

Behera et al. [83] numerically studied heat transfer enhancement using interrupted impinging jets. They tested sine and square wave pulsations with Reynolds numbers of 5130-8560 and frequencies of 25-400. The average Nusselt number of the square wave jet was found to increase by 12% in the stagnation zone and 35% in the wall jet zone, while with a sine wave jet the increase was only 5% in the stagnation zone and 10% in the wall jet zone. It was also observed that the amplitude was more important than the frequency for augmenting heat transfer. A three-dimensional (3-D), unsteady, large eddy simulation (LES) was proposed to study the synthetic jet thermal management of a printed wiring board (PWB) [84].The computational phase-locked velocity was compared to the hot-wire measurements and good agreement was observed. The temperature distributions of the device top surface were also consistent with infrared data. The average heat transfer coefficient was found to be 123 W/m^2K. This CFD model was found to be able to solve synthetic jet flow and heat transfer problem.

Gerlach et al. [85] fabricated a device to dissipate 5 W for a 3-D stacked chip using solid spreaders and synthetic jets in a 27 mm × 38 mm region. It was found that the entrained cool air by the synthetic jet was very helpful for heat transfer and this device can reduce thermal resistance from that of the original design by 40%. Ervas and Baysal [86] computationally carried out a two-dimensional channel flow with synthetic jets impinging on a constant heat flux wall. By changing the position of the synthetic jet along the channel, the maximum heat transfer coefficient of 268.4 W/m^2K was obtained. This was with the synthetic jet in the middle of the channel. They also studied heat transfer performance with two jets in the channel. A peak heat transfer coefficient of 348.6 W/m^2K was found in this case. Timchendo et al. [87-89] studied the flow and thermal fields of a two-dimensional micro-channel cooling system with a synthetic jet actuator using CFD. It was found that the operating frequency of the synthetic jet had very little effect on heat transfer enhancement.

1.3 Acoustics of Synthetic Jet

The agitator plates and synthetic jets have been found to be very effective in enhancing heat transfer. However, these active devices, especially when they are operating at high frequencies, generate noise that adds to the noise of the traditional fans [90]. Seeley et al. [91] measured the sound intensity level of a synthetic jet operating at 3-5 kHz and found levels as high as 80 dB. Arik [67] fabricated a synthetic jet that is able to provide peak air velocities of 90 m/s from a 1.0 mm hydraulic diameter rectangular orifice. The synthetic jet was operated between 3.0 and 4.5 kHz and found to be effective in heat transfer enhancement. They measured the sound pressure levels as large as 73 dB.

These levels are too high and, thus, noise reduction is required for implementation of active devices. Mufflers are considered to be promising devices since they are not only effective in reducing noise levels but they also allow air to pass through the cabinet. Mufflers are widely used in exhaust systems of vehicles to reduce the noise generated by the engines. The principle of a muffler is to generate a reflected sound wave is different in phase from the incident sound wave [92]. The incident and reflected sound waves can cancel each other at specific frequencies. Those frequencies can be targeted by the muffler design. The circular expansion chamber geometry is one simple muffler design. It is generally made of three tubes with different diameters that generate a reflected wave due to a change in cross section of a circular tube [93]. The expansion chamber is easy to fabricate and its performance can be calculated analytically. A number of analytical, numerical, and experimental studies have focused on noise reduction performance with changes in the expansion chamber geometry. EI-Sharkawy et al. [94] investigated the effects of expansion chamber geometry on sound propagation and reflection in circular ducts. They found that the performance of an expansion chamber is greatly affected by the expansion ratio and the noise amplitude-frequency distribution, but is less affected by the chamber length. Kim et al. [95] used a Green's function approach to analyze acoustic characteristics of a circular chamber with inlets and outlets situated at arbitrary locations on the chamber walls. The analytical results were found to agree with experimental results very well. It was also found that this method was easier than a modal expansion method in terms of the convenience of mathematical derivation. Selamet et al. [96] studied analytically, numerically, and experimentally the detailed effects of the chamber length on the acoustic attenuation performance of concentric expansion chambers. They

found that multi-dimensional waves are excited at all frequencies and they decay in a short distance. Denia et al. [97-98] studied the acoustic performance of an elliptical expansion chamber. They found that eccentricity had an important effect on acoustic performance.

In the present study, the synthetic jet is applied to a cooling module for high heat flux electronics. Heat transfer performance of synthetic jet impingement has been studied numerically and experimentally. A mock-up synthetic jet test facility was fabricated for a parametric study of its heat transfer performance and fluid mechanics. The CFD software ANSYS Fluent is used to simulate the synthetic jet flow combined with a channel flow to support the experiment. The fluidic power consumption of a synthetic jet is also studied to find the performance of this active device. The noise issue of the synthetic jet is researched last and some noise reduction methods are proposed and tested.

Chapter 2 Heat Transfer Enhancement of Synthetic Jets for in a Cooling Module

The present study deals with integration of a synthetic jet cooling scheme within a full-sized heat sink module and documentation of its heat transfer performance. An inclined synthetic jet design has been used to avoid the interference of the jet actuation parts with the fan that is used to drive flow through the heat sink channels. Numerical simulation is used to find the optimal design for the synthetic jets. The number of jets has been optimized without much of a penalty on the peak jet velocity. This study serves as a guide for effective integration of synthetic jet technology in cooling systems.

2.1 Experimental Setup

2.1.1 Heat Sink

The experimental set up consists of a 26-channel heat sink with a base area of 114 × 89 mm (4.5 × 3.5 inches). The fin (channel wall) height is 23.6 mm and the fin thickness is 1.0 mm. An induced-draft suction system with a square-headed inlet is mounted on the heat sink to generate cross-flow, drawing air into the sides, through the channels, then out the center section. The setup simulates a fan with actual heat sink assembly used in electronics. The cross flow rate was measured using a laminar flow meter and an inclined manometer. The heat sink was heated from the bottom by a heat spreader with cartridge heaters inserted. A glass fiber insulation block was used to insulate the heat spreader from the bottom. The heat sink module was used to study cooling effects of various active devices such as synthetic jets and agitation plates.

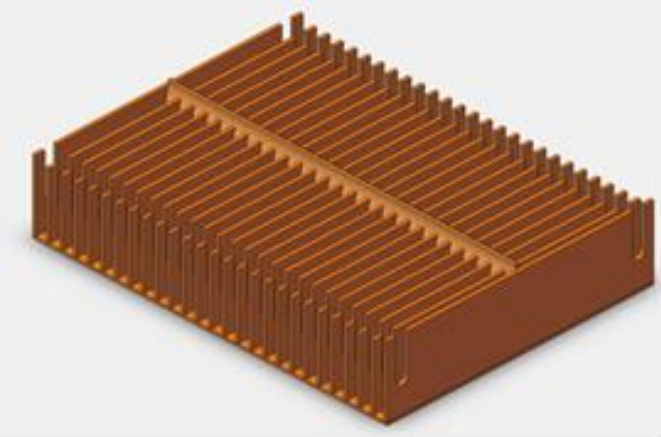

Figure 0-1

Figure 2.1 Heat sink showing finned channels

2.1.2 Synthetic Jet Actuation Mechanism

The jet was actuated using a PITM manufactured piezoelectric stack. The stack was supplied with sinusoidal voltage input from a function generator having 180 volts (root mean square) and a resonance frequency of 700-750 Hz. The piezoelectric stack is held in a bow-actuator that transmits the vibrations to a carbon fiber piston mounted on a diaphragm. The oscillatory motion of the diaphragm over a cavity results in jets of air coming out of the opposite face through a series of orifices. The bow structure is used to amplify the vibration of the piezo stack to obtain the required amplitude for the diaphragm of the synthetic jet.

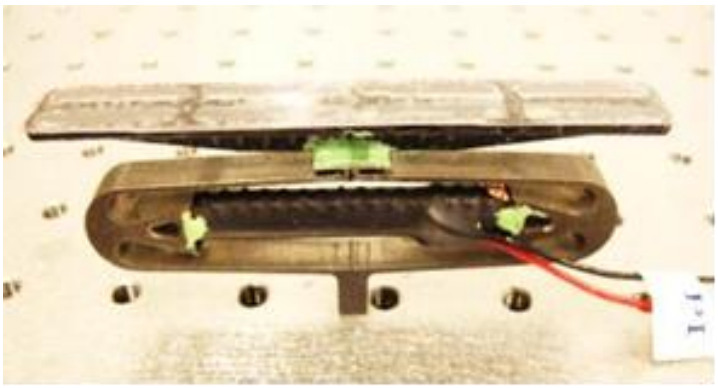

Figure 2.2 Piezo stack, bow actuator and driving piston assembly

2.1.3 Wedge Platform

In the actual cooling module, the jet actuation parts interfere with the cross flow fan, which requires inclining the synthetic jet to avoid interference.

A wedge-shaped platform was designed for mounting the synthetic jet-actuator assembly on the heat sink with the objective of avoiding interference of the synthetic jet actuators with the cross flow fan while maintaining perfect alignment of the actuating piston over the orifices. It was ensured that this scheme raises the height of the through flow fan, minimally. Figure 2.3 shows a schematic description of the cooling module with the synthetic jets mounted in an inclined fashion.

A computational study was done to help understand the effects of various parameters, such as the orifice size and the length of fluid path, on the performance of the synthetic jet. This provided guidance towards designing the wedge in a manner that would keep the velocity losses minimal (compared to a flat cavity case) as peak jet velocity is an important factor for heat transfer performance.

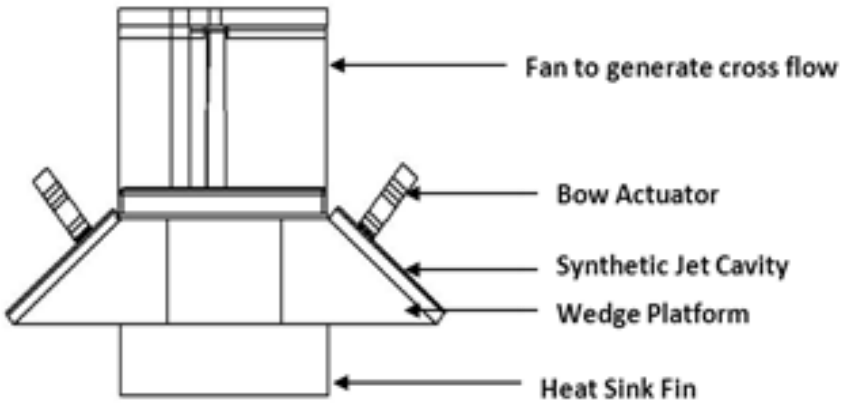

Figure 2.3 Fluid path within the wedge showing the jet channel and orifice; above is the cavity and below is the module channel section.

2.2 Numerical Simulation

Air damping on the diaphragm of the synthetic jet is the most important factor to determine the performance of the synthetic jet. Higher damping leads to smaller amplitude of oscillation. Decreased amplitude leads to reduced peak jet velocity. In the numerical simulation, air flow inside the cavity of the synthetic jet is simulated with a vibrating diaphragm. Power consumption is calculated to determine air damping. The commercial Computational Fluid Dynamics (CFD) software, ANSYS FLUENT [99] is used for the numerical simulation.

2.2.1 Numerical model

In the numerical model, the fluid domain is extracted and simulated independently (Figure 2.4). When the diaphragm is moving toward the orifice, the air inside the cavity is pushed through the wedge platform hole and orifice to the channel environment for impingement cooling. The oscillating diaphragm of the synthetic jet is defined as a rigid moving wall using a layering dynamic mesh which can be realized with a user defined

function. The diaphragm is defined in the numerical simulation in such a way that it matches the real situation. Due to the symmetry of the problem, one unit could be computed to represent the whole module (Figure 2.5). Thus, the side walls of the cavity are defined as symmetric boundaries (Figure 2.5).

A three-dimensional, incompressible, time-dependent scheme was used to compute the flow. For each cycle, fifty time steps were calculated to capture the unsteadiness of the specific flow and for each time step the internal iterations were allowed to continue until the residuals reduced to 10^{-6}. The surface-averaged static pressure on the diaphragm and the diaphragm velocity were recorded during each time step to obtain the instantaneous fluidic power using the equation:

$$P = p \times V \times A \tag{1}$$

where p is the surface-average static pressure on the diaphragm, V is the diaphragm velocity and A is the area of the diaphragm. The time-average power consumption for one cycle was computed for judging the design.

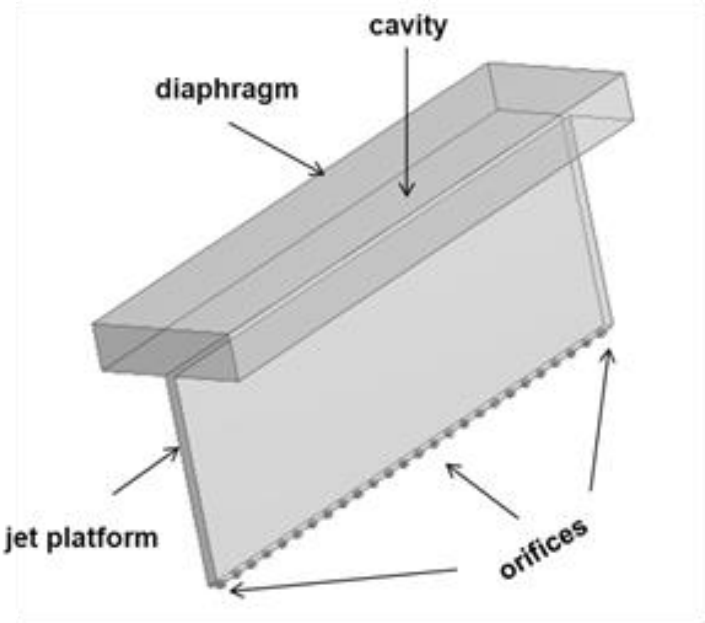

Figure 2.4 Fluid domain in the numerical simulation

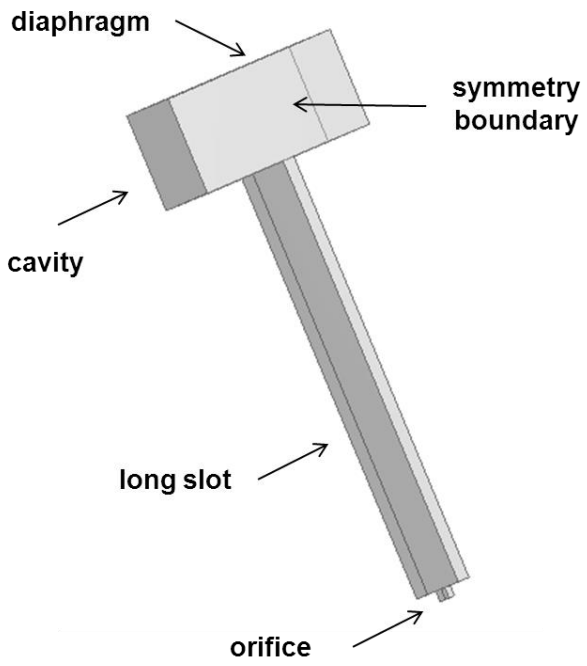

Figure 2.5 One unit in the numerical simulation

2.2.2 Numerical Study

In the numerical simulation, the dimensions of the cavity and the diaphragm were kept constant since the synthetic jets were driven by the same actuator. The dimensions of the orifices were also kept constant. The different shapes of the flow path based on different wedge shaped platforms were studied in search of an optimum configuration. Table 2.1 shows the basic dimensions, which did not change in the numerical simulation. A wedge-shaped platform with a long slot flow path was considered first, due to the simplicity of the structure. The effect of the length of the flow path was studied first. The long slot case (40 mm) was compared with the short case (10 mm) (Figure 2.6). It is found that the longer flow path increased the power consumption due to the extra friction with the walls. Thus, in the actual design, the length of the flow path should be as small as possible. The length of the flow path was chosen as 10 mm, considering the manufacturability. A tetrahedral mesh was used for the simulation. The number of elements was about 0.3 million.

Table 2.1 Dimensions of the orifices and the cavity

orifice dimension	1×1 mm^2
orifice thickness	1 mm
number of orifices	25
cavity size	30×100 mm^2
cavity thickness	10 mm

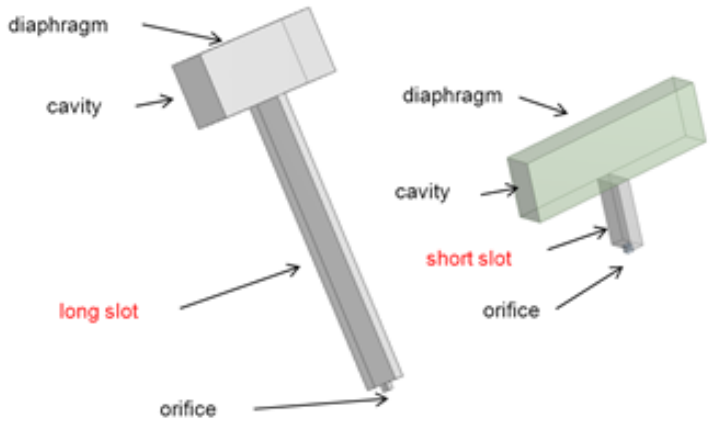

Figure 2.6 Comparison between the long slot and short slot

Table 2.2 The performances of wedge platform with long slot and short slot

	Long slot	Short slot
Cross area	2×100 mm^2	2×100 mm^2
slot length	40 mm	10 mm
power	1.59 W	1.45 W

Although the wedge shaped platform with a slot flow path has the simplest structure, it is difficult to fabricate. The cylinder design was considered, since it is easier to fabricate by drilling multiple holes on the wedge-shaped platform. The cylinder design was compared with the slot design (Figure 2.7) to verify that the cylinder design would not increase fluid damping excessively. It was found that the fluid power consumption levels for these two designs are almost the same, under the same conditions (Table 2.3). As a result, the cylinder design was chosen due to the ease of fabrication.

The effect of diameter of the cylinder on air damping was studied. Figure 2.8 shows power consumption of three cases. It can be seen that the diameter of the cylinder is not an important factor on air damping within the range studied.

After the numerical simulation, the final dimensions were decided (Table 2.4). On the inclined face of the wedge were 2.5 mm diameter orifices. A plate with 0.9 mm square orifices was inserted in the groove engraved at the bottom of the plate. The path length for the fluid to travel was 10 mm. This configuration resulted in a jet angle of 62 degrees with respect to horizontal.

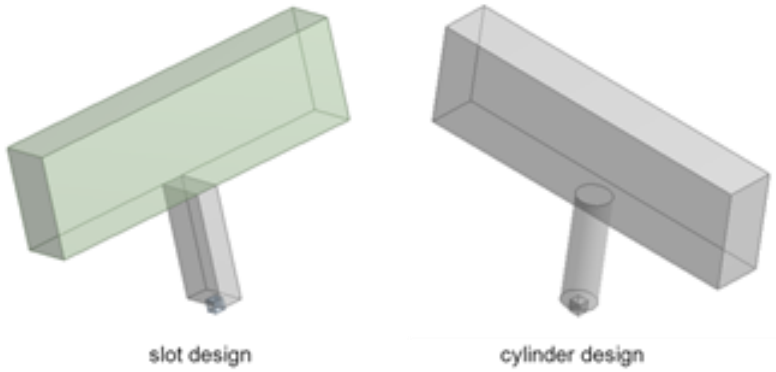

Figure 2.7 Comparison between the slot design and the cylinder design

Table 2.3 The performances of wedge platform with a slot and a cylinder

	Slot design	Cylinder design
cross section area	2×100 mm^2	3 mm hole diameter
slot length	10 mm	10 mm
power	1.45 W	1.47 W

hole diameter	Power
2 mm	1.46 W
2.5 mm	1.5 W
3.5 mm	1.5 W

Figure 2.8 The power consumptions with different diameters of the cylinders

Table 2.4 Dimensional attributes of wedge platform

Parameter	Dimension
Diameter of circular holes on the inclined face	2.5 mm
Size of square orifice	0.9 mm ×0.9 mm
Thickness of orifice plate	2 mm
Length of fluid path	10 mm

2.2.3 Experimental Results

Velocity tests were done to ensure that the peak jet velocities from the wedge match those of a flat cavity without the wedge platform. Tests were conducted using hot film anemometry with a TSI 1240 miniature hot film probe. The width of this probe was 0.9 mm, thus ensuring that the jet flow out of the 0.9mm × 0.9mm square orifice completely covers the active length of the probe, resulting in accurate velocity measurements. Table 2.5 shows the peak jet velocities from the wedge as well as from the flat cavity. Both cases had 25 0.9 mm x 0.9 mm square orifices.

Table 2.5 Peak velocities of two cases with and without the wedge shaped platform

Orifice No.	2	7	10
Velocity from Wedge	38 m/s	39 m/s	35 m/s
Velocity from Flat Cavity	44 m/s	43 m/s	41 m/s

It can be seen that the velocity from the wedge is not very different from that of the flat cavity, which indicates that the extra flow path length of the wedge platform didn't increase the loss much. This may be because smaller orifices are the major sources of flow resistance for a synthetic jet. The longer flow path introduced by the slot in the wedge platform provides minimal flow resistance, which is good for the application of a

wedge platform. The wedge-jet configuration was then mounted on the heat sink for use in the system heat transfer tests. The heat sink base temperatures were measured using thermocouples located at various positions within the heat sink. These temperatures were averaged to obtain a heat sink base temperature. Also the air temperatures at the inlet to the heat sink and at the outlet of the induced draft fan (which simulates a cross flow fan) were measured using thermocouples. Since the module was well insulated from the sides and the bottom, heat loss was considered to be minimal. The heat transfer results are shown in table 2.6. The thermal resistance of the heat sink was calculated as:

$$R_{th} = \frac{T_b - T_{in}}{q} \tag{2}$$

Where, q is the heat dissipated, calculated as,

$$q = m_{air} C_p (T_{Out} - T_{in}) \tag{3}$$

Table 2.6: Heat transfer test results for a synthetic jet with 25 orifices mounted on the wedge platform

Condition	Cross flow rate (CFM)	T_b (°C)	T_{in} (°C)	T_{out} (°C)	Heater power (W)	R_{th} (K/W)
Cross Flow Only	62.5	100	23.2	49.3	900.2	0.086
Cross Flow and Jets	62.5	99.5	23.9	49.5	883.5	0.085

It can be seen that the improvement in thermal resistance is minimal. It was inferred that an increase in the number of jets shooting into one channel could improve the situation. However, an increase in the number of orifices might reduce the peak velocities of the jets, which would be detrimental for heat transfer. Thus, there was a need to increase the number of orifices and at the same time keep the penalty on the peak velocity

low. It is believed that the oscillatory motion of the diaphragm over the cavity sets up re-circulating flows that may dampen the diaphragm motion. It has been reported that flow within the cavity reduces the amplitude of the resonating drive for the piston by as much as 40 per cent. This has a negative effect on the peak velocities. This re-circulation pattern can be weakened by offering more orifice area. The theory is that if the flow resistance to be reduced, the diaphragm amplitude would rise and the velocity would not fall as much as would be predicted by a simple mass conservation calculation based upon constant diaphragm amplitude. Velocity tests were done with a flat cavity jet with varying numbers of orifices to support this conclusion. Table 2.7 shows the results of these tests. It can be seen that the drop in velocities with increasing number of orifices is not so large.

Thus, a wedge platform was designed with four rows of orifices. Also, the orifices were staggered so as to cool the adjacent faces of the fins simultaneously. It has also been reported in that a staggered configuration of jets is more effective in cooling than an in-line configuration. Table 2.8 shows the heat transfer test results with such a configuration. It can be seen from table 8 that the thermal resistance of the heat sink module was about 0.084 K/W with the cross flow and the synthetic jet operating together. This amounts to a total heat load removal of about 50 watts by the synthetic jets alone.

Table 2.7: Peak jet velocities with orifice plate of 100 (4 rows – upper lines) and 125 (5 rows-lower line) of orifices

Column	**Row 1**	**Row 2**	**Row 3**	**Row 4**	**Row 5**
13	38 m/sec 39 m/sec	36 m/sec 37 m/sec	37 m/sec 36 m/sec	36 m/sec 34 m/sec	 31 m/sec
10	43 m/sec 32 m/sec	39 m/sec 34 m/sec	37 m/sec 36 m/sec	38 m/sec 38m/sec	 35 m/sec

Table 2.8: Heat transfer test results for synthetic jets mounted on the wedge platform (with 100 orifices)

Condition	Cross flow rate (CFM)	T_b (°C)	T_{in} (°C)	T_{out} (°C)	Heater power (W)	R_{th} (K/W)
Cross Flow Only	63.4	98.2	25.3	49.0	829.7	0.088
Cross Flow and Jets	63.4	93.8	24.8	48.3	821.1	0.084

2.3 Conclusions

In this study, synthetic jets were used in an inclined configuration for active cooling enhancement in a heat sink having fan-induced throughflow. An inclined configuration may be necessary in situations where the jet actuation parts interfere with other module components. Numerical simulations were done to design a platform to incline the jets with minimal loss of fluid power. The number of jets per channel of the heat sink was optimized for improved performance without penalizing on the peak jet velocity. For a four-staggered-jet-per-channel configuration, the thermal resistance was 0.084 K/W in the presence of both synthetic jets and flow through.

Chapter 3 Numerical Simulation of Synthetic Jets with Channel Flow in Single Unit Module

In the present work, a heat sink cooling module combined with synthetic jet arrays is simulated physically and numerically. Though the heat sink has multiple channels, the present study focuses on a single channel. The synthetic jet arrays used in this channel are driven by two piezoelectric stacks. Heat transfer performance characteristics with the synthetic jets and the single channel flow are measured under various conditions. Also, numerical simulation is conducted to further investigate flow and heat transfer within the heat sink since it can provide information which is difficult to realize in the experiments.

3.1 Experimental Study

3.1.1 Heat Transfer Test Facility

The heat sink has 20 fins mounted on a 100 mm x 100 mm base. The fin height is 16.5 mm with a thickness of 1.6 mm (Table 3.1). The distance between each two fins is 5 mm. The air flow comes from the two ends of the heat sink, turns 90°, and exits from a 20 mm x 90 mm opening in the middle. Because of the symmetry of each fin, a single-channel heat sink test facility could be used to verify the whole 20-channel heat sink design (Figure 3.1). The exit of the channel is connected to a vacuum pump (Figure 3.2) so that a flow is generated through the channel. Synthetic jets are put on top of the channel to allow impingement on the fins, which are the side walls of the channel, to

enhance heat transfer performance. Two synthetic jet arrays of 2×10 jets (Figure 3.3) are driven by two separate piezoelectric stacks (model P-007.40 of the PI Co.). Each orifice is a 0.9 mm x 0.9 mm square. The synthetic jets are operating at 1250 Hz having a peak velocity of about 44m/s. The temperatures of the fin walls and air inlet temperature are measured using E-type thermocouples (Omega, 5TC-TT-E-40-36). The heat transfer test facility is heated by using a Kapton heater in the base which is powered by a DC power supply. The input power is determined as the product of voltage and current to the heater. The heat transfer performance of the heat sink is evaluated by its convective heat transfer coefficient defined as:

$$h = q/(A \times \Delta T) \tag{1}$$

where q is the power input to the heater and A is the cooled surface area. The temperature difference, ΔT, is the channel log mean temperature difference [17] defined as:

$$\Delta T = \frac{(T_{fin\_in} - T_{air\_in}) - (T_{fin\_out} - T_{air\_out})}{\ln[(T_{fin\_in} - T_{air\_in}) - (T_{fin\_out} - T_{air\_out})]} \tag{2}$$

The temperatures of the inlet air and the fins are measured by thermocouples and the temperature of the outlet air is calculated using an energy balance, then verified by thermocouples.

3.1.2 Uncertainty Analysis

The uncertainty values of the heat transfer coefficients in this test come from uncertainties in the measurements of temperature, flow rate, and heater power. The uncertainty of the temperature measurement from the thermocouples is 0.5°C over a 22~63°C range. The uncertainty of the thermocouple location measurement is very small (within 1.0 mm over a 11.0 mm range). The uncertainty for DC voltage is 0.1 V over a 20

V range and for DC current is 0.01 Amps over a 1.00 Amp range. The uncertainty for the flow rate measurement is less than 1.0 %. The estimated bias error and the calculated precision error of the heat transfer coefficients are 5.4% and 3.7%, respectively. By assuming that each component of uncertainty is independent and using the propagation method of Kline and McClintock [100], assuming that the estimated bias error is equally likely to be low as high, we compute the overall uncertainty for the heat transfer coefficient to be 7% with a 95% confidence interval. The repeatability of the experimental results has been checked by repeating the same experiment three times. The overall difference is found to be within 5%, which showed that the test setup can be considered to be repeatable.

3.1.3 Results and Discussion

The thermal performance of the heat sink was measured with and without synthetic jets operating to obtain the heat transfer enhancement effected by the synthetic jets. Table 3.2 shows the enhancement by the synthetic jets under cases of different z distances (between the orifice plate and the fin tip). The channel flow inlet velocity is constant at 8 m/s. It is observed that the heat transfer coefficient increased by 22% when the synjets were activated and the orifice-plate-to-fin-tip distance was 2 mm. The enhancement is found to decrease with an increasing distance between the orifice and fin tip, which is due to a weakening synthetic jet flow in the fin tip region.

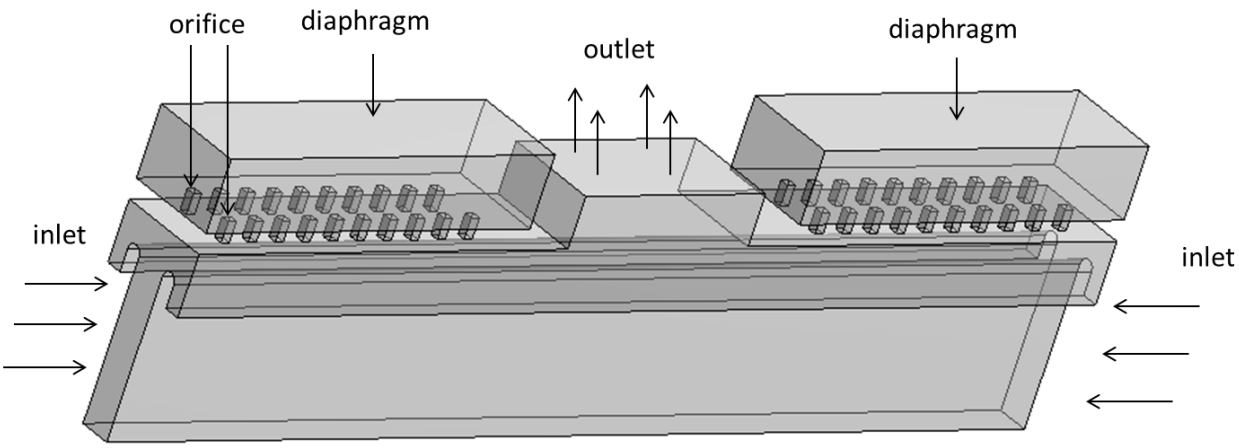

Figure 3.1 Schematic of the heat transfer test facility

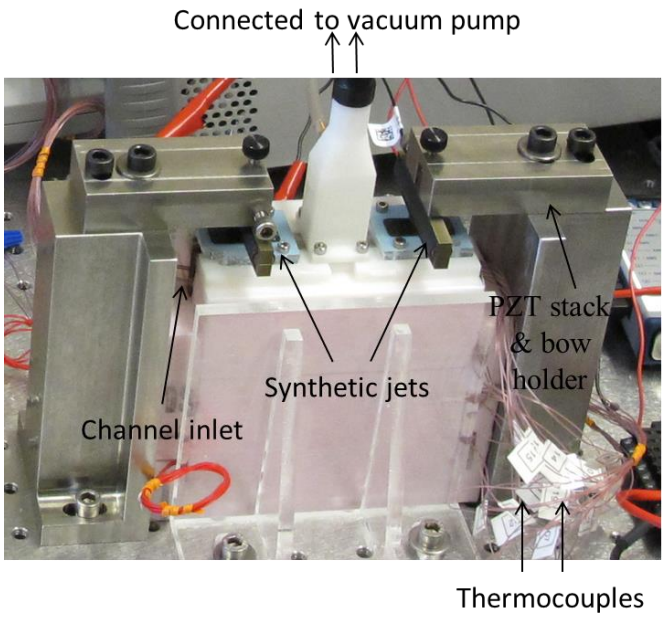

Figure 3.2 A picture of the heat transfer test facility

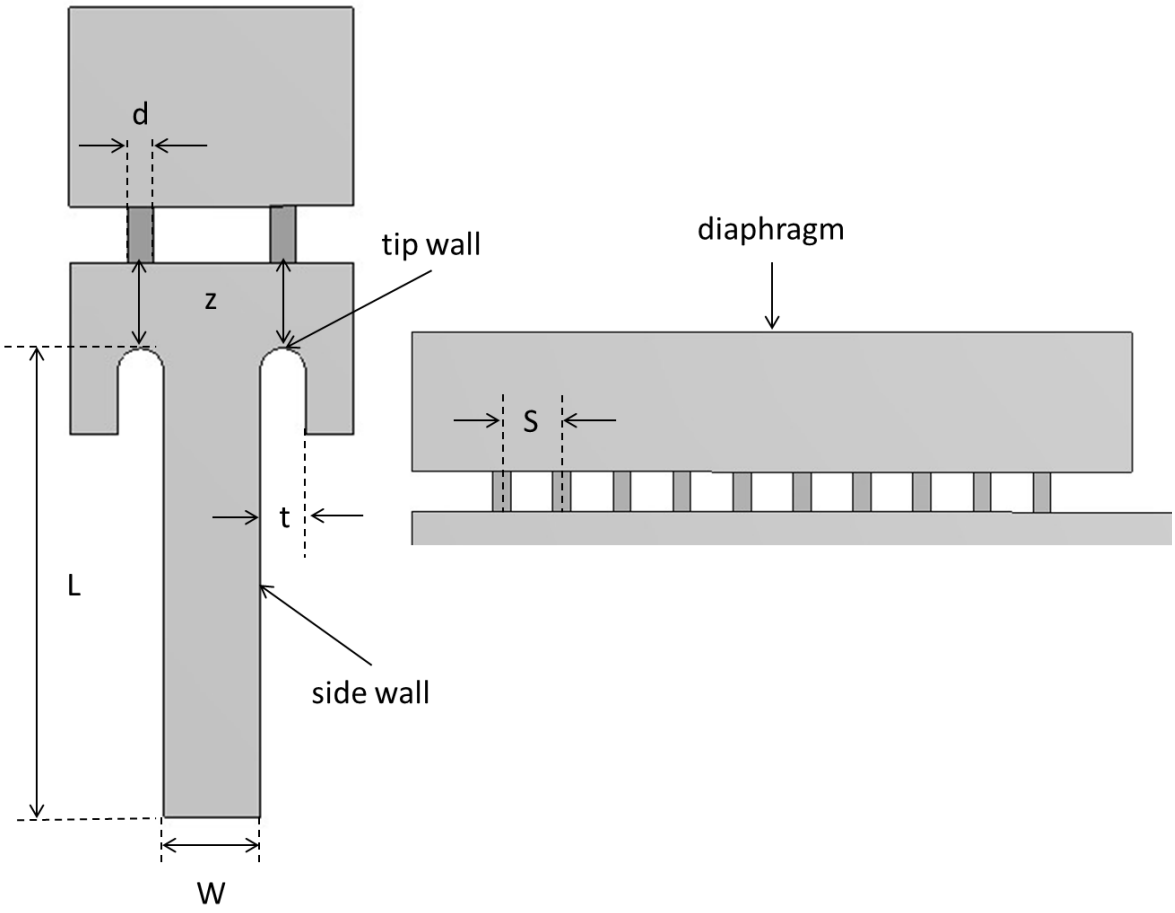

Figure 3.3 Front view and part of the side view of the test section

Table 3.1 Values of various parameters

Symbol	Name	Value
d	Square orifice side length	0.9 mm
f	Synthetic jet diaphragm frequency	1250 Hz
z	Jet to stagnation point distance	3 mm
S	Two jets spacing	3 mm
t	Fin thickness	1.6 mm
L	Fin length	16.5 mm
U	Cross-flow velocity	8 m/s

V	Jet peak velocity	44 m/s
W	Channel width	3.4 mm

Table 3.2 The measured heat transfer coefficients

z	2 mm	3 mm	4 mm
Channel flow	115 w/m^2k	105 w/m^2k	110 w/m^2k
Channel flow + jets	140 w/m^2k	123 w/m^2k	121 w/m^2k
increase	22.10%	16.90%	10.20%

3.2 Numerical Simulation

3.2.1 Numerical Model

In this section, the numerical simulation of heat transfer enhancement by synthetic jets in the heat sink is introduced to further investigate the behavior of the synthetic jet flow within the channel. The geometry of the numerical model is exactly matched with the experimental setup and the numerical model is validated by comparing with the experimental results. The moving diaphragm, which is driven by the piezoelectric stack in the experiment, is modeled as a moving wall by using a layering dynamic mesh in the commercial computational fluid dynamics (CFD) software (ANSYS FLUENT) [18]. Each time the diaphragm changes its position; the software updates the meshes and calculates the flow. The inlet of the channel flow is defined as a constant velocity boundary with a constant air temperature (27 °C). The values of the inlet velocity are given by matching the flow rate with that of the experiment. All the convective walls of the fin are defined as constant temperature boundaries held 10 °C higher than the inlet air temperature. In the computation, three-dimensional, incompressible, time-dependent

Reynolds-Averaged Navier-Stokes equations (RANS) are solved with the shear-stress-transport (SST), k-ω turbulence closure model. First-order, implicit, Euler discretization is used for the time model. The second-order upwind scheme is employed for other terms in the momentum and energy equations. The Semi-Implicit Method for Pressure Linked Equations (SIMPLE) algorithm is employed for pressure-velocity coupling. For each oscillation cycle, the program runs 50 time steps (1.6×10^{-5} s for each time step) and the internal iterations continue until the residuals have been reduced to 10^{-6}. One specific case was run under different mesh sizes to validate grid independence and minimize computational error. The average heat transfer coefficients of the round tip, side walls, and all convective surfaces (sum of the two) are compared with various numbers of mesh cells (Table 3.3). The results show good convergence with a maximum difference of less than 5%. The numerical model is further validated by comparing its results with the experiments for one specific case. The dimensionless number, Nusselt number ($Nu = h_{avg}D_h/k$), is used to make the comparison. The geometry and jet velocity are matched between experiments and computations. Good agreement is shown in Figure 3.4 with a maximum difference of less than 10%.

3.2.2 Parametric Study of Synthetic Jet Heat Transfer Enhancement when Operating in a Channel Flow

A parametric study of synthetic jet behavior when operating in a channel flow is developed using the numerical model. The synthetic jet is operating at 1250 Hz and the jet orifice plate is 3mm away from the fin tip. The Reynolds number of a synthetic jet (Re_jet) is calculated using jet peak velocity, V, and its hydraulic diameter (0.9 mm). The

Reynolds number of the channel flow is calculated using channel flow velocity, U, and the channel hydraulic diameter.

The effects of jet peak velocity when operating at the same channel flow velocity. The amplitude of diaphragm movement is changed while the frequency is held constant at 1250 Hz to obtain different peak jet velocities (V = 0 - 60 m/s, Re_jet = 0 - 3715). The jet velocity, V, is zero when the jet is not operating and only channel flow exists. The heat transfer coefficient in the tip region is found to increase significantly with increases of jet velocity (Figure 3.5). An increase of 413% over the channel flow only case was observed with a peak jet velocity of 60 m/s (Re_jet = 3715) and a channel flow velocity of 4 m/s (Re_channel = 1451). Heat transfer coefficients on the side walls were found to increase also with increases of the jet velocity. However, the rate is much smaller than seen in the tip region. The jet had a lower influence on heat transfer when the velocity of the channel flow was increased. The influence of the synthetic jets was found to mainly be near the tip region and the enhancement is better under lower channel flow velocity conditions.

The effect of channel flow velocity at the same peak jet velocity. In this study, the channel flow velocity is varied (U = 4-16 m/s, Re_channel = 1451-5805) while the synthetic jet conditions are fixed. The heat transfer coefficients in the tip region are found to be not sensitive to changes of channel velocity except in cases with low jet Reynolds numbers (i.e. 536, Figure 3.6). The reason is that the synthetic jet plays a dominant role when its velocity is large compared to channel flow velocity. However, the impinging flow of the jet will be carried away by the channel flow when the jet is relatively weak. The heat transfer coefficients on the side walls were found to increase significantly with

increases of channel flow velocity, compared with increases of synthetic jet velocity (Figure 3.5), which indicates that channel flow plays a more important role in this region than does jet flow. The flow of the synthetic jets is carried away by the channel flow in the side wall region under these conditions.

The effects of changing distance between the orifice plate and the fin tips. The inlet velocities are kept the same from case to case in this study. The frequency of the synthetic jet is held constant (1250 Hz) and the amplitude of oscillation is changed to generate changing peak jet velocities. The distance between the orifice plate and the fin tip is changed from case to case to determine the effects on heat transfer performance. It is observed that the heat transfer coefficients on the different surfaces show similar trends (Figure 3.7). The heat transfer coefficients are nearly the same though the z distance is changed, if the peak jet velocity is small. The heat transfer coefficient rises with smaller z-distances when the jet velocity is large. The synthetic jet flow is more influential on the overall heat transfer performance if the jet is put closer to the fin, for it is less inclined to be carried away by the channel flow.

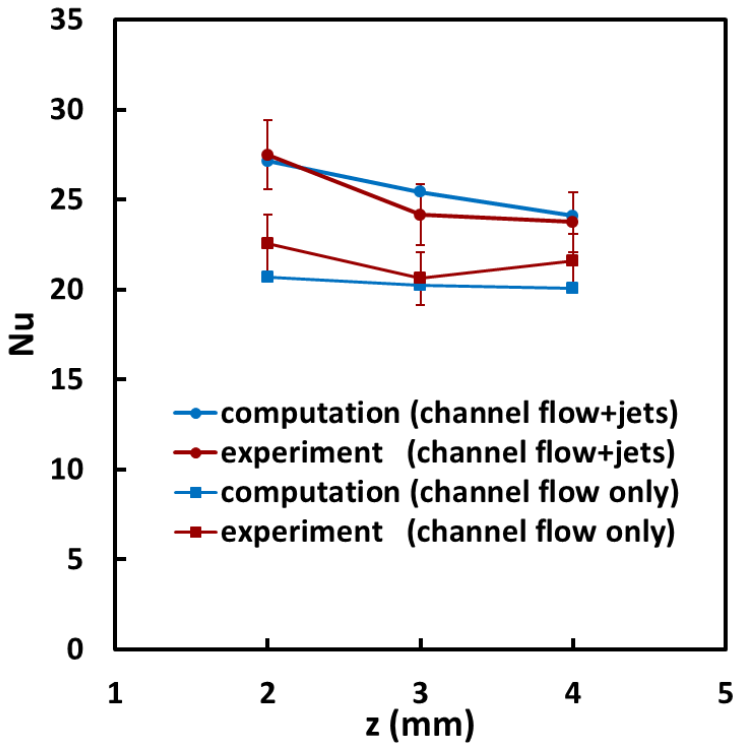

Figure 3.4 Comparison of average Nusselt numbers between experiment and numerical simulations

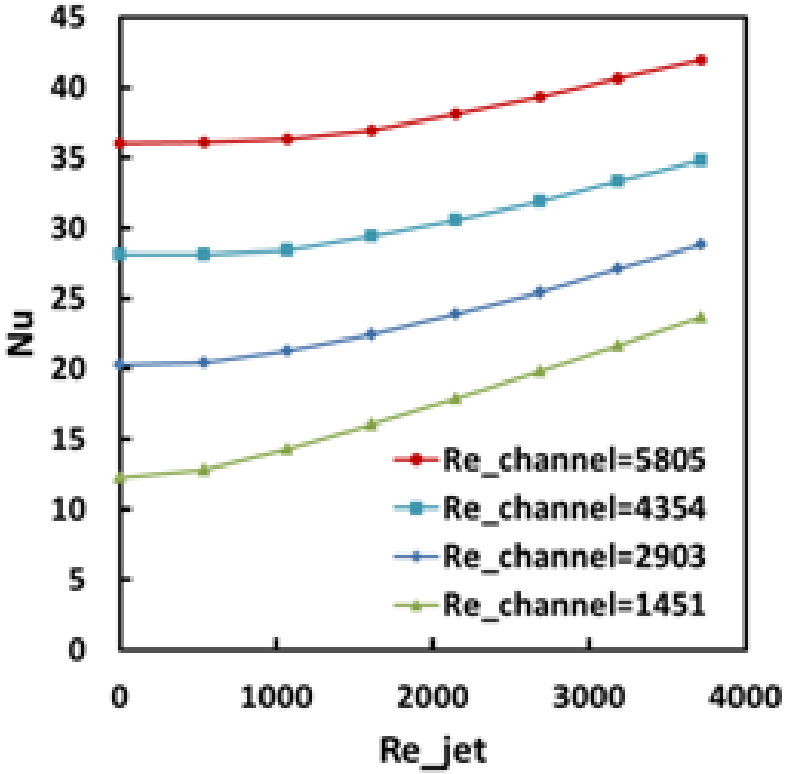
45
40
35
30
25
20
15
10
5
0
Nu
0
1000
2000
3000
4000
Re_jet
Re_channel=5805
Re_channel=4354
Re_channel=2903
Re_channel=1451

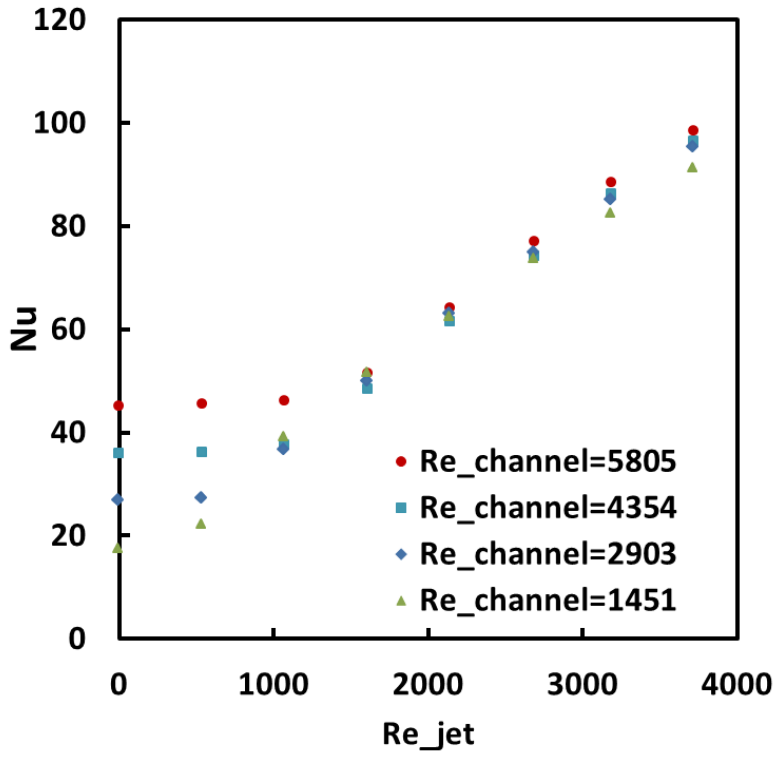
120
100
80
60
40
20
0
Nu
0
1000
2000
3000
4000
Re_jet
Re_channel=5805
Re_channel=4354
Re_channel=2903
Re_channel=1451

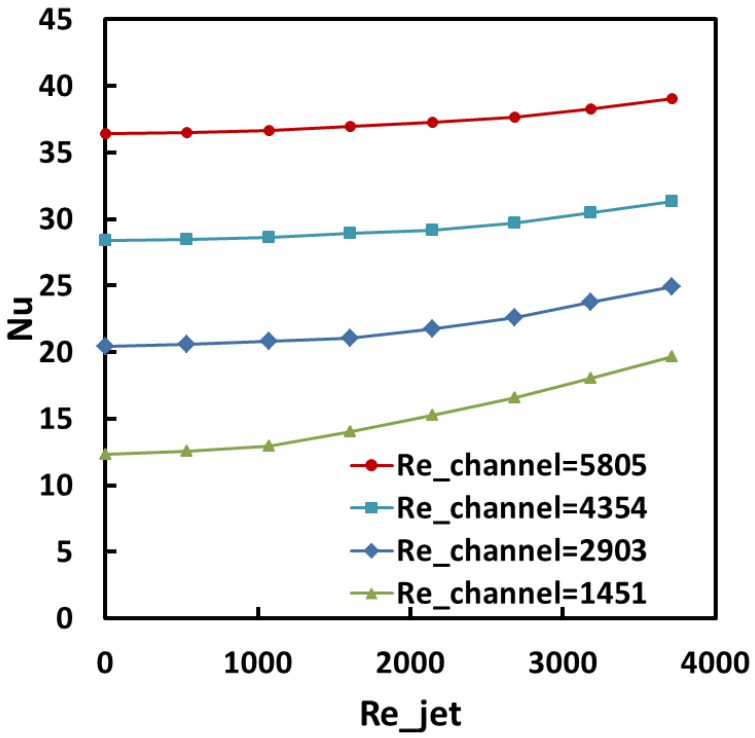

Figure 3.5 Average Nusselt numbers for cases with different jet velocities; top - round tip, middle - side wall, and bottom - all walls, round tip and side walls

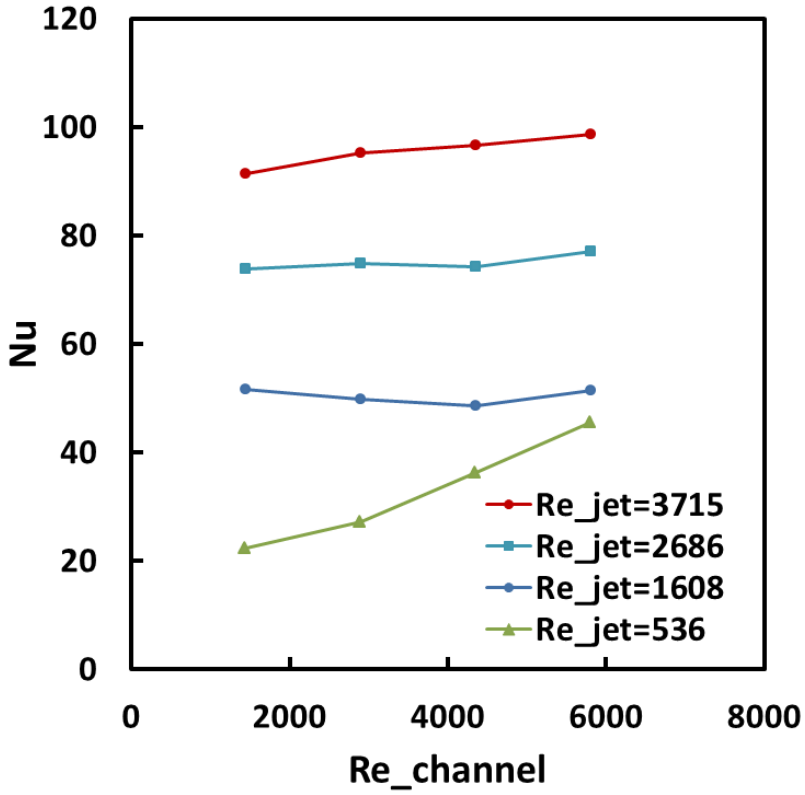
120
100
80
60
40
20
0
Nu
0
2000
4000
6000
8000
Re_channel
Re_jet=3715
Re_jet=2686
Re_jet=1608
Re_jet=536

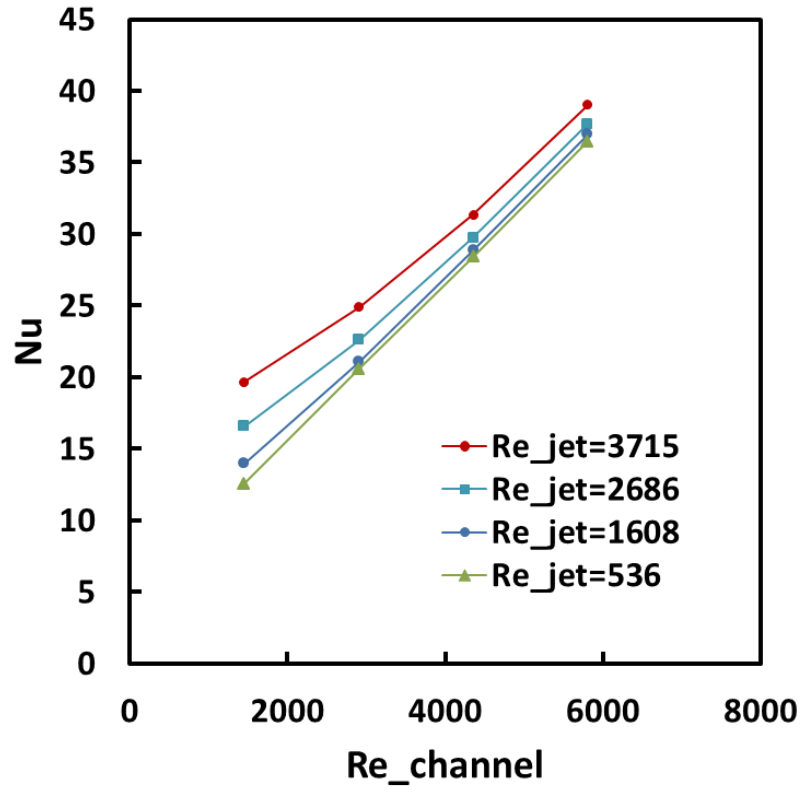
45
40
35
30
25
20
15
10
5
0
Nu
0
2000
4000
6000
8000
Re_channel
Re_jet=3715
Re_jet=2686
Re_jet=1608
Re_jet=536

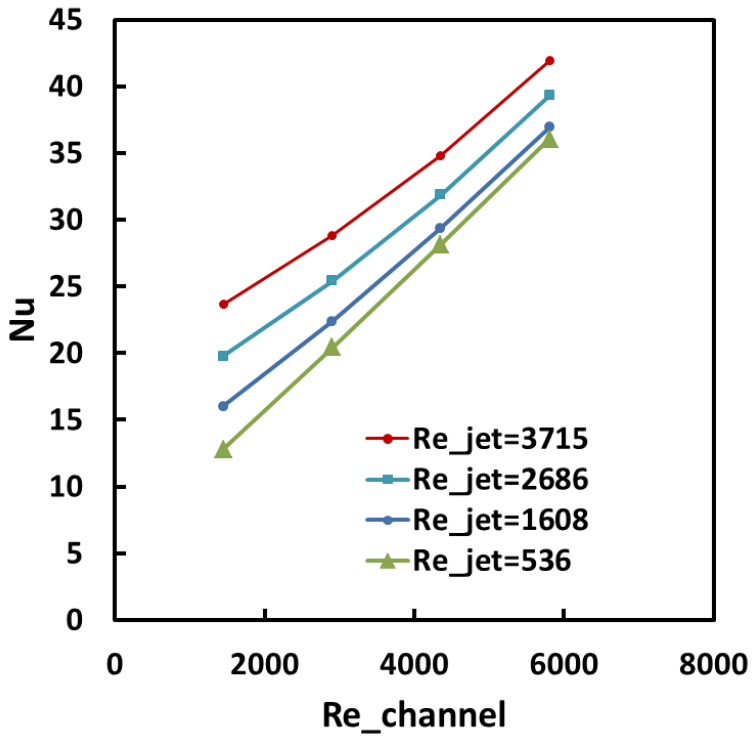

Figure 3.6 Average Nusselt numbers for cases with different channel velocites; top - round tip, middle - side wall, and bottom - all walls, round tip and side walls

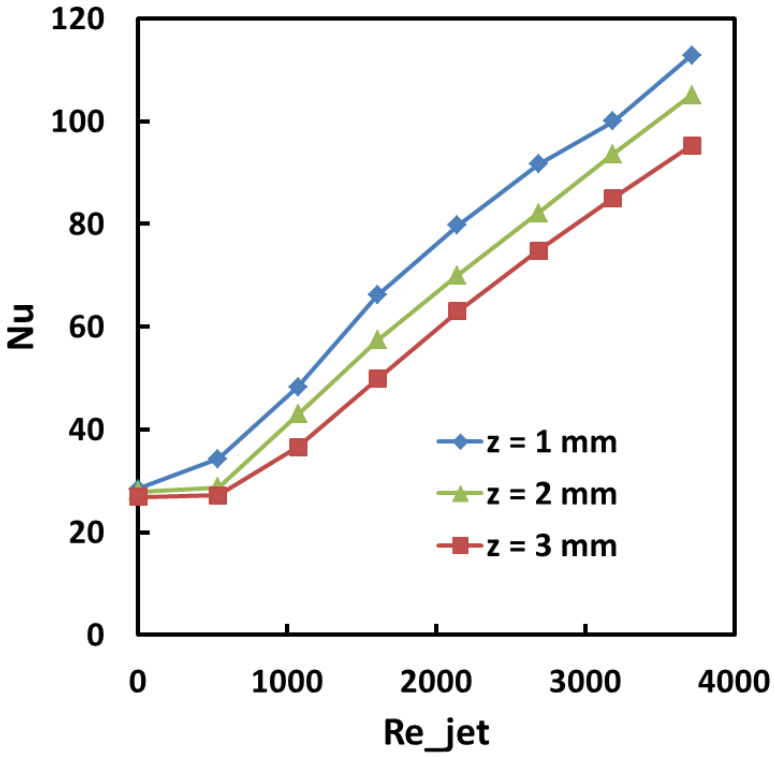
120
100
80
60
40
20
0
Nu
0
1000
2000
3000
4000
Re_jet
z = 1 mm
z = 2 mm
z = 3 mm

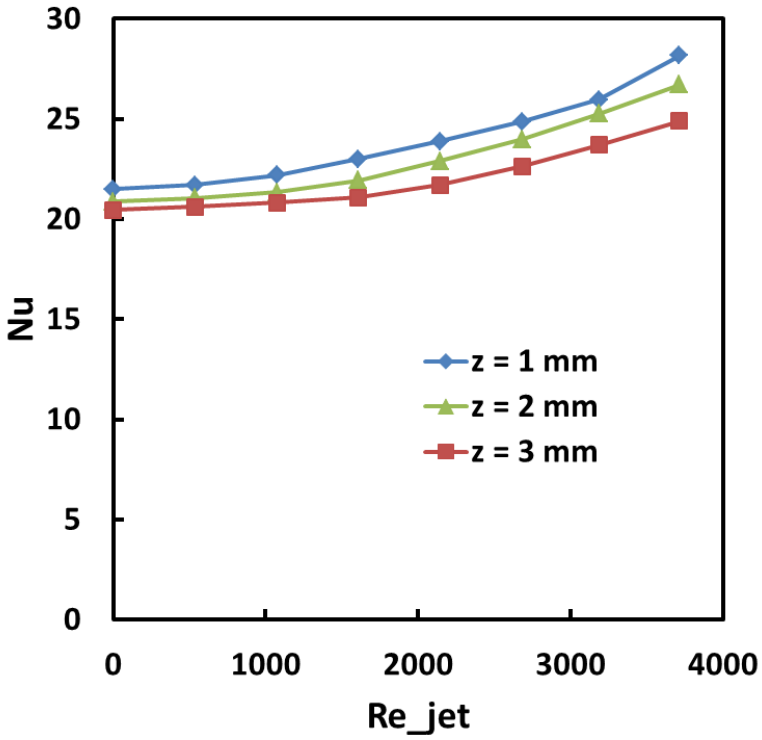
30
25
20
15
10
5
0
Nu
0
1000
2000
3000
4000
Re_jet
z = 1 mm
z = 2 mm
z = 3 mm

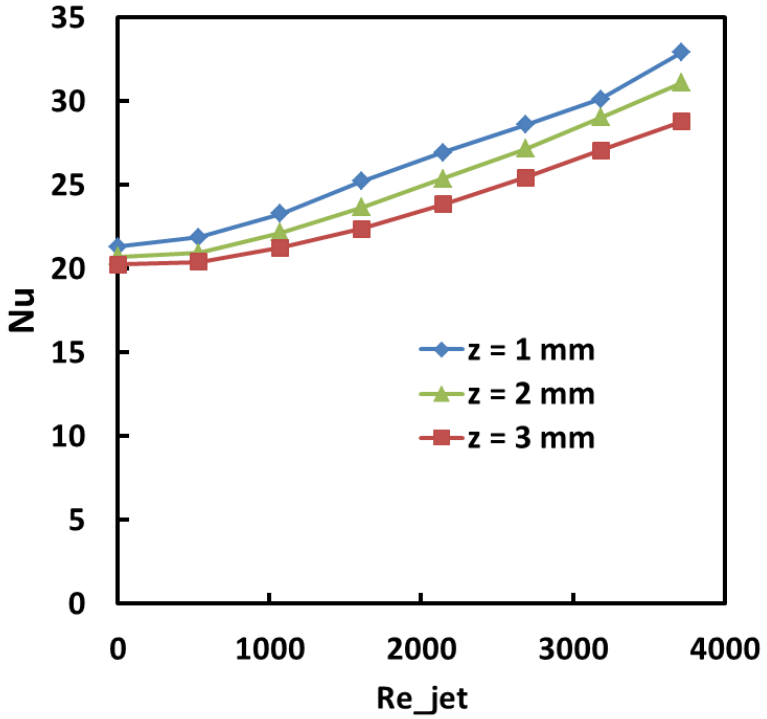

Figure 3.7 Average Nusselt numberss for cases with different z/d; top - round tip, middle - side wall, and bottom - all walls, round tip and side walls

Table 3.3 Heat transfer coefficients with different grid sizes: grid independence study

Number of cells	h_{avg} of round tip (W/m^2K)	h_{avg} of side walls (W/m^2K)	h_{avg} of all surfaces (W/m^2K)
0.5 million	120.2	90.4	91.5
0.9 million	120.3	90.3	91.2
1.5 million	121.5	91.7	92.7
2.5 million	121.9	92.7	93.5

3.3 Conclusions

Heat transfer enhancement using synthetic jet arrays in heat sinks for electronics cooling was investigated experimentally and computationally. A heat transfer test facility was fabricated to measure this heat transfer enhancement. The synthetic jets are driven by two piezoelectric stacks which are operating at a resonance frequency of 1250 Hz to

provide a peak velocity of 44 m/s. The measured overall heat transfer enhancement is found to be more than 20%, based on heat transfer coefficients for the channel flow only.

A numerical model was first validated by comparing its results to the experimental data. It was then used for a parametric study of the interaction between synthetic jet flows and channel flows. It was found that the heat transfer coefficients of the fin tip region were increased significantly by synthetic jets and channel flow had little effect on this region. A maximum heat transfer enhancement of 400% has been found by turning on the synthetic jets in the channel flow. The channel flow was found to be more effective in cooling the fin side walls. Synthetic jets were found to have more influence near the fin tip region and were not able to penetrate much further, due to interaction with the channel flow. The heat transfer increase in this region by the synthetic jets is less than 10%. Finally, a study of the effects of distance between the jet orifice plate and the fin tip also showed that synthetic jets can be more effective in cooling the fin tip region.

Chapter 4 Mock-up Experimental Study of a Synthetic Jet Impinging Cooling

A mock-up synthetic jet test facility has been fabricated for both fluid mechanics and heat transfer study of synthetic jet impingement cooling. The mock-up facility has been built geometrically and dynamically similar to the actual synthetic jet. As a result, the experimental data obtained from the mock-up test facility can be transformed to the actual case and guide the actual design. The dimensional analysis is introduced to document the comparison between the mock-up module and actual module.

Using the mock-up test facility, the flow fields of the synthetic jet impingement are documented under various conditions; the unsteady velocity and the turbulence are measured using a Laser Doppler Anemometer (LDA); the cooling performances of a synthetic jet impinging on a fin are obtained under various conditions (e.g. orifice shapes and operating frequencies)

4.1 Dimensional Similarity

The actual synthetic jet is operating at a very high frequency (around 1000 Hz) and the scale is very small (around 1 mm) which is a difficult size and speed combination for detailed measurements. A mock-up synthetic jet, which is dynamically similar to the actual jet, is fabricated to study the flow characteristics and its cooling performance when it is applied to an electronics module (Figure 4.2.1). The mock-up synthetic jet is designed to be dynamically and geometrically similar to the actual-size module by matching Reynolds number, Stokes number, and Prandtl number using a scale factor of

44. Table 4.1.1 compares some parameters of the actual setting and the mock-up setting. By keeping Reynolds number the same ($Re_{avg} = \rho U_{avg} d/\mu$), the velocity is 1/44 of the actual velocity and by matching Stokes number ($S = (\omega d^2/\nu)^{1/2}$), the frequency is $1/44^2$ of the actual frequency, which makes it easy to drive.

Figure 4.2.1 Mock-up synthetic jet (44 times actual jet)

Table 4.1.1 Comparison between large scale and actual scale in one specific case

Symbol	Name	Large scale value	Small scale value
d	Synthetic jet orifice diameter	44 mm	1 mm
f	Synthetic jet diaphragm movement frequency	0.63 Hz	1220 Hz
U_{max}	Jet peak velocity	1.14 m/s	50 m/s
z	Jet to Stagnation point distance	3 mm	132 mm
R	Radius of the fin	1.1 mm	48 mm
L	Length of the fin	2.2 mm	96 mm
W	Width of the fin	2.0 mm	90 mm

4.2 Experimental Test Facility

A mock-up heat transfer test facility is fabricated to study the characteristics of synthetic jet impingement cooling for application to an electronics cooling module. The heat transfer performance values of different orifice shapes at different frequencies of diaphragm movement are measured (Figure 4.2.2). The whole test facility is made of three parts: the dynamic motion system to drive the diaphragm of the jet, the chamber, and the test section. Each part will be introduced in detail in the following pages. The picture of the whole test facility is shown in Figure 4.2.3.

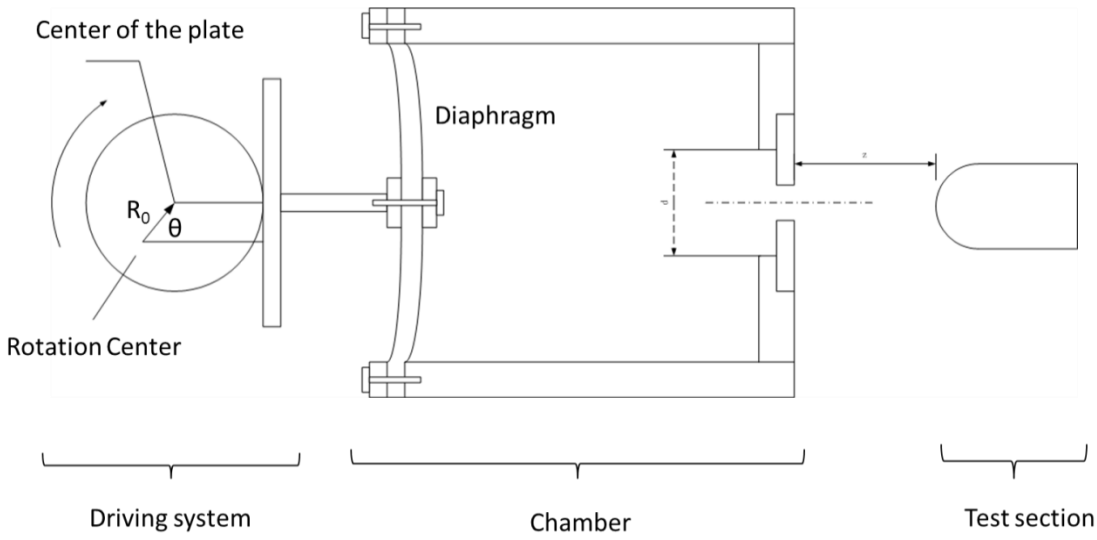

Figure 4.2.2 The schematic drawing of the whole test facility

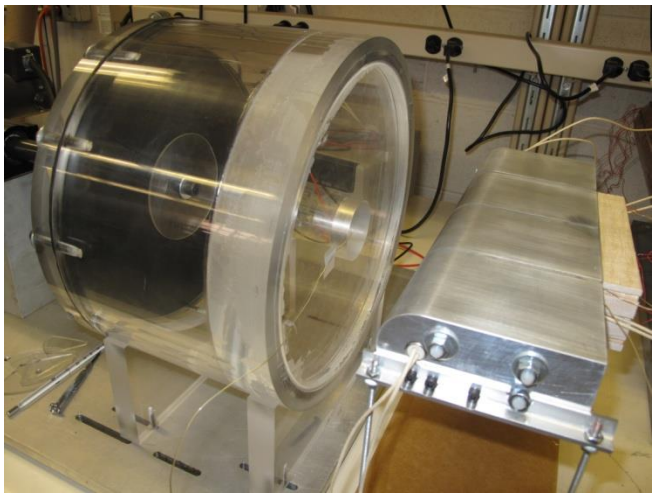

Figure 4.2.3 The picture of the whole test section

4.2.1 Driving System

A cam mechanism (Figure 4.2.4) is used to create sinusoidal movement to drive the diaphragm of the synthetic jet. An eccentrically mounted round plate of 152 mm (6 inches) diameter rotates to push another round plate, which is placed normal to the rotating cam. A spring is utilized to keep the moving plate always in touch with the

rotating plate. Since the vertical plate is always tangent to the round plate, the displacement of the plate, which is here defined to be the same as the axial distance from the center of the plate to the center of its rotation, is $X=A\times\cos\theta$, which is the same as the actual synthetic jet driving mechanism.

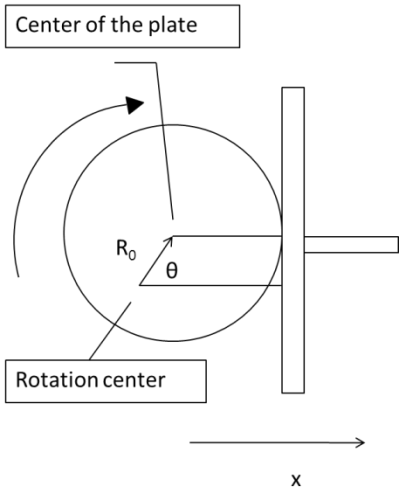

Figure 4.2.4 A cam design of the driving system

The chamber is well sealed, except for the orifice, so an unsteady flow is produced when the diaphragm moves back and forth to simulate a synthetic jet diaphragm. The rotation is driven by a DC Gearmotor (Dayton, Model 4Z381A). The motor is controlled by a DC speed controller (Dayton DC Speed Control, Model 5X412D). The controller supplies a speed range of 0-96 rpm.

4.2.2 Chamber Design

The chamber is made of a plastic tube with a thickness of 2 inches. A round piece of rubber is mounted in the back of the plastic tube which is driven by a piston with sinusoidal movement to simulate the movement of synthetic jet diaphragm (Figure 4.2.5). A 2-inch thick plastic plate is inserted and glued to the plastic tube in the front with a

shoulder to allow different plastic plates with different orifices arrangements to be easily mounted (Figure 4.2.6 and 4.2.7).

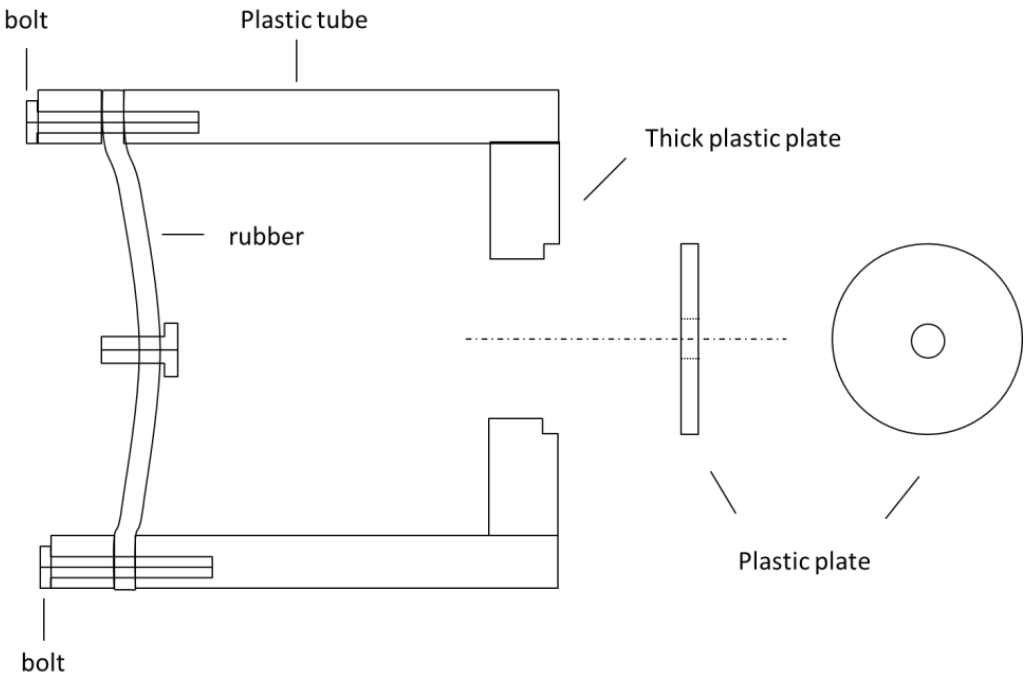

Figure 4.2.5 A schematic drawing of the chamber design

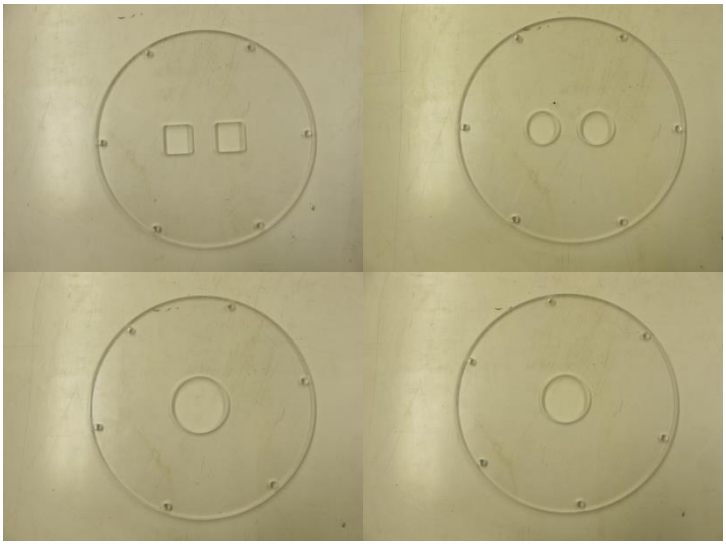

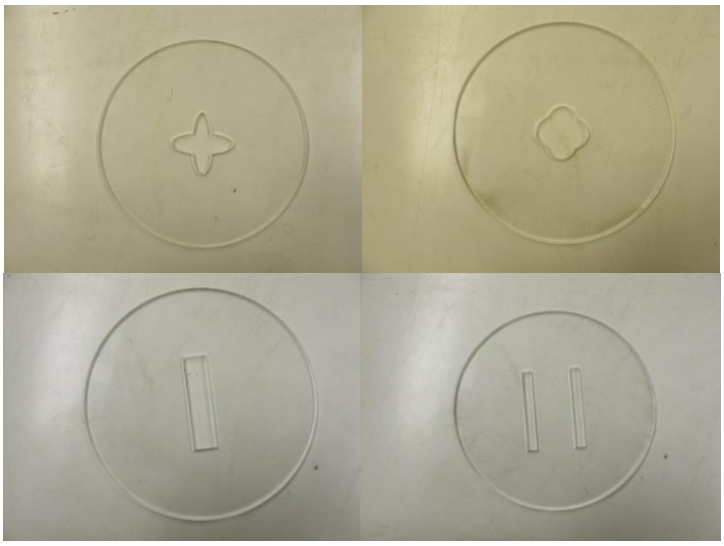

Figure 4.2.6 Different plastic plates with different orifices

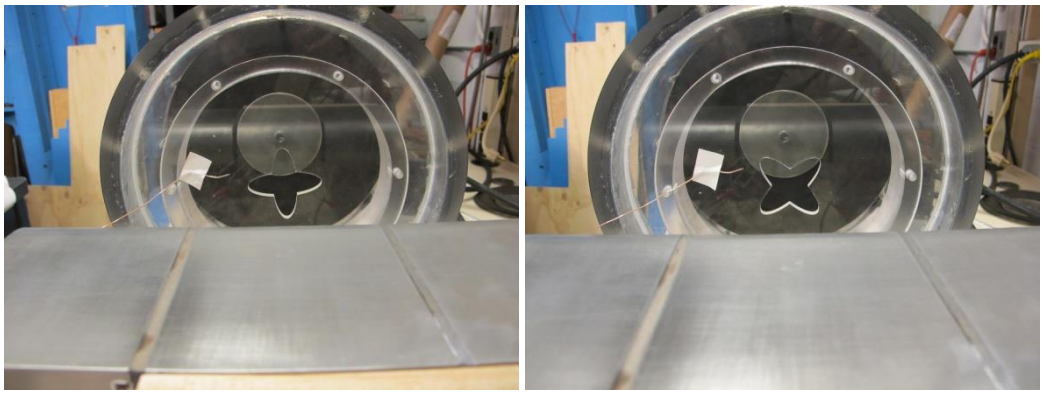

Figure 4.2.7 Two different rotation positions for the star shaped orifice

4.2.3 The Test Section

The test section is in front of the synthetic jet (Fig. 4.2.8). It consists of four identical aluminum units (Fig. 4.2.9) with wood between each two units. This test facility is used to study the cooling performance of one segment or two segments of the test wall. If it is applied to study heat transfer performance of two segments, the two segments at the sides of the test segment are the guard sections. If it is used to study cooling performance of one segment, one of the two middle segments is regarded as a guard unit.

In this experiment, the cooling performance of one segment is investigated. The temperatures of guard sections are adjusted to be the same as that of the test section to minimize heat transfer between the test section and ambient air. A thick piece of wood downstream of the two middle units is used to insulate the heaters from the ambient air downstream of the body (see Fig. 4.2.8). All four units are held by two threaded rods that are made of nylon to minimize the heat transfer between units. A rod heater is inserted into each unit. The power is measured using a multimeter that can be controlled by adjusting voltage input from the DC power supply. The heat flux range is between 0.007 W/cm^2 and 0.016 W/cm^2. The surface temperature is measured with K-type thermocouples mounted at two sides of each unit providing a spatially-averaged temperature over all convective surfaces. An identical thermocouple is mounted near the jet orifice to measure the ambient temperature taken to be the jet, or sink, temperature. The average heat transfer coefficient is defined as follows:

$$h_{avg} = \frac{q}{(T_s - T_{air})A} \tag{4.1}$$

$$q = VI \tag{4.2}$$

where q is the power input to the heater, a product of voltage and current.

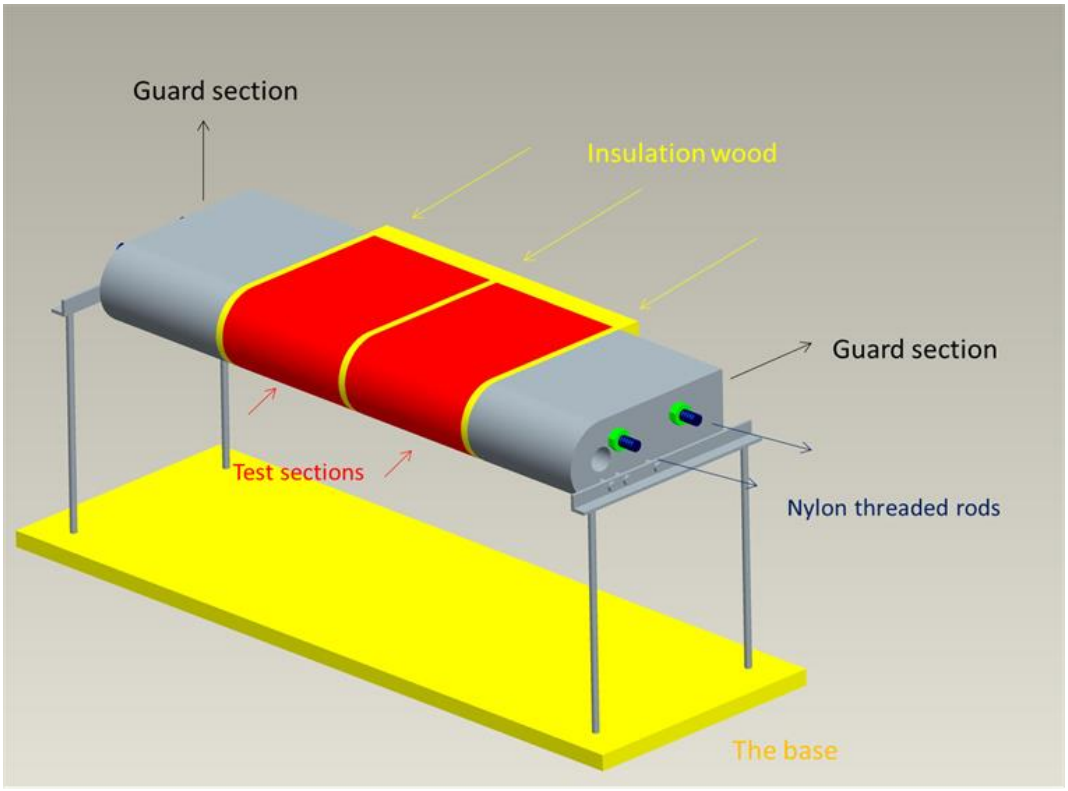

Figure 4.2.8 Schematic drawing for the whole test section

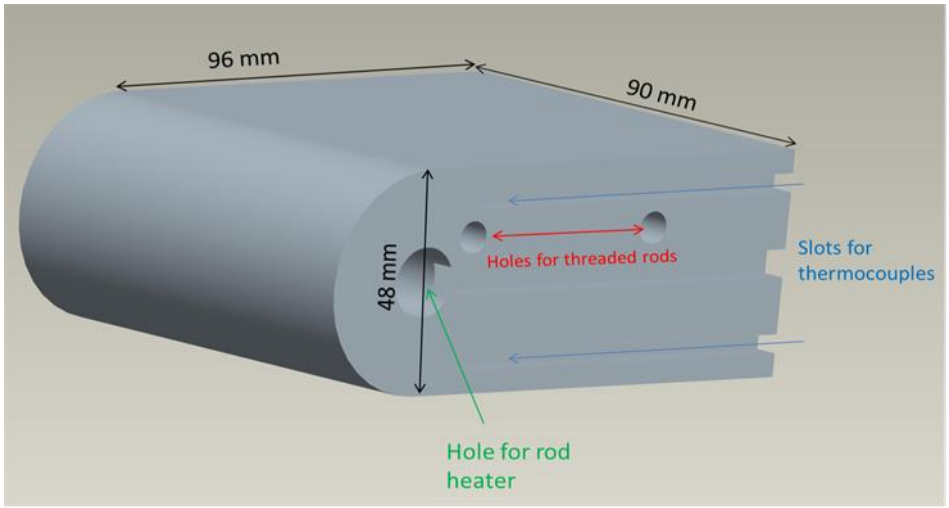

Figure 4.2.9 Schematic drawing for one unit of the test section

4.3 Heat Transfer Results and Analysis

The effects of different orifice shapes on heat transfer performance were studied for different frequencies (Figure 4.3.1). In the experiments, the distance between the test section and orifice plate was fixed (z = 132 mm). The amplitude of the diaphragm was held constant, thus providing a higher momentum flow with an increase of frequency.

The heat transfer coefficients and frequencies plotted on Figure 4.3.1 were scaled to the values of the actual module. Consequently, the heat transfer coefficients of the actual module are 44 times of the values obtained from the mock-up experiment and the frequency is 44^2 times mock up value. The average heat transfer coefficient showed an almost linear increase with frequency for all documented orifices (Figure 4.3.1). A high frequency (2700 Hz) synthetic impinging jet can provide a heat transfer coefficient of as high as 650 W/m^2K which indicates that the synthetic jet can be very effective for electronics cooling. A case with double circular orifices was found to outperform other cases.

The heat transfer coefficient of a single orifice with a smaller diameter was found to be higher than that with a larger diameter (Figure 4.3.2 (b)) as a result of higher velocity. The instantaneous, spatial-average velocity is larger with a smaller orifice when the amplitude and frequency are fixed. The heat transfer coefficients of the star-shaped orifices are found to be close to those of other qeometries (Figure 4.3.2 (c)). The comparison between one circular orifice and two circular orifices is shown in Figure 4.3.2 (d). The heat transfer coefficients were found to be close to each other. The possible

reason is that the one circular orifice produced high heat transfer on the tip region but lower performance on the flat walls. However, the two circular orifice shapes provide low cooling effect on the round tip but high performance on the flat walls. The overall total-surface-average performances were close to one another. The details will be discussed using numerical simulation and velocity experiment in section 4.4 and 4.5 in this chapter.

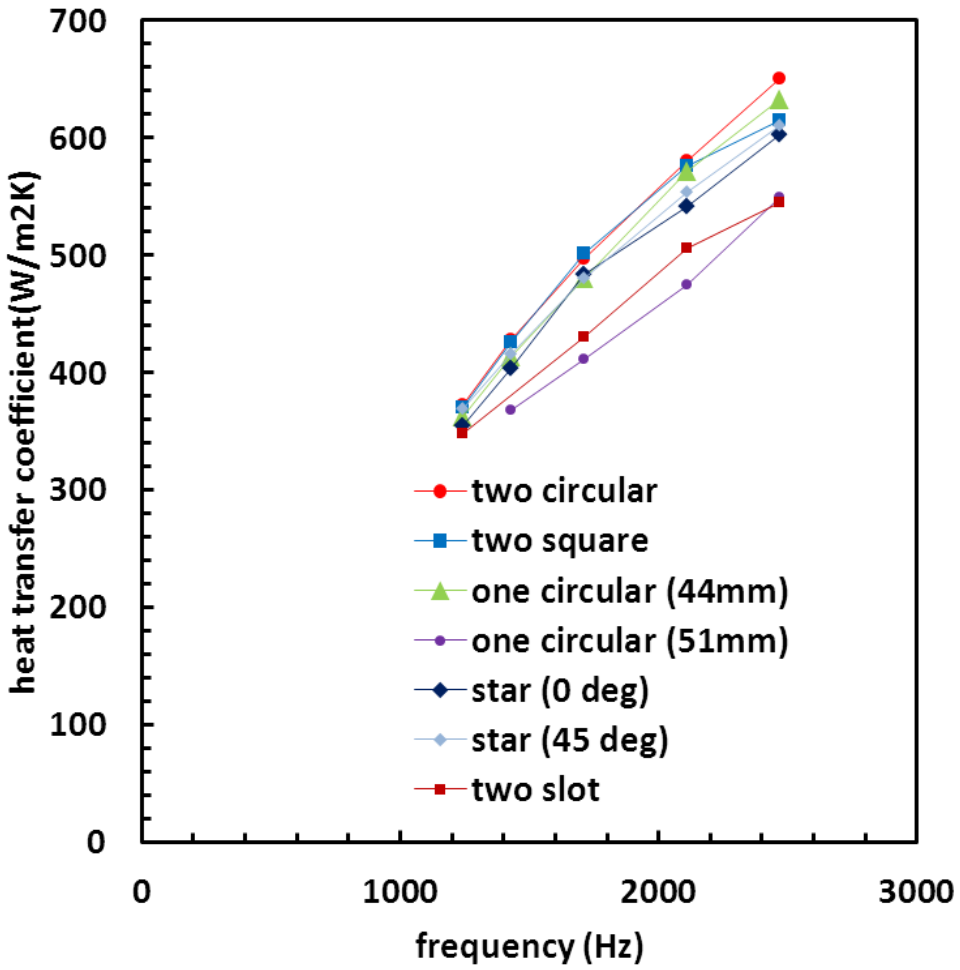

Figure 4.3.1 Surface average heat transfer coefficients as a function of frequency for different orifice shapes (all data are transformed to actual scale by matching the dimensionless numbers)

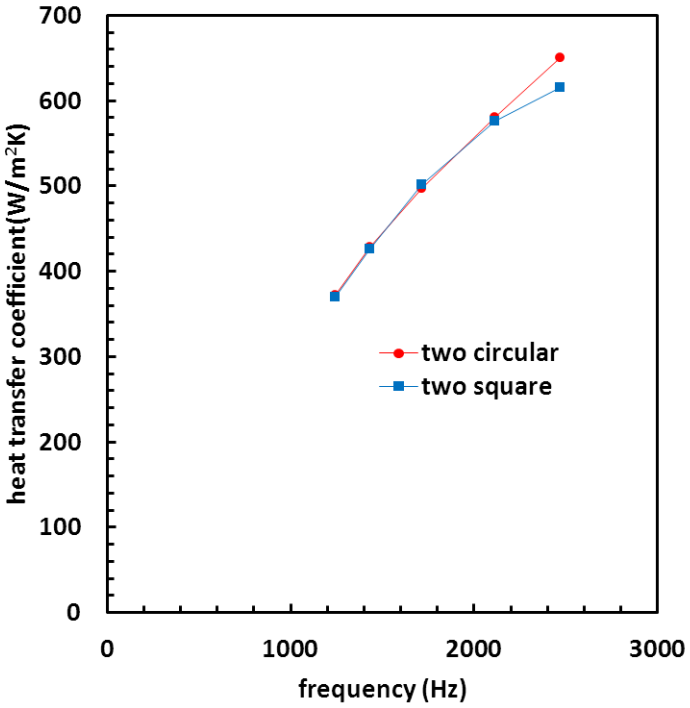

(a) Comparison of surface-average heat transfer coefficients between two circular and two square orifices

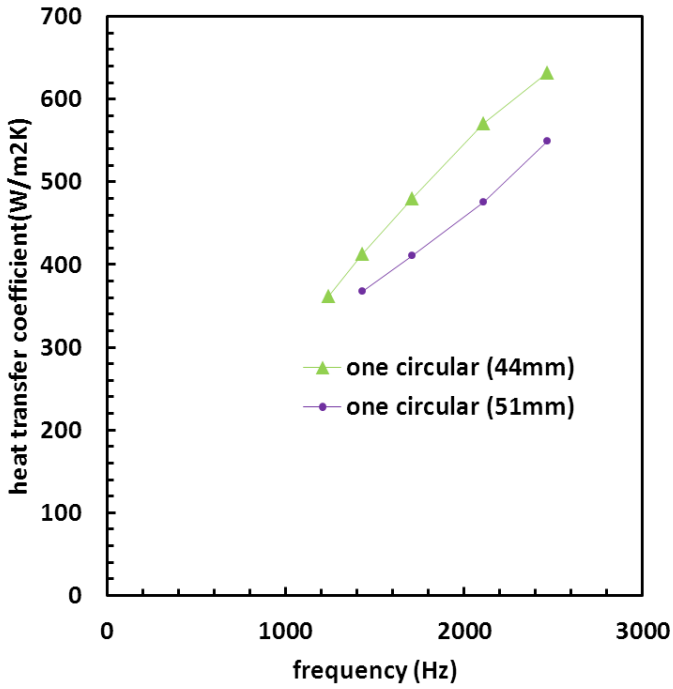

(b) Comparison of surface-average heat transfer coefficients between circular orifices with different orifice diameters

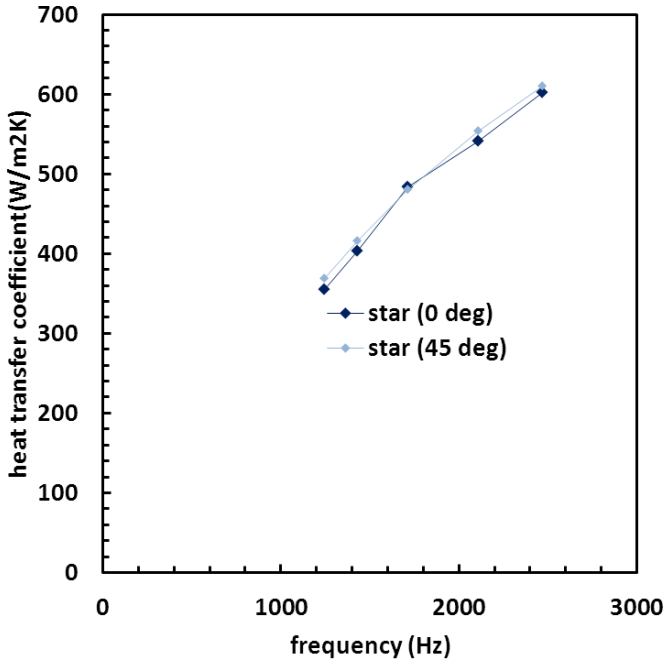

(c) Comparison of surface-average heat transfer coefficients between star orifices with different direction

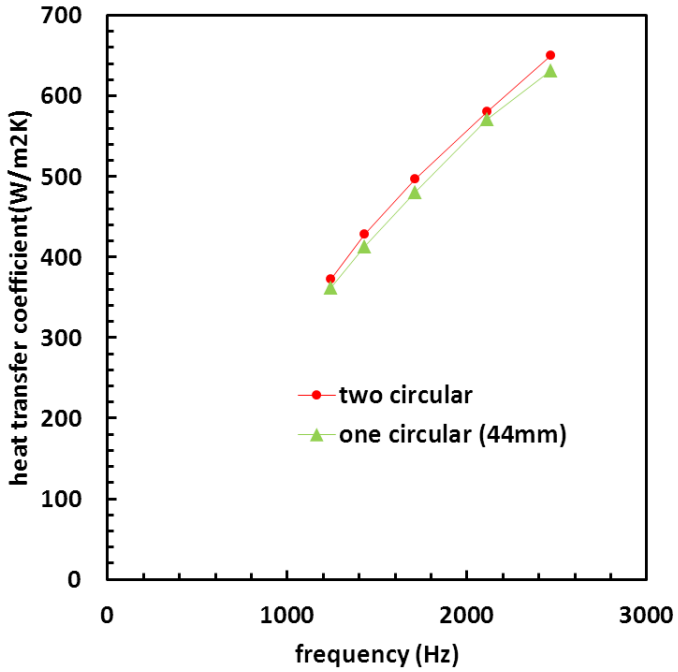

(d) Comparison of surface-average heat transfer coefficients between one circular and two circular orifices

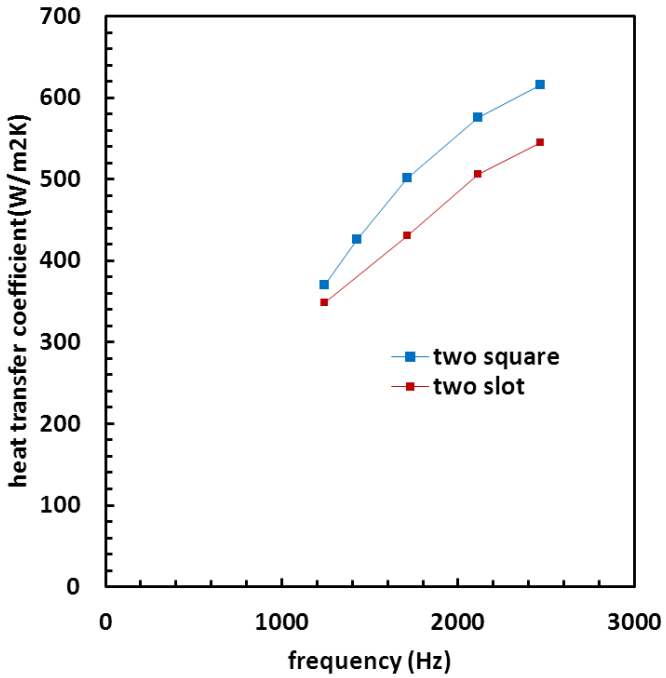

(e) Comparison of surface-average heat transfer coefficients between two square and two slot orifices

Figure 4.3.2 (a)-(e) Comparison of heat transfer coefficients between some specific orifice shapes (The diaphragm amplitude are held constant).

Another study is to investigate the two slot orifice shape with different designs. The dimension of the one slot is 10 × 80 mm^2. The spacing between the two slots is the only changed parameter (Figure 4.3.3) for this study. Four cases have been tested and compared (S = 24 mm, 48 mm, 72 mm, and 96 mm). The heat transfer coefficients for the four cases at different frequencies are shown in Figure 4.3.4. It is found that the heat transfer coefficients increase almost linearly with increases of frequencies for the three cases with a spacing of 24 mm, 48 mm, and 72 mm. For the case with spacing of 96 mm, there is an obvious transition near the frequency of 1429 Hz. In addition, the heat transfer coefficients are close to one another for the all four case at the lowest frequency of 728

Hz, which indicates that the heat transfer coefficient is not sensitive to the orifice shape at low frequencies. The flow visualization is used to support the heat transfer results, which are discussed in section 4.5 of this chapter. The cooling mechanisms of the two-slot orifice can be categorized as following:

(1) The two flows merge into one bulk flow upstream of the round tip, which is like an impinging flow: The round tip has a high heat transfer coefficient, but the flat wall has a lower heat transfer coefficient.

(2) The two flows merge downstream of the fin, which is like two wall jets: The flat wall has a high heat transfer coefficient, but the round tip has a low heat transfer coefficient.

(3) The merging point is near the round tip (most flow covers the fin region): the two flows from the two orifices are impinging on the whole fin.

Flow visualization (Figure 4.3.5-4.3.10) show that the cooling mechanisms are as summarized in Table 4.3.1. For the cases with S values of 24 mm, 48 mm, and 72 mm, the cooling mechanisms are found to be consistent with one another which indicate a linear relationship between the heat transfer coefficient and the frequency. For the case with spacing of 96 mm, the cooling mechanism changes at the frequency of 1429 Hz, which explain the transition of the heat transfer coefficient. Since the two flows are more cooling mechanism 3, relatively higher heat transfer coefficients are expected, relative to those of the other two cooling mechanisms. As a result, the 96 mm case has relatively higher heat transfer performance when the frequency is less than 1429 Hz.

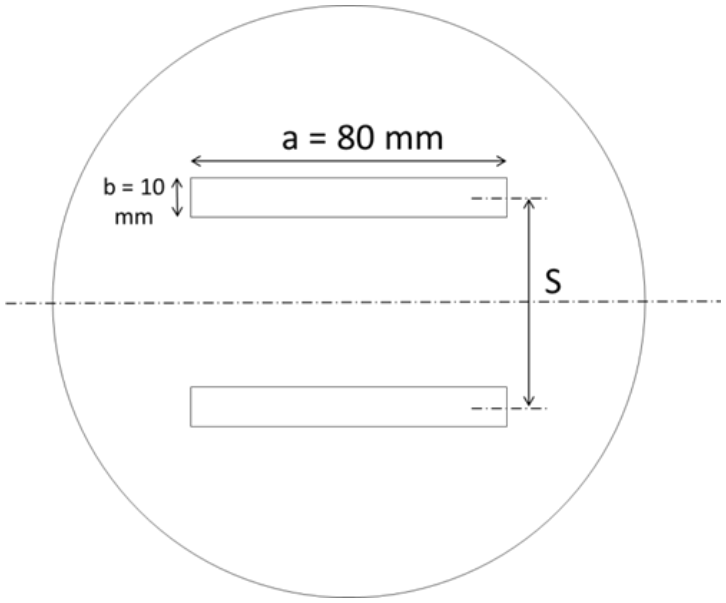

Figure 4.3.3 The dimension of the two slot orifice

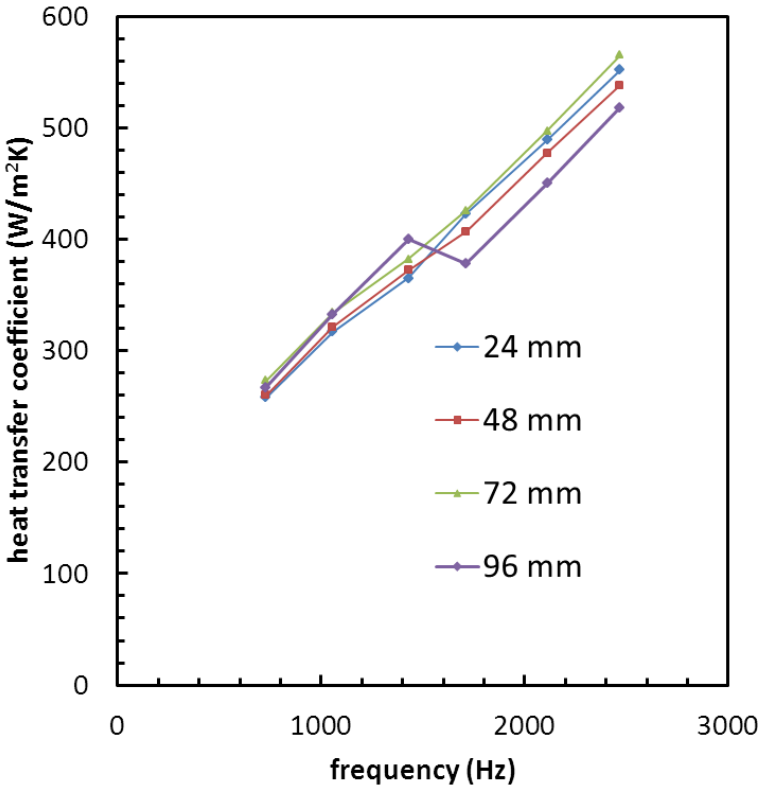

Figure 4.3.4 Surface-averaged heat transfer coefficients for the two slot orifices with different designs

Table 4.3.1 Cooling mechanisms of different cases

	f=728 Hz	f=1056 Hz	f=1429 Hz	f=1713 Hz	f=2112 Hz	f=2469 Hz
24 mm	1	1	1	1	1	1
48 mm	1	1	1	1	1	1
72 mm	1	1	1	1	1	1
96 mm	2	3	3	2	2	2

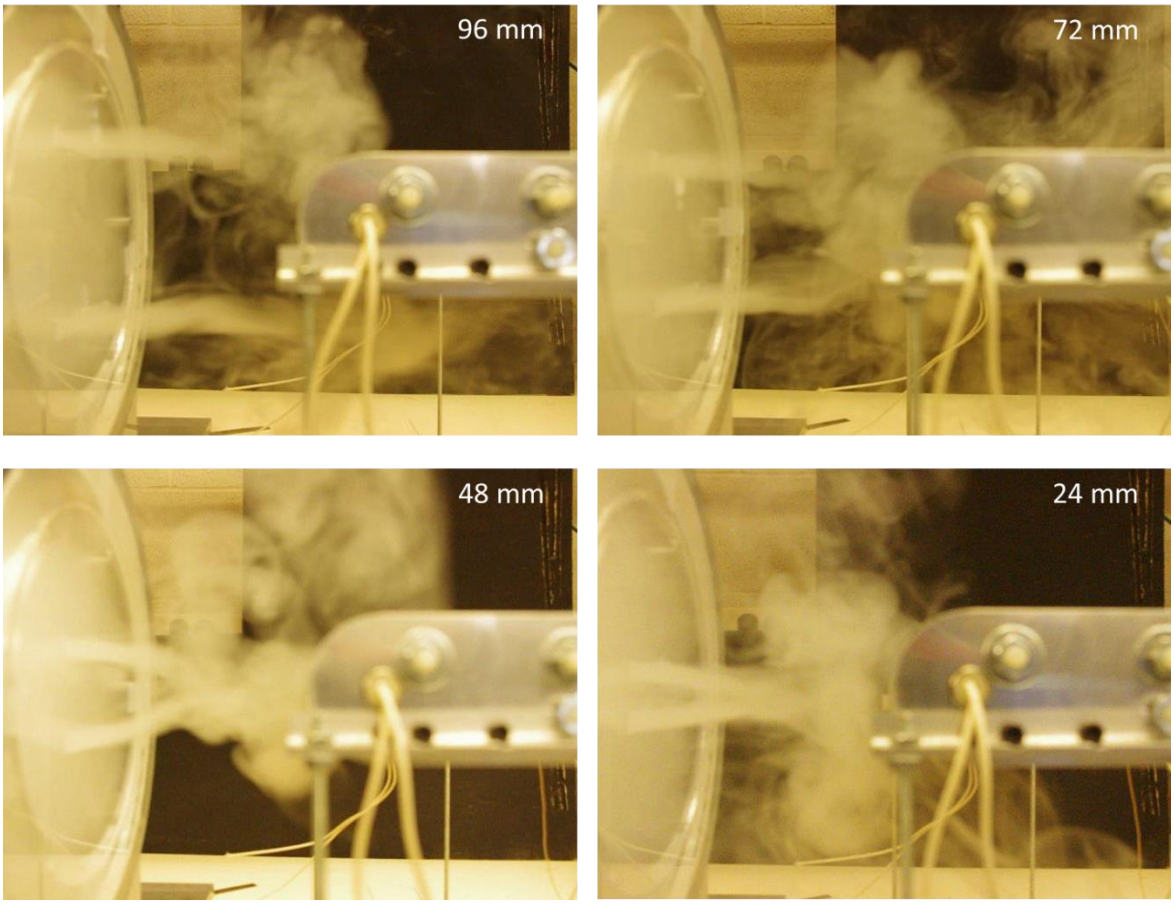

Figure 4.3.5 Flow visualization of all four shapes at a frequency of 728 Hz

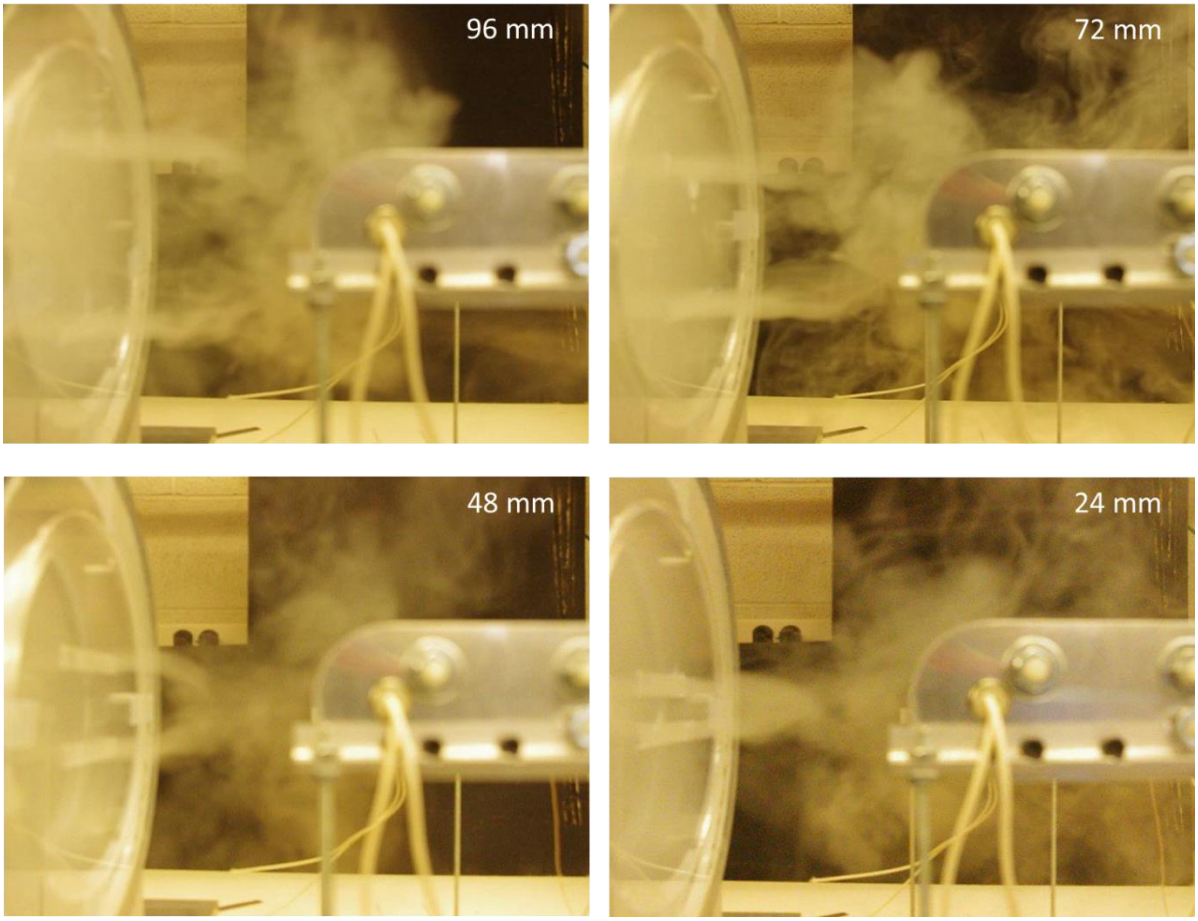

Figure 4.3.6 Flow visualization of all four shapes at a frequency of 1056 Hz

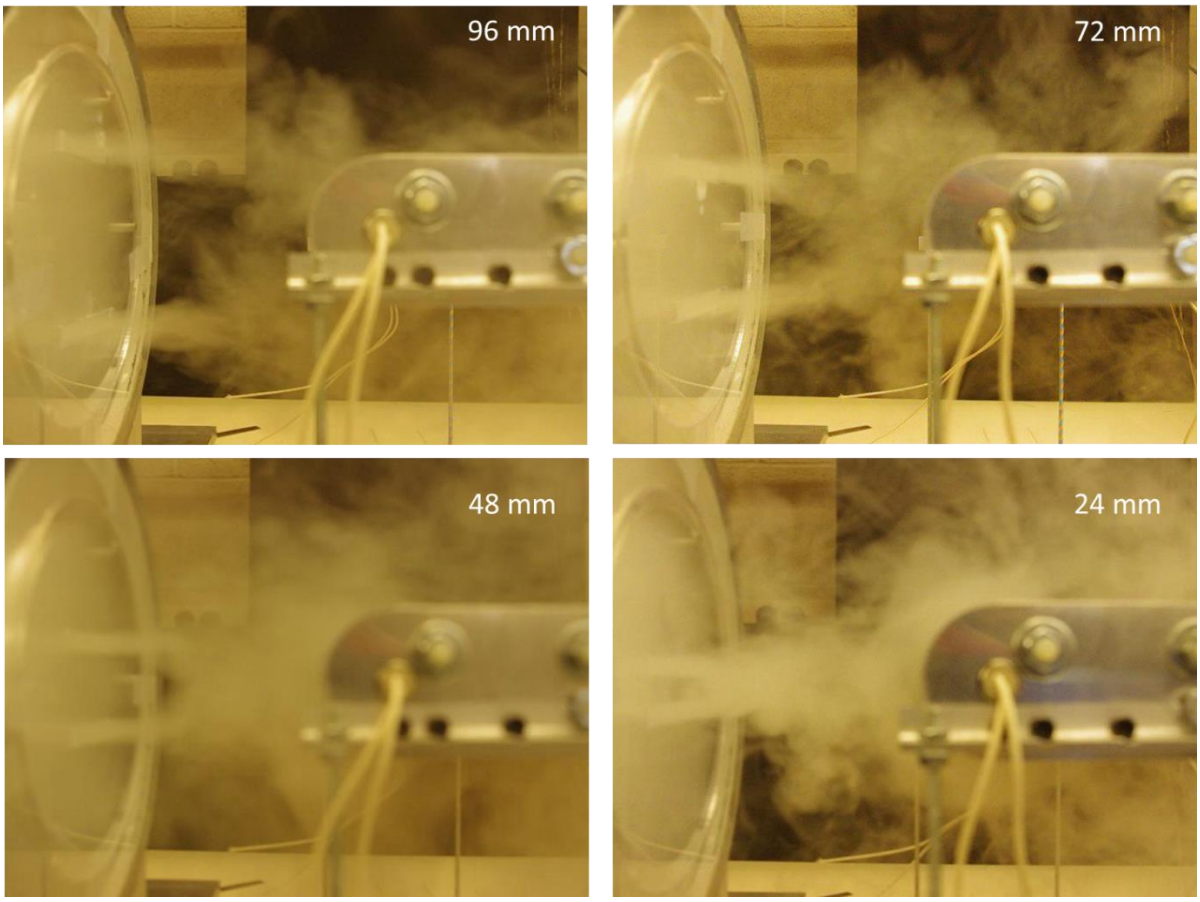

Figure 4.3.7 Flow visualization of all four shapes at a frequency of 1429 Hz

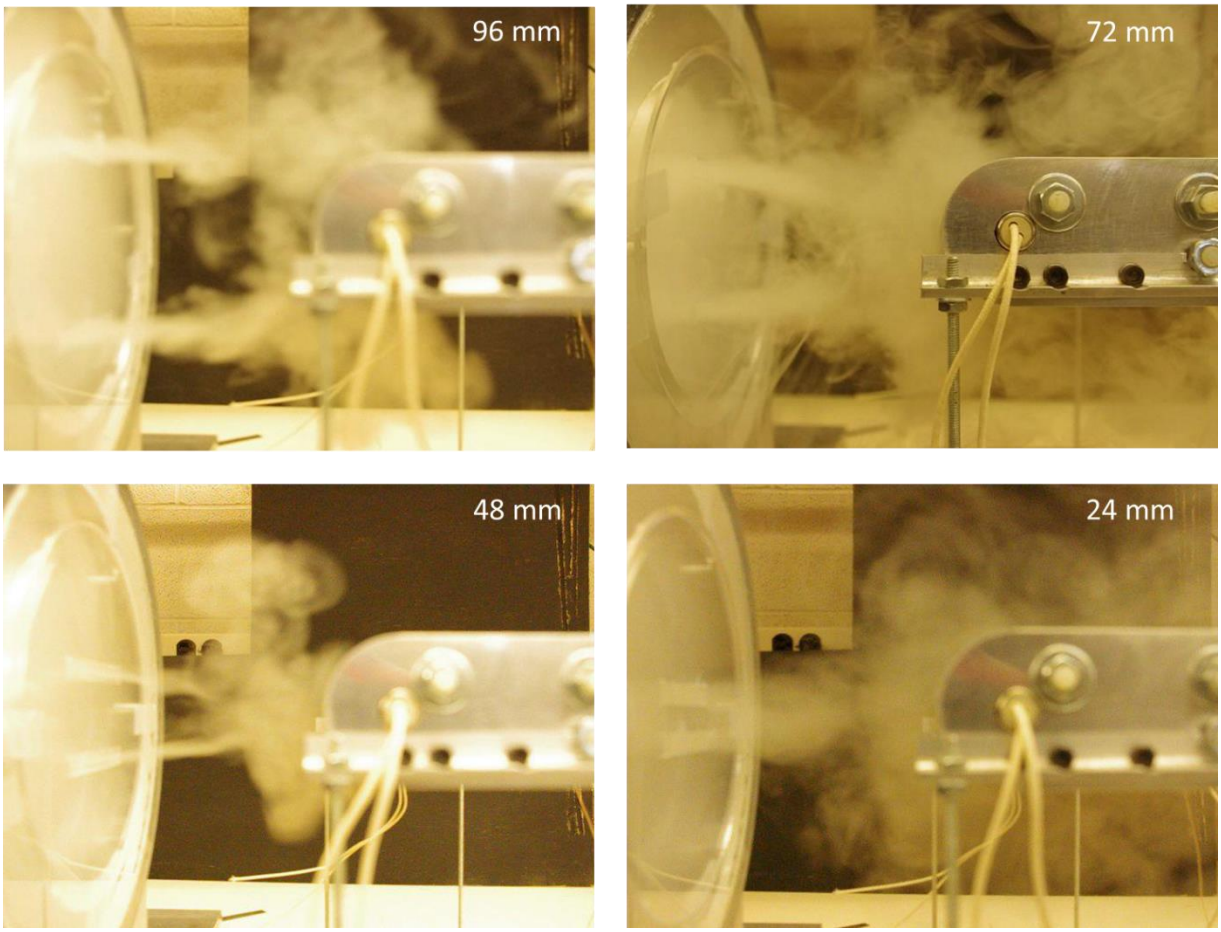

Figure 4.3.8 Flow visualization of all four shapes at a frequency of 1713 Hz

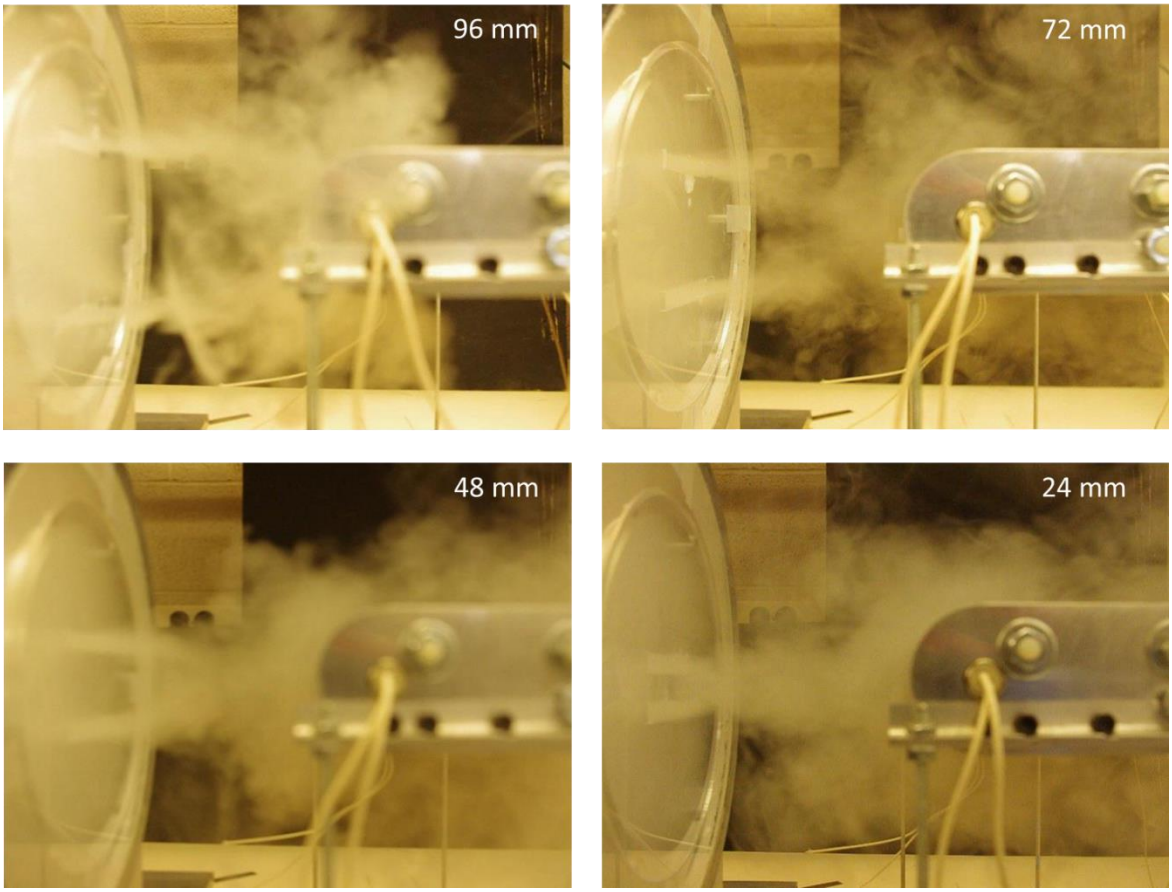

Figure 4.3.9 Flow visualization of all four shapes at a frequency of 2112 Hz

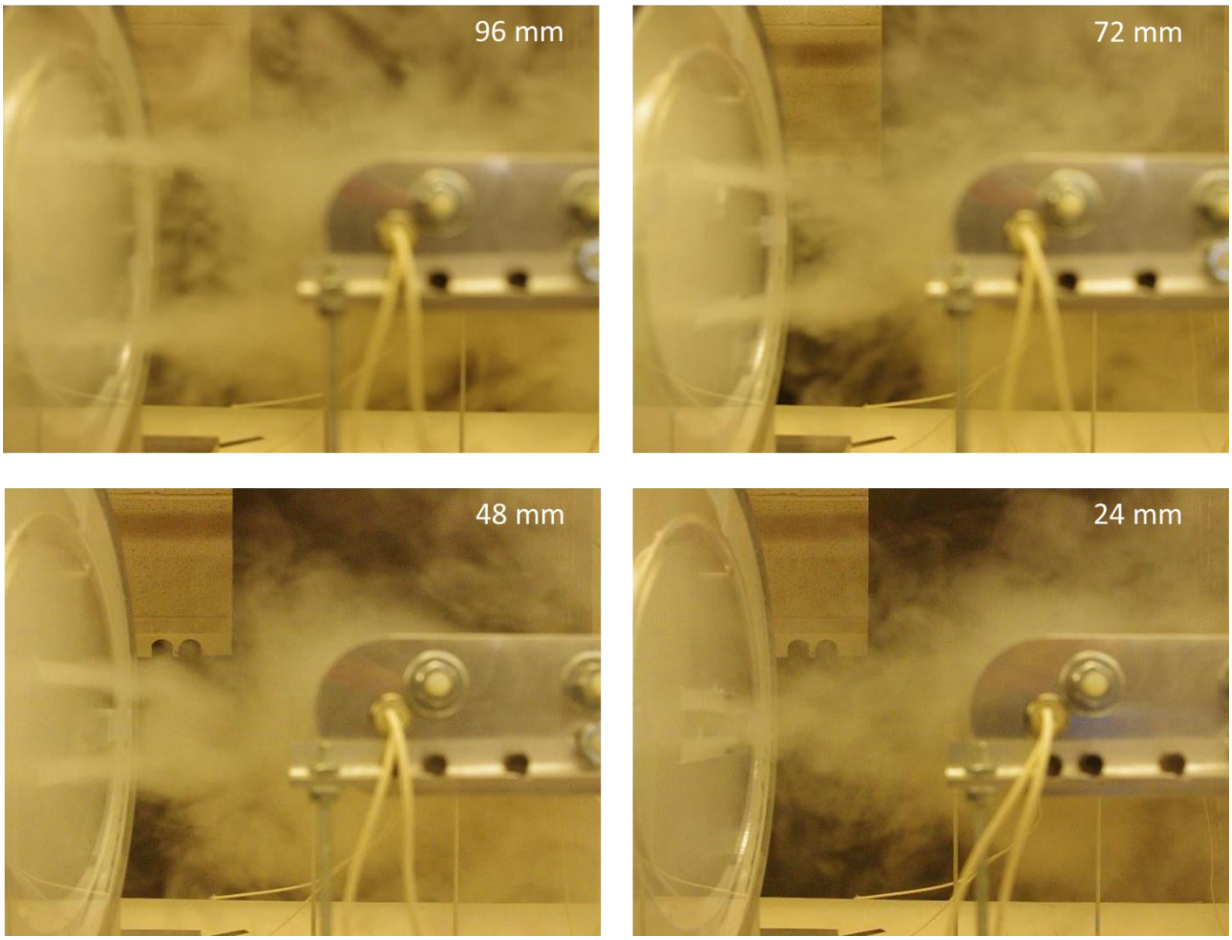

Figure 4.3.10 Flow visualization of all four shapes at a frequency of 2469 Hz

4.4 Flow Visualization

The unsteady flow generated by the synthetic jet has been visualized and recorded by a camera to document the characteristics of the synthetic jet flow. The flow fields of synthetic jets operating at different frequencies have been compared. The flows of the synthetic jets with different orifice shapes have also been compared and documented. The flow field of the synthetic jet impinging on the fin is recorded and used to support the heat transfer measurement (e.g. explains why synthetic jets with different orifices have different heat transfer coefficients).

A fog generator (Figure 4.4.1) is used to generate particles for flow visualization. The chamber is first filled with particles by the fog generator, then the synthetic jet is turned on and the flow is driven out of the orifice to give seeding particles. The particles are light enough to go with the flow, which makes the flow visible. At the same time, the camera records the movement of the particles to visualize the flow field. The picture of each frame is extracted from the video and put together, which is easier to document than the video. The interval of time between each two frames is 0.04s. A blackboard is put behind for better visualization of the whole process.

4.4.1 Flow Visualization without Fin Insert

4.4.1.1 Flow Visualization for Different Frequencies

The typical orifice shape (round one with a diameter of 44 mm) has been used to study the characteristics of synthetic jet flow with different frequencies (Figure 4.4.2 – 4.4.4). Every frame of the flow field has been presented for one cycle. The interval between each two frame is 0.04 s. Cases of three different frequencies (0.56, 0.9, and 1.3

Hz) have been studied and compared. For the low frequency case (f = 0.56 Hz), a starting vortex can be clearly seen near the orifice when the diaphragm is starting to push flow out of the orifice over the first 10 frames (Figure 4.4.2). As the diaphragm continues to move towards the orifice, the vortex moves downstream entraining surrounding air. Finally, these vortices dissipate and the entire flow field is quiescent, because the sink flow (returning to orifice) is much weaker than the discharge flow and has little effect on the flow field far from the orifice when the diaphragm is moving away from the orifice. For the other two frequencies, a similar vortex development is found (Figure 4.4.3 and 4.4.4). However, for the high-frequency case (f = 1.3 Hz), movement of the diaphragm is faster and the peak jet velocity is higher. The starting vortex is not as clear as in the low-frequency case.

4.4.1.2 Flow Visualization for Different Orifices

The frequency is kept the same (f = 0.90 Hz) for the orifice shape study (Figure 4.4.5 – 4.4.8). The orifice type is two-slot case. The dimension of each slot is 10 × 80 mm^2. The only difference is the distance separating the two slots (24 mm, 48 mm, 72 mm, and 96 mm). The slot is relatively narrow with an aspect ratio of 8, which makes the flow field become close to a 2-D flow so that the side view recorded by the camera is very representative of the whole flow field. At the very beginning of each cycle (around first 10 frames), the starting vortices can be clearly seen for all cases. The vortices from the two slots are inclined to induce one another and finally merge together as they move downstream. The closer the two slots are, the more upstream the merging point is. It is clearly seen that the two flows from the two slots merge near the orifice for the 24 mm

case (Figure 4.4.5). However, when the separation distance between the two slots is too far away (the distance between two slots is 96 mm), the two flows will not affect each other and they will move downstream independently (Figure 4.4.8).

4.4.2 Flow Visualization with Fin Insert

Next the fin is added and the flow fields of the synthetic jets impinge on a fin. The distance between the orifice and fin tip is kept at 132 mm for all cases. The cases of a round orifice are presented with three different frequencies (0.556 Hz, 0.90 Hz, and 1.30 Hz) (Figure 4.4.9 – 4.4.11). The diameter of the orifice is 44 mm. The starting vortices are first generated near the orifice at the beginning of the cycle and then move downstream as the diaphragm continues to move toward the orifice. The vortices entrain the surrounding air and finally impinge on the fin to convect the heat from the fin. The core flow first impinges on the round tip forming a stagnation point and goes over the entire fin (Figure 4.4.9) to take the heat away.

The flow fields of the two-slot cases are shown in figure 4.4.12 – 4.4.23. As with the round orifice case, three different frequencies (0.556 Hz, 0.90 Hz, and 1.30 Hz) were studied. For cases with spacings of the two slots between 24 mm, 48 mm, and 72mm, the two flows from the two slots first merge to form one core flow, then impinge on the fin (Figure 4.4.12 – 4.4.19). However, the two flows don't affect each other and impinge on the fin independently which work similar to two wall jets.

Figure 4.4.1 Fog generator

Figure 4.4.2 a. Flow fields of one cycle (f = 0.556 Hz, round orifice, d = 44 mm)

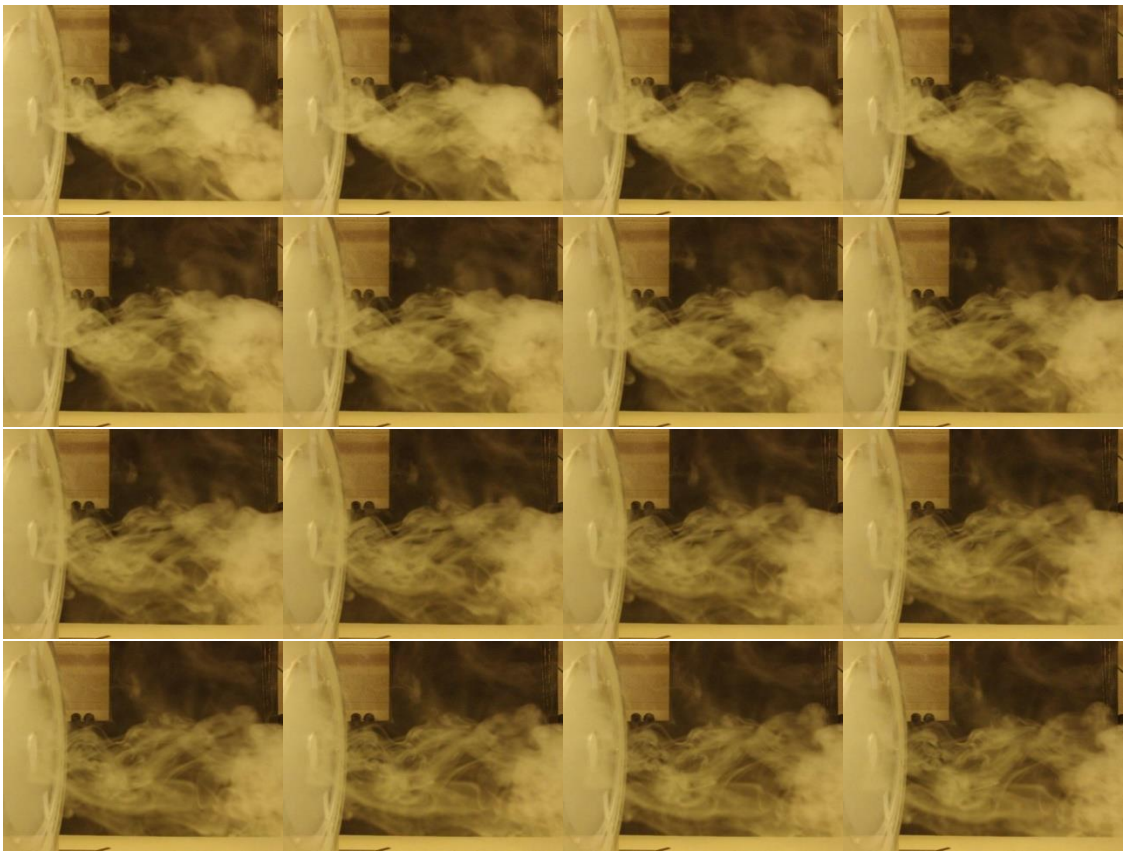

Figure 4.4.2 b. Flow fields of one cycle (f = 0.556 Hz, round orifice, d = 44 mm)

Figure 4.4.3 Flow fields of one cycle (f = 0.90 Hz, round orifice, d = 44 mm)

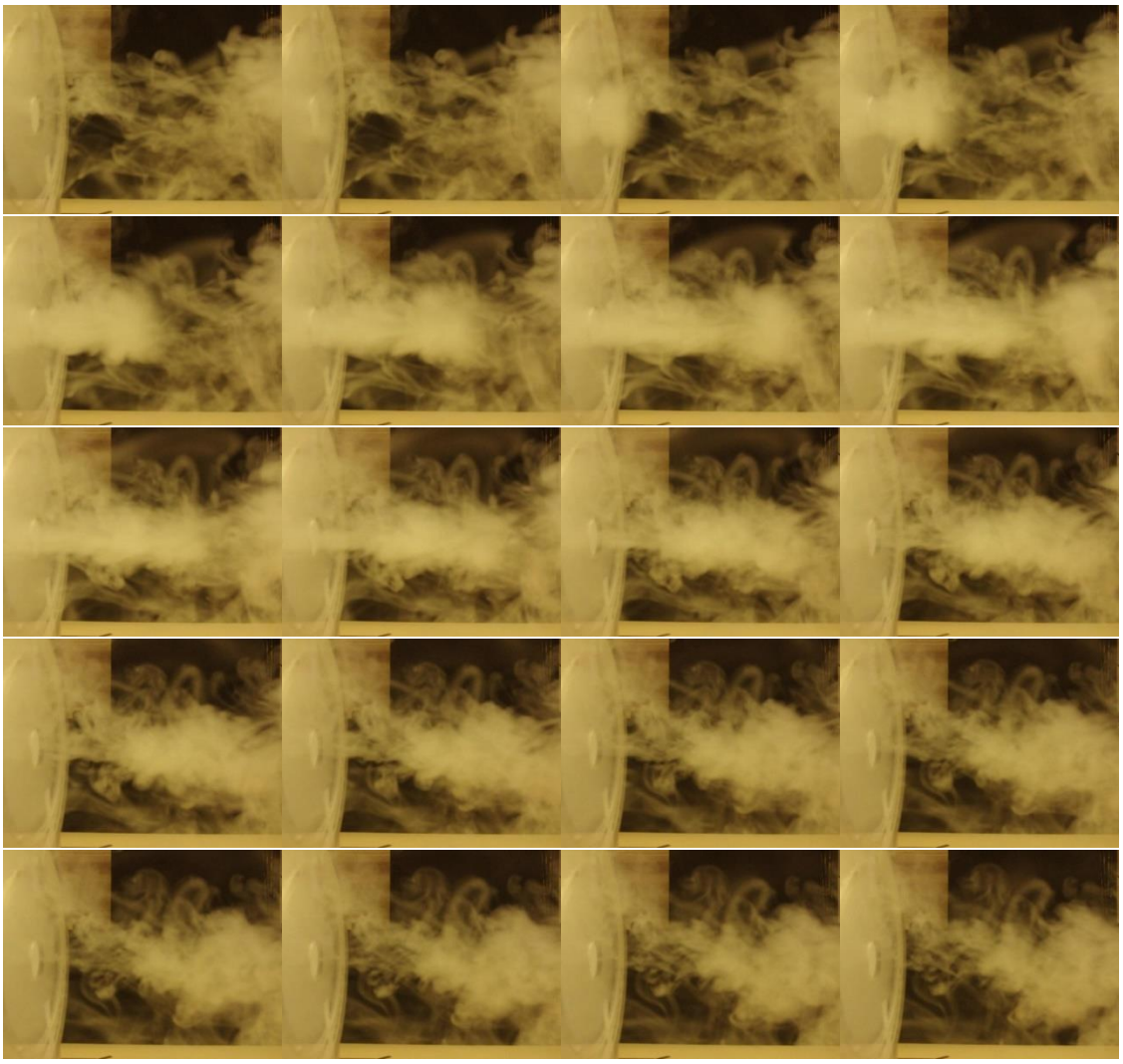

Figure 4.4.4 Flow fields of one cycle (f = 1.30 Hz, round orifice, d = 44 mm)

Figure 4.4.5 Flow fields of one cycle (f = 0.90 Hz, two slot, 10 × 80 mm^2, S = 24 mm)

Figure 4.4.6 Flow fields of one cycle (f = 0.90 Hz, two slot, 10 × 80 mm^2, S = 48 mm)

Figure 4.4.7 Flow fields of one cycle (f = 0.90 Hz, two slot, 10 × 80 mm^2, S = 72 mm)

Figure 4.4.8 Flow fields of one cycle (f = 0.90 Hz, two slot, 10 × 80 mm^2, S = 96 mm)

Figure 4.4.9 a. Flow fields of one cycle with fin insert (f = 0.556 Hz, round orifice, d = 44 mm)

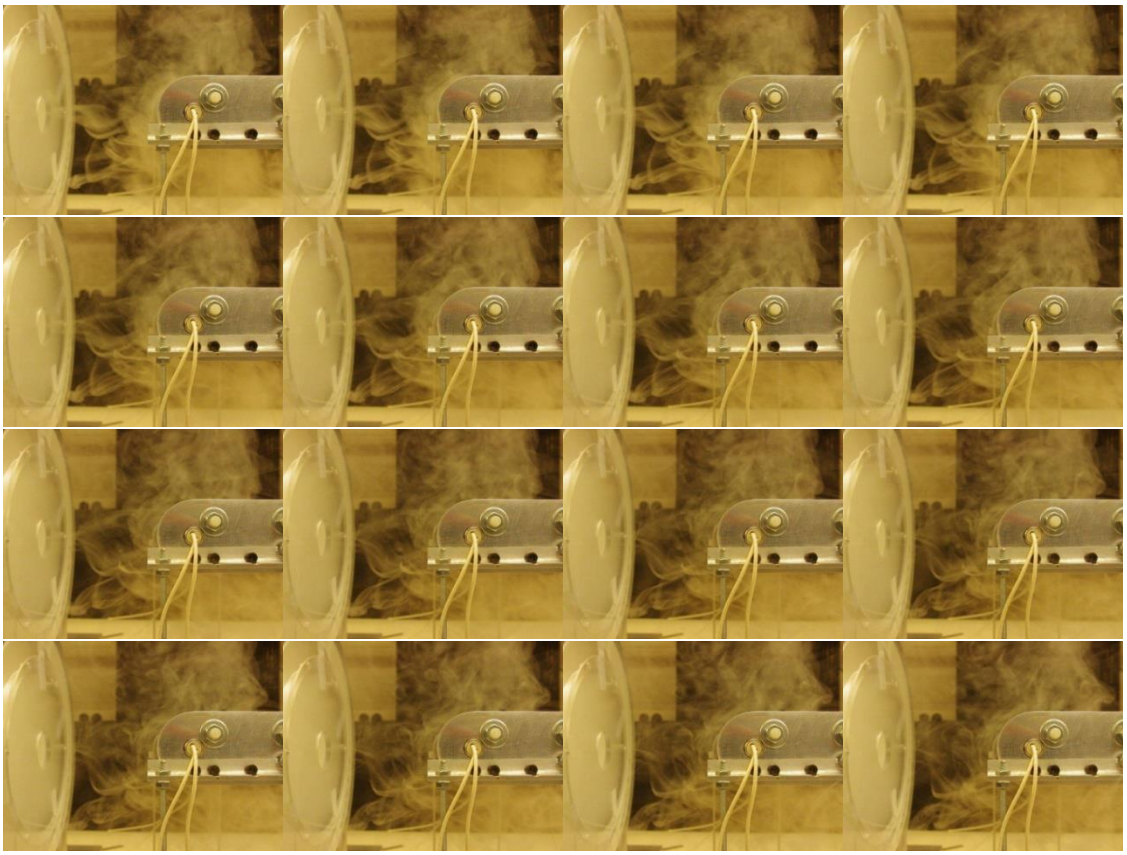

Figure 4.4.9 b. Flow fields of one cycle with fin insert (f = 0.556 Hz, round orifice, d = 44 mm)

Figure 4.4.10 Flow fields of one cycle with fin insert (f = 0.90 Hz, round orifice, d = 44 mm)

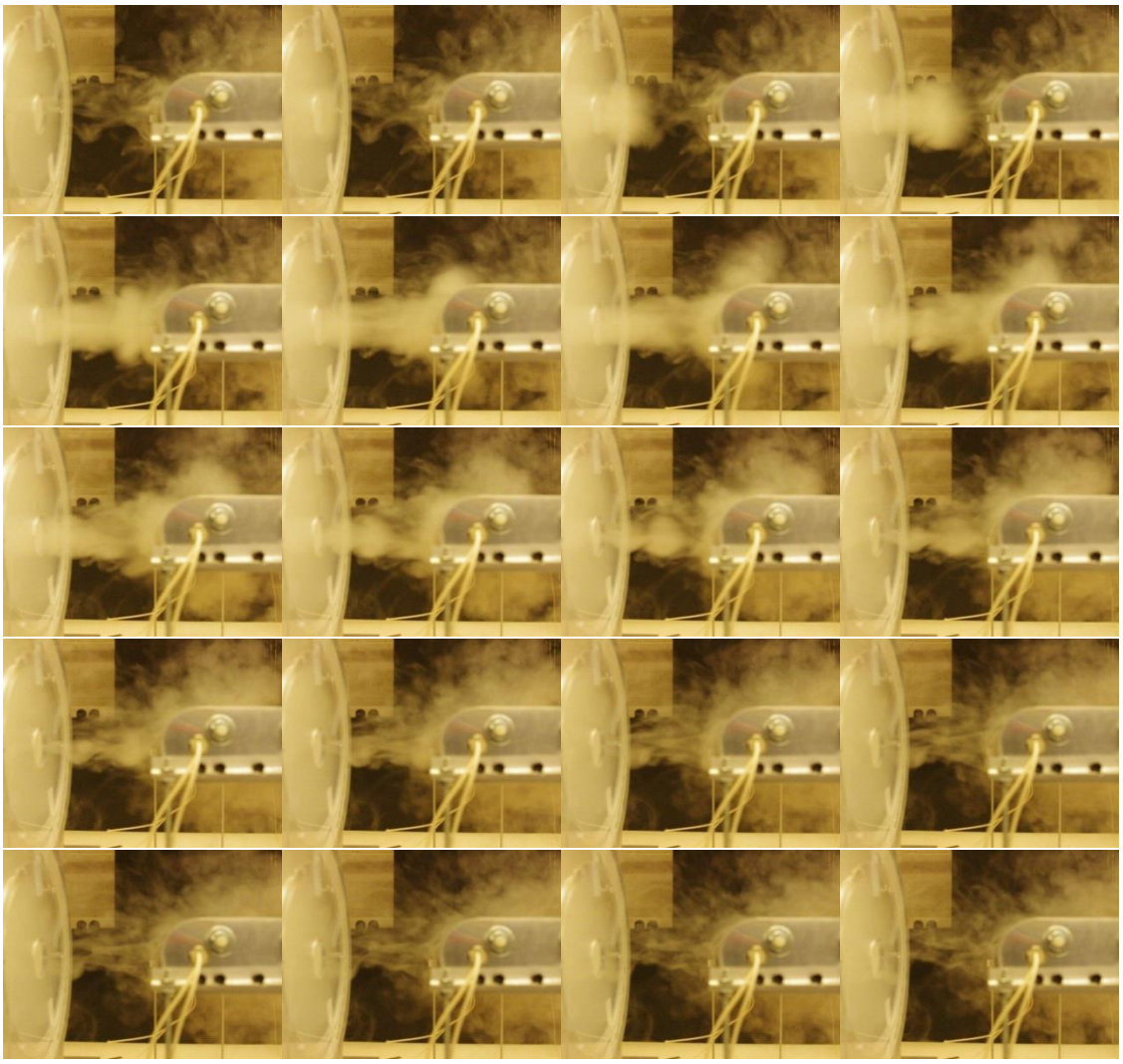

Figure 4.4.11 Flow fields of one cycle with fin insert (f = 1.30 Hz, round orifice, d = 44 mm)

Figure 4.4.12 a. Flow fields with fin insert (f = 0.556 Hz, two slot, 10 × 80 mm^2, S = 24 mm)

Figure 4.4.12 b. Flow fields with fin insert (f = 0.556 Hz, two slot, 10 × 80 mm^2, S = 24 mm)

Figure 4.4.13 Flow fields with fin insert (f = 0.90 Hz, two slot, 10 × 80 mm^2, S = 24 mm)

Figure 4.4.14 Flow fields with fin insert (f = 1.30 Hz, two slot, 10 × 80 mm^2, S = 24 mm)

Figure 4.4.15 a. Flow fields with fin insert (f = 0.556 Hz, two slot, 10 × 80 mm^2, S = 48 mm)

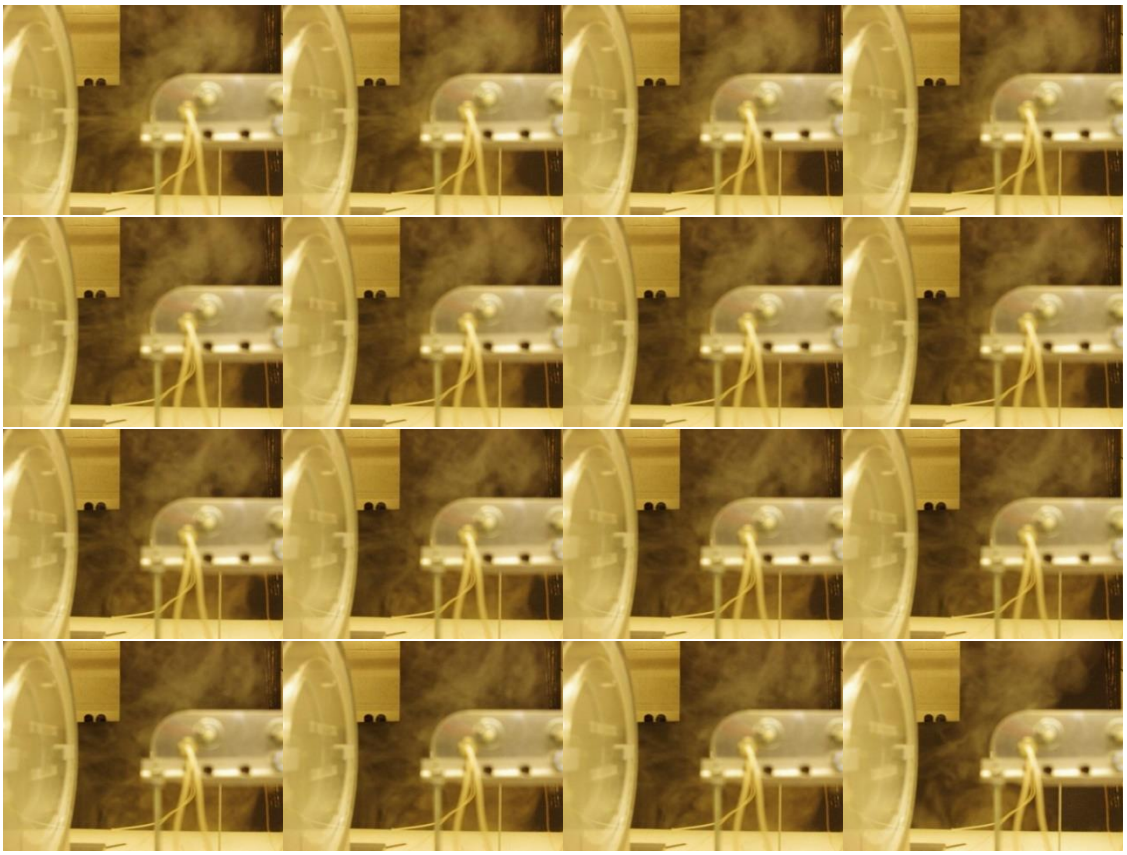

Figure 4.4.15 b. Flow fields with fin insert (f = 0.556 Hz, two slot, 10 × 80 mm^2, S = 48 mm)

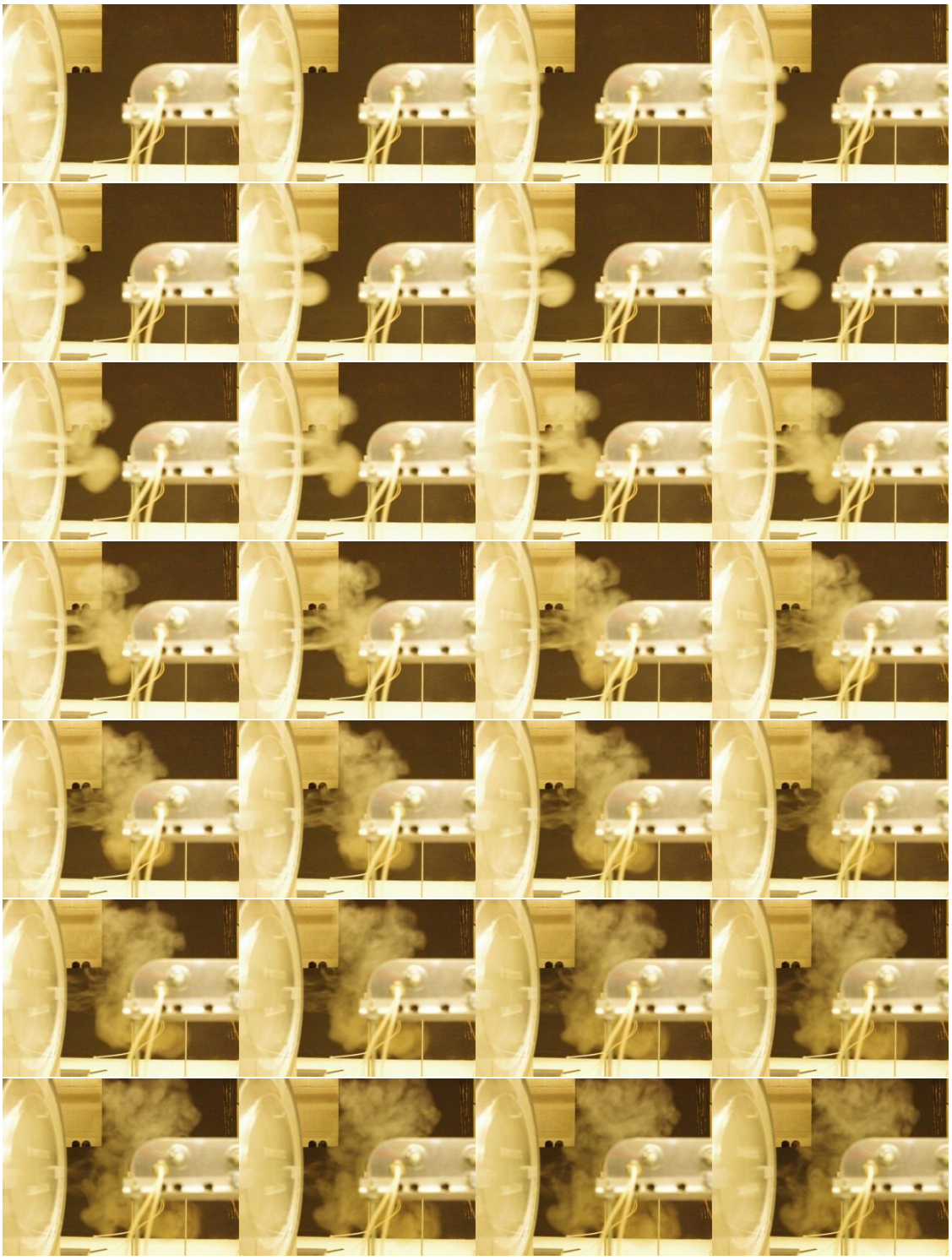

Figure 4.4.16 Flow fields with fin insert (f = 0.90 Hz, two slot, 10 × 80 mm^2, S = 48 mm)

Figure 4.4.17 Flow fields with fin insert (f = 1.30 Hz, two slot, 10 × 80 mm^2, S = 48 mm)

Figure 4.4.18 a. Flow fields with fin insert (f = 0.556 Hz, two slot, 10 × 80 mm^2, S = 72 mm)

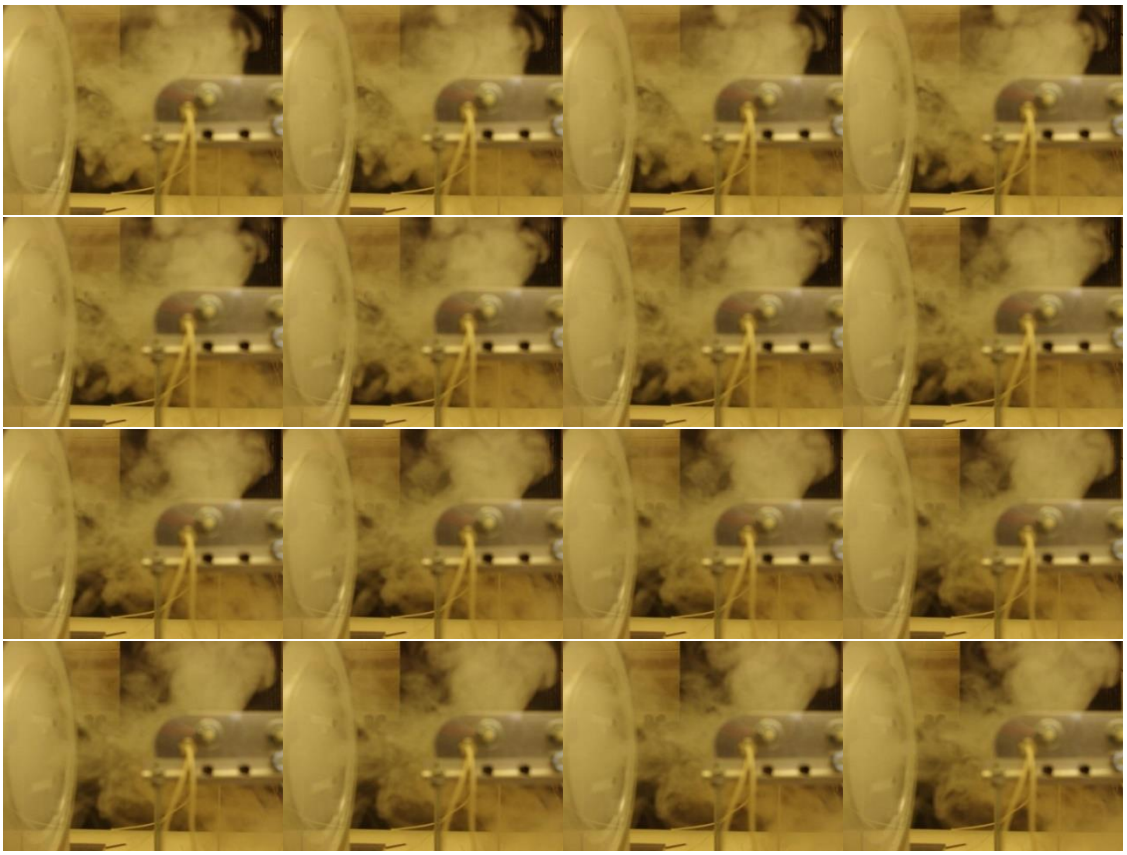

Figure 4.4.18 b. Flow fields with fin insert (f = 0.556 Hz, two slot, 10 × 80 mm^2, S = 72 mm)

Figure 4.4.19 Flow fields with fin insert (f = 0.90 Hz, two slot, 10 × 80 mm^2, S = 72 mm)

Figure 4.4.20 Flow fields with fin insert (f = 1.30 Hz, two slot, 10 × 80 mm^2, S = 72 mm)

Figure 4.4.21 a. Flow fields with fin insert (f = 0.556 Hz, two slot, 10 × 80 mm^2, S = 96 mm)

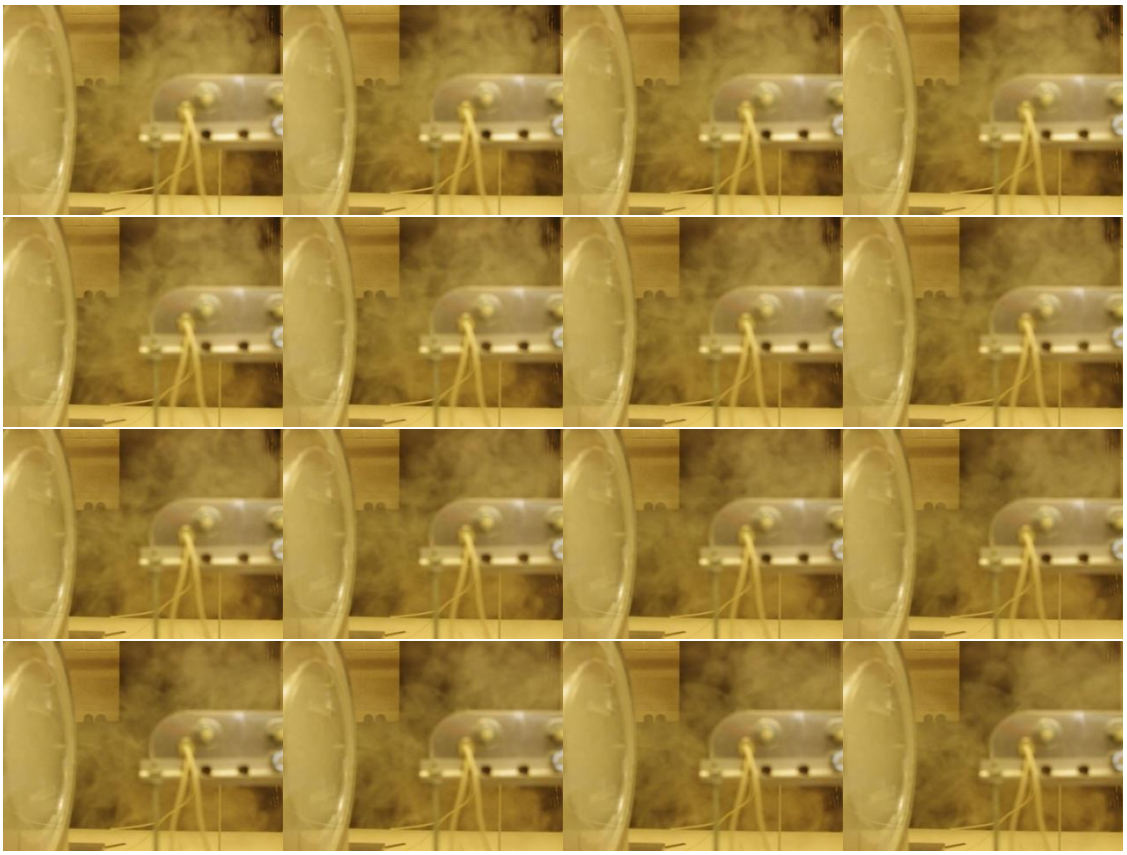

Figure 4.4.21 b. Flow fields with fin insert (f = 0.556 Hz, two slot, 10 × 80 mm^2, S = 96 mm)

Figure 4.4.22 Flow fields with fin insert (f = 0.90 Hz, two slot, 10 × 80 mm^2, S = 96 mm)

Figure 4.4.23 Flow fields with fin insert (f = 1.3 Hz, two slot, 10 × 80 mm^2, S = 96 mm)

4.5 Unsteady Velocity Measurement

The flow visualization has been used to qualify the specific characteristics of the unsteady synthetic jet flow impinging on a fin for cooling. To quantify the flow fields and document the detail information, a TSI TR 60 series, two-component Laser Doppler Velocimetry (LDV) system is used to make detailed velocity measurements (Figure 4.5.1). The LDV system has an Argon Ion laser with a wavelength of 514.5 mm. The diameter of the laser beam is 2.8 mm. The LDV system is able to measure velocities in two directions that are perpendicular to each other. To measure the synthetic jet flow, the probe is put close to the mock-up synthetic jet (Figure 4.5.2), which can be moved to different locations to measure the velocity at various points.

For the flow measurement of a particular point, velocity data are collected for a number of cycles, generally 80. The photo gate (Figure 4.5.2) is able to initiate the time at the beginning of each cycle. Thus, the velocity data for every cycle overlap (Figure 4.5.3) in one cycle which makes the ensemble-average mean velocity and ensemble averaged RMS fluctuating velocity easily calculated. The shape of the figure represents the ensemble-average velocity while the band represents velocity fluctuation (Figure 4.5.3). An ensemble-averaged mean velocity at any instant, t, within the cycle is calculated as:

$$U_{mean}(t) = \frac{1}{n}\sum_{i=1}^{i=n} U_i(t) \qquad (2)$$

where i is the cycle number and t is the particular instant within the cycle. The quantity $U_i(t)$ is a velocity data point from LDV measurement at that particular time for cycle number i.

The ensemble averaged RMS fluctuating velocity is calculated as:

$$U'_{RMS}(t) = \left(\frac{1}{n}\sum_{i=1}^{n}\left(U_{mean}(t) - U_i(t)\right)^2\right)^{1/2} \quad (3)$$

where $U'_{RMS}(t)$ is the ensemble-averaged RMS fluctuating velocity at time, t, within the cycle.

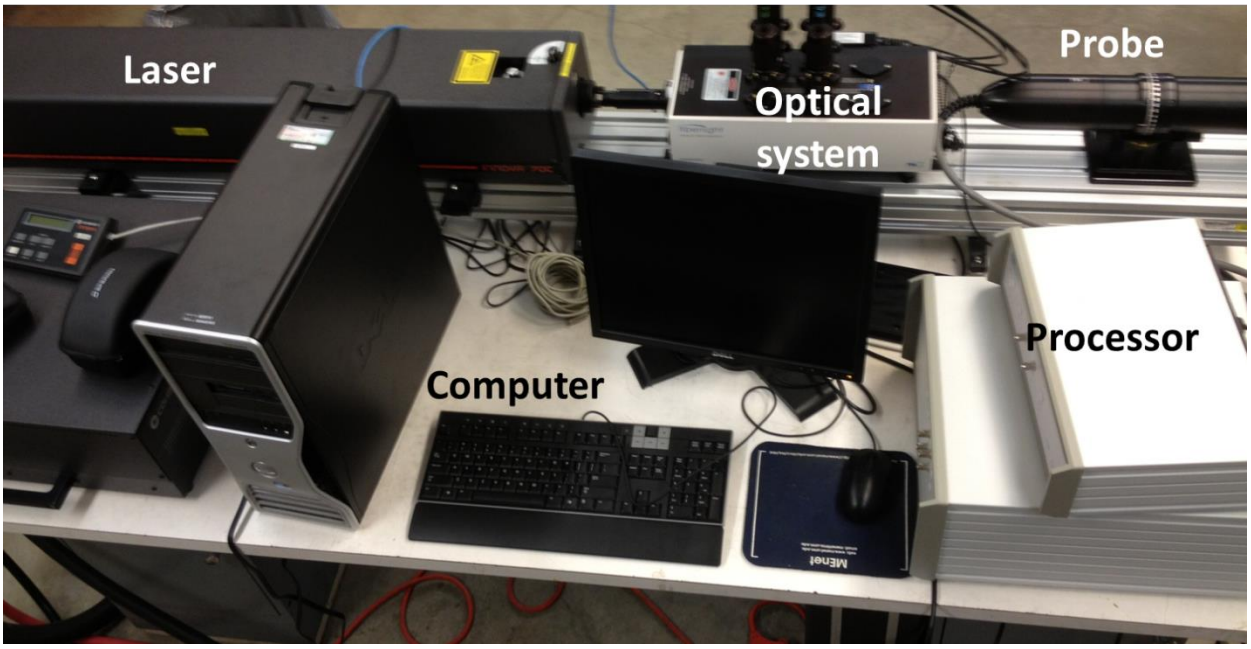

Figure 4.5.1 Laser Doppler Velocimetry (LDV) system

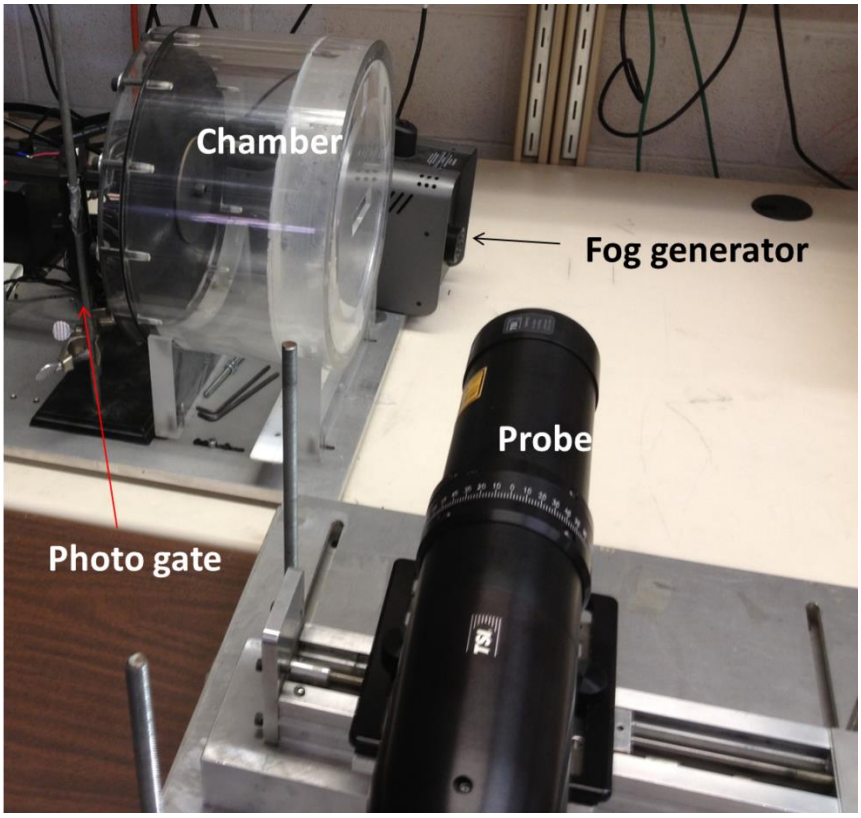

Figure 4.5.2 Velocity measurement test facility

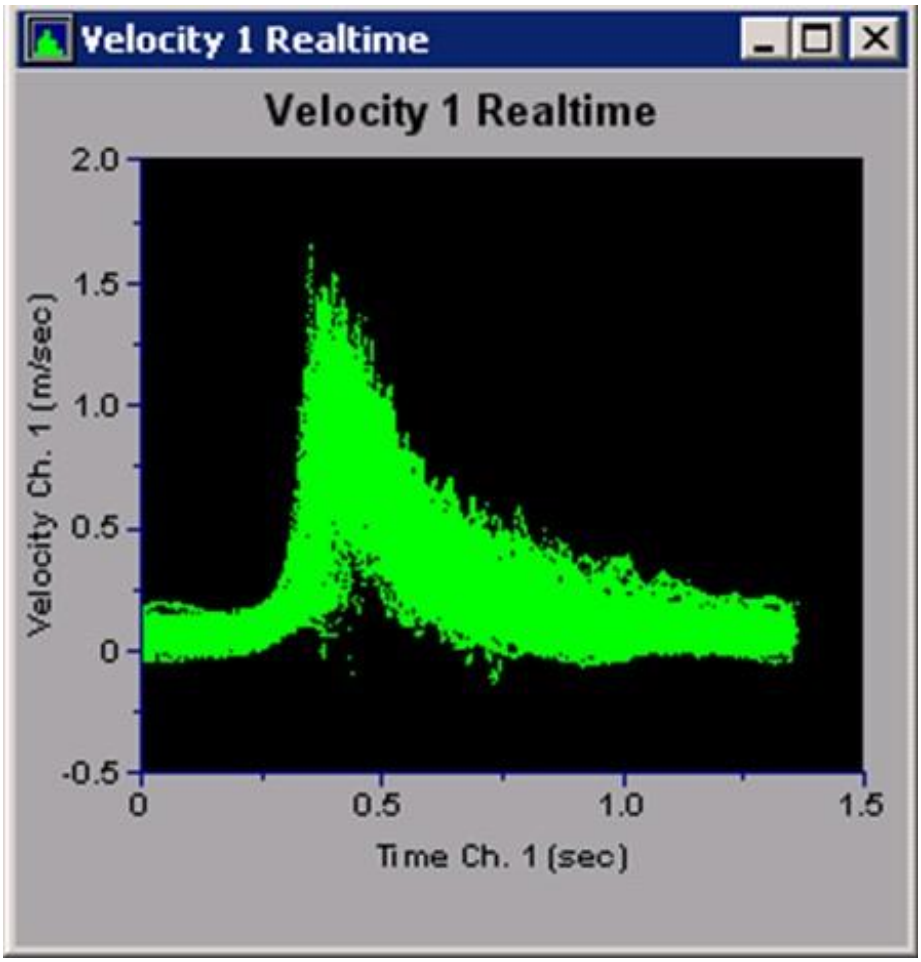

Figure 4.5.3 velocity raw data from the LDV system

A typical case of synthetic jet with a round orifice (d = 44 mm) operating at a frequency of 0.752 Hz was used to study the characteristics of the synthetic jet impinging flow. Since the entire flow field is axisymmetric, the axial surface is representative of the whole flow domain. The measurement map is shown in Figure 4.5.4, in which the crossing points represent the measurement points. In the x-direction, the probe is traversed every 25.4 mm (1 inch) from the orifice 25 mm to 178 mm (1 inch to 7 inch) with 7 points. In the y-direction, the probe is traversed every 6.3 mm (0.25 inch) from the

centerline (0 to 51 mm (2 inch)) with 9 points. Total number of measurement points is 63 (7 × 9).

The ensemble-average velocities in the x direction, the root mean square velocities in the x direction, the ensemble-average velocities in the y direction, and the root mean square velocities in the y direction for all measured points are documented in four separate figures (Figure 4.5.5 – Figure 4.5.8), which make a comparison of the different points easily seen.

At the beginning of the cycle, the whole flow domain is quiescent and the velocity of each figure starts with a velocity of near 0 m/s. When the diaphragm starts to move toward the orifice and push the flow out of the orifice, as the time increases, a bulk flow jets out and moves downstream.

In the core region near the centerline (0 mm < y < 19 mm (0.75 inch)), a mountain shape can be clearly seen in the velocity plots for the ensemble-average in x the direction (Figure 4.5.5) as the bulk flow is moving through those points. However, the peak velocity decreases as the bulk flow moves downstream (x > 76 mm (3 inch)) due to the friction by the surrounding quit flow. Velocity fluctuations in x the direction of the points in this region are relatively higher than those of the points in other regions (Figure 4.5.6). However, the velocities and velocity fluctuations are very low in the y direction. The values of the ensemble-averaged velocities in the y direction are almost zero for the whole cycle (Figure 4.5.7). The velocity fluctuations in the y direction for this region are found to be lower than those of other regions (Figure 4.5.8).

In the shear layer region (19 mm (0.75 inch) < y < 38 mm (1.5 inch)), the jetting flow out of the orifice starts to entrain the quiescent surrounding fluid and form vortices, which moves downstream. In the region in which the distance from the orifice is less than 25.4 mm (x <25.4 mm (1 inch)) the flow has a very low momentum (Figure 4.5.5). As the vortices move downstream, the magnitudes of velocities in both x and y directions increase (Figure 4.5.5 and 4.5.6). The velocity fluctuations are found to increase also (Figure 4.5.7 and 4.5.8). However, in the region downstream of the orifice (x > 127 mm (5 inch)), the magnitudes of the ensemble-average velocity and velocity fluctuations decrease, due the turbulence dissipation.

In the region far downstream the centerline (38 mm (1.5 inch) < y < 51 mm (2 inch)), the flow domain is relatively quiescent. Both ensemble-average velocities and velocity fluctuations are at a lower level than in other regions. However, as the shear layer grows, the flow region with an x value larger than 127 mm (5 inch) is agitated and the velocity fluctuations can be clearly seen.

4.6 Conclusions

The heat transfer and fluid mechanics characteristics of a synthetic jet have been investigated by a mock-up synthetic jet test facility. It is 44 times that of the actual one causing the frequency of the mock-up jet $1/44^2$ the actual frequency. The average heat transfer coefficients over the fin increase almost linearly with increases of operating frequency of the synthetic jet. The case with two circular orifices is found to provide the highest heat transfer performance among all orifice geometries studied (square, two square, circular, two circulars, slot, two slots, and star shape). The unsteady flow

characteristics and development of synthetic jet impinging flow are visualized using a smoke generator and a camera. The starting vortices and their developments are documented in detail. Flow visualization of the two-slot synthetic are used to support the heat transfer trends. The ensemble-averaged velocities and the Root Mean Square (RMS) velocities measured by a Laser Doppler Velocimetry (LDV) system are used to capture the flow characteristics. In the shear layer region, the RMS velocities are found to be in a high level due to the development of the starting vortices. However, in the region of far field, both ensemble-averaged velocities and RMS velocity fluctuations are at a low level due to turbulence dissipation.

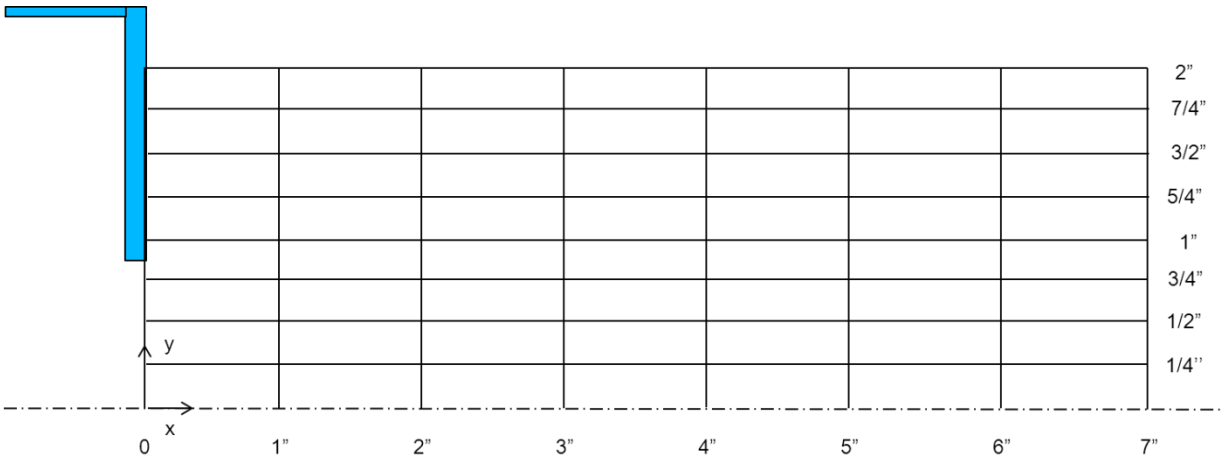

Figure 4.5.4 Grids of the axisymmetric plane for the velocity measurements of the synthetic jet with a round orifice

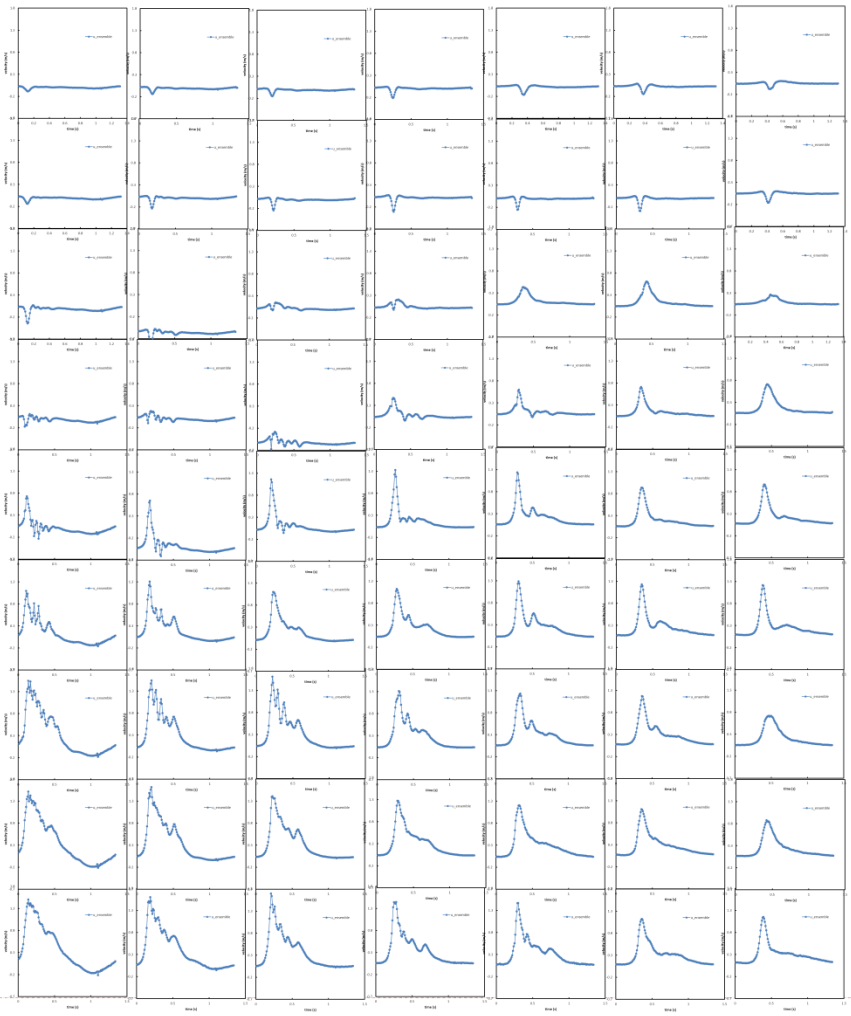

Figure 4.5.5 Overview ensemble average velocity of one cycle in x-direction for all points within the measurement map (the orifice is round with a diameter of 44 mm, the frequency is 0.752 Hz)

(Horizontal direction represents x-direction; vertical direction represents y-direction)

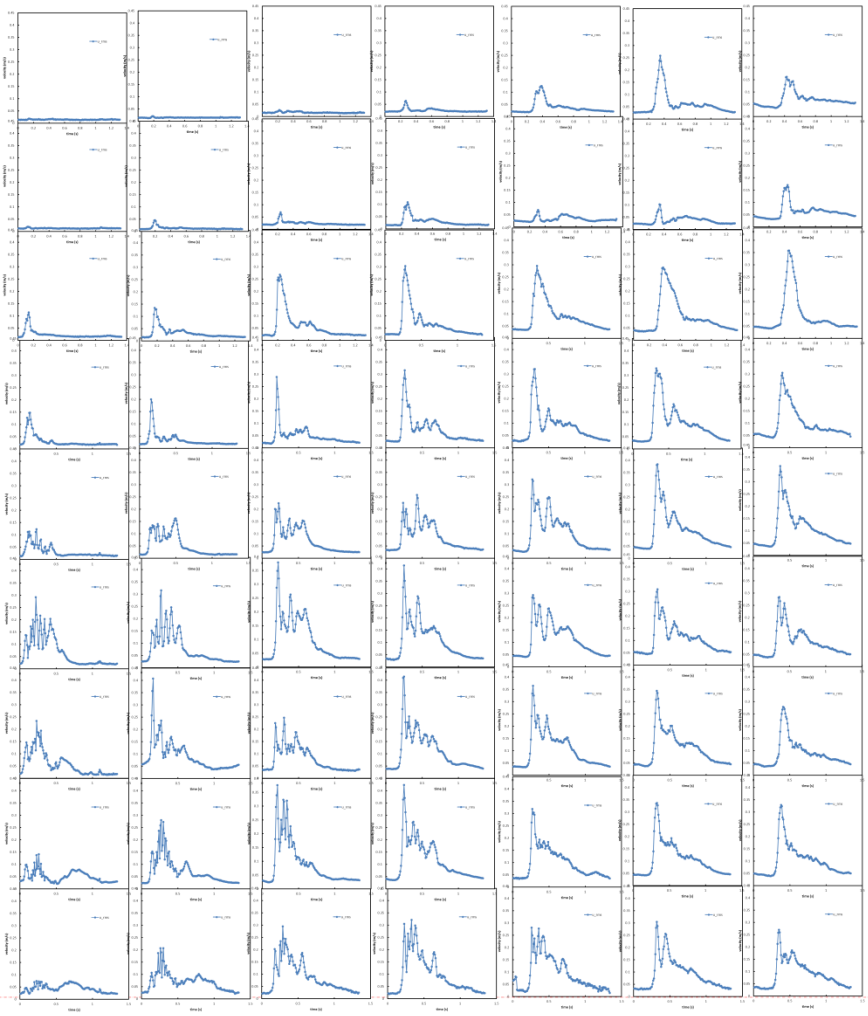

Figure 4.5.6 Overview root mean square (RMS) velocity of one cycle in x-direction for all points within the measurement map (the orifice is round with a diameter of 44 mm, the frequency is 0.752 Hz)

(Horizontal direction represents x-direction; vertical direction represents y-direction)

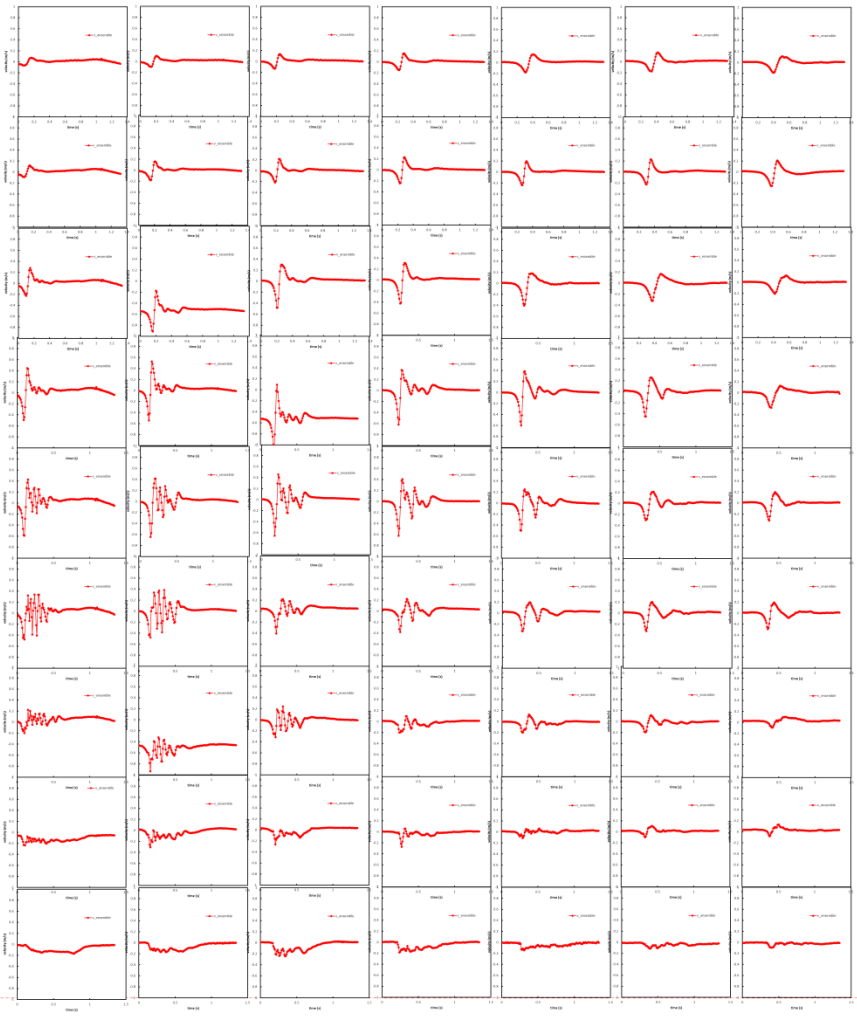

Figure 4.5.7 Overview ensemble average velocity of one cycle in y-direction for all points within the measurement map (the orifice is round with a diameter of 44 mm, the frequency is 0.752 Hz)

(Horizontal direction represents x-direction; vertical direction represents y-direction)

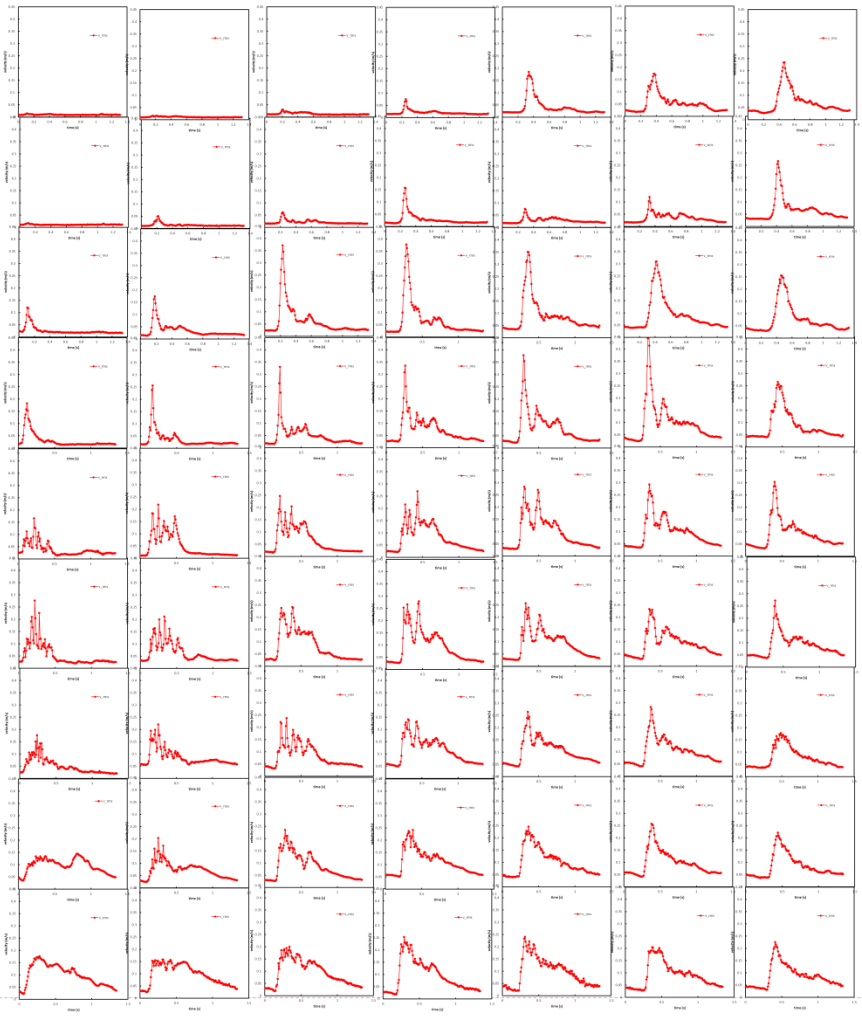

Figure 4.5.8 Overview root mean square (RMS) velocity of one cycle in y-direction for all points within the measurement map (the orifice is round with a diameter of 44 mm, the frequency is 0.752 Hz)

(Horizontal direction represents x-direction; vertical direction represents y-direction)

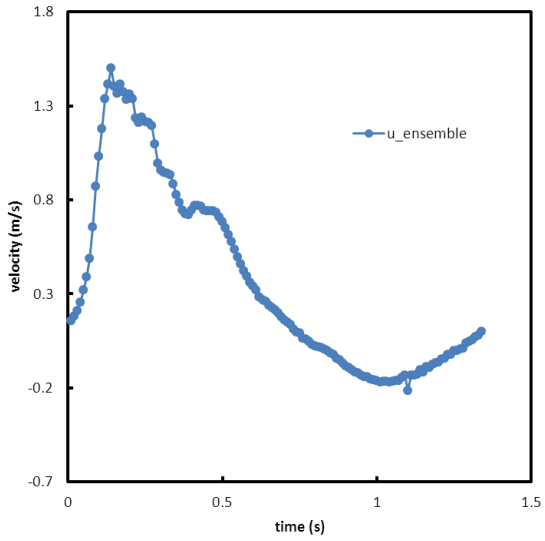

(x = 1 inch, y = 0 inch)

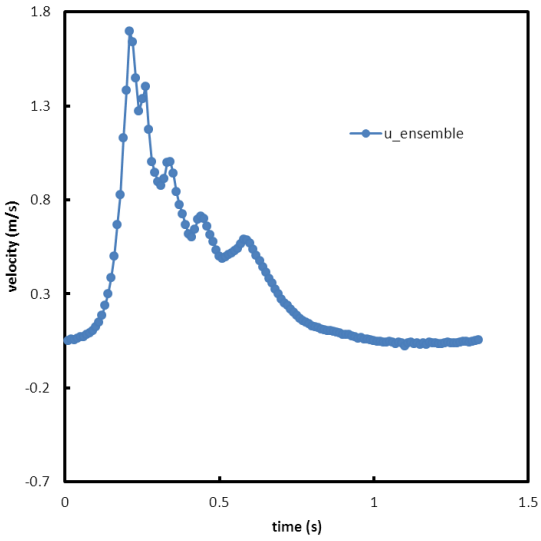

(x = 3 inch, y = 0 inch)

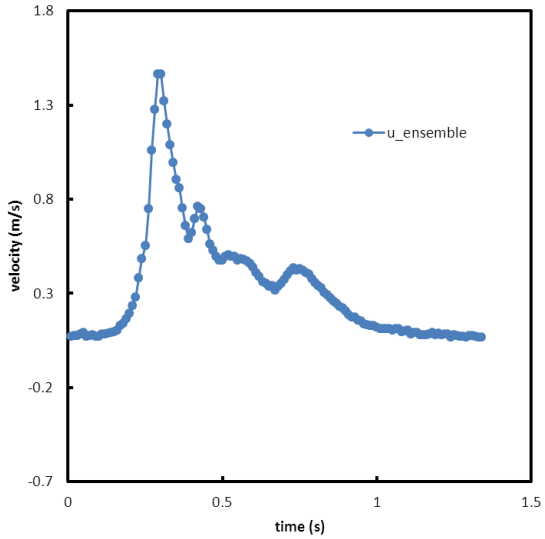

(x = 5 inch, y = 0 inch)

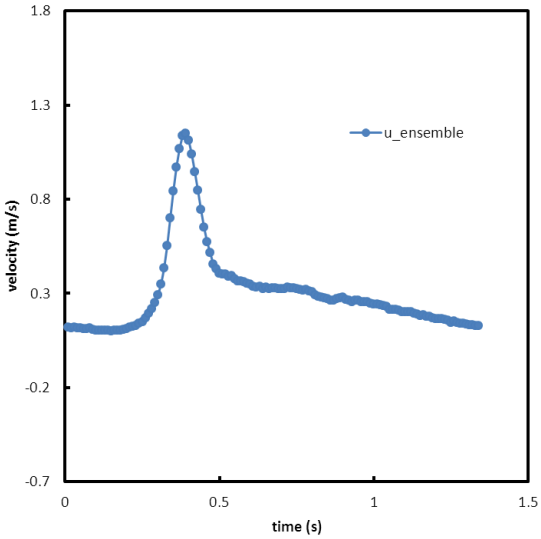

(x = 7 inch, y = 0 inch)

Figure 4.5.9 (a) Detail ensemble average velocities of one cycle in x-direction for different points

(x = 25 mm~178 mm (1~7 inch); y = 0 mm (0 inch))

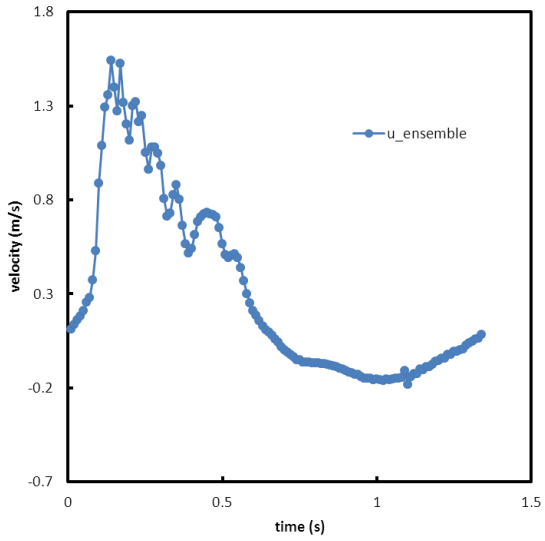

(x = 1 inch, y = 0.5 inch)

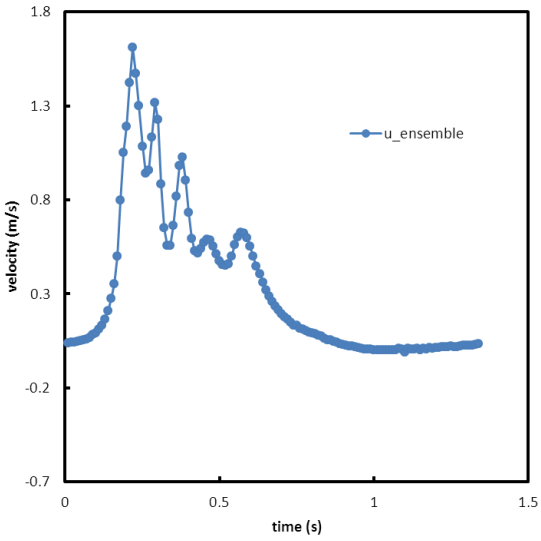

(x = 3 inch, y = 0.5 inch)

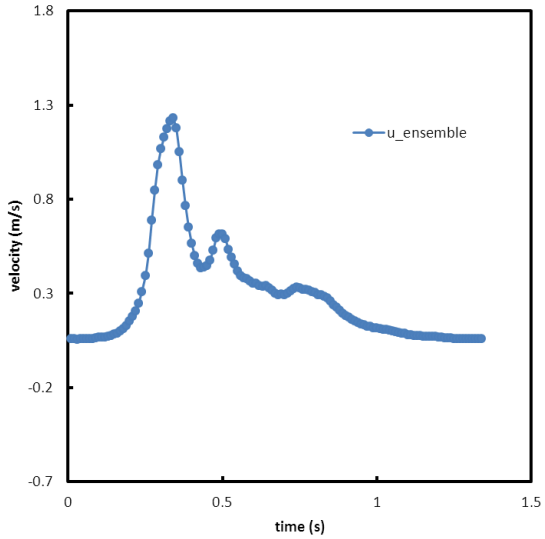

(x = 5 inch, y = 0.5 inch)

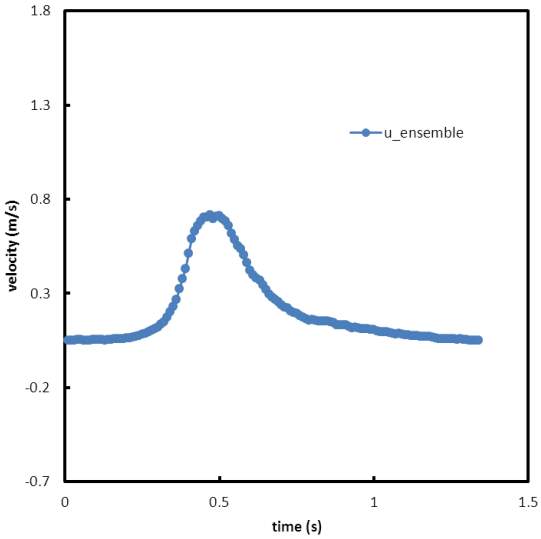

(x = 7 inch, y = 0.5 inch)

Figure 4.5.9 (b) Detail ensemble average velocities of one cycle in x-direction for different points

(x = 25 mm~178 mm (1~7 inch); y = 13 mm (0.5 inch))

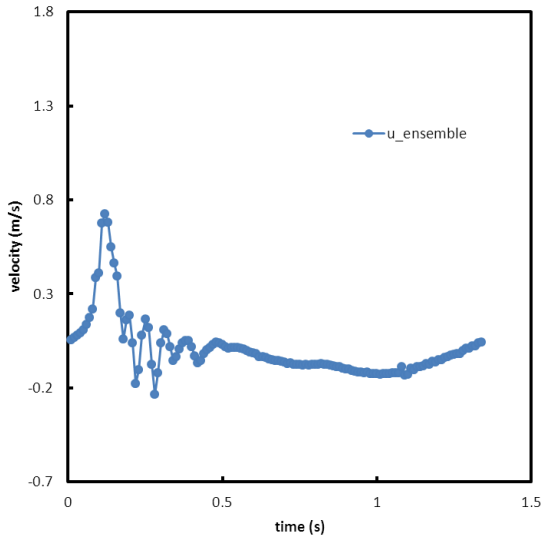

(x = 1 inch, y = 1 inch)

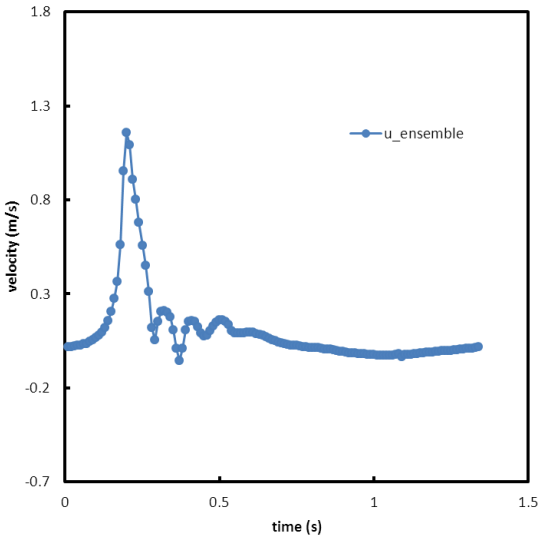

(x = 3 inch, y = 1 inch)

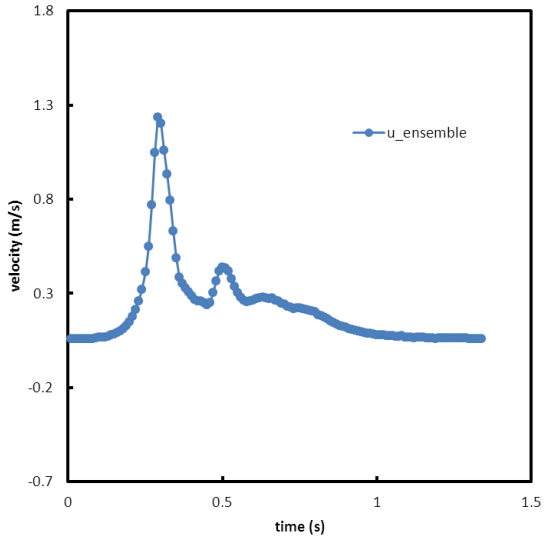

(x = 5 inch, y = 1 inch)

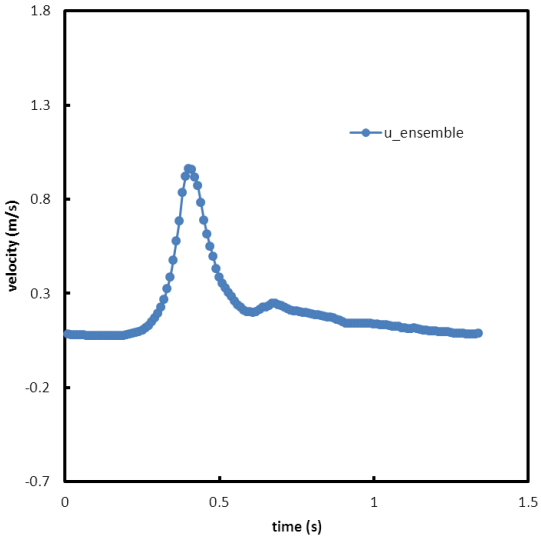

(x = 7 inch, y = 1 inch)

Figure 4.5.9 (c) Detail ensemble average velocities of one cycle in x-direction for different points

(x = 25 mm~178 mm (1~7 inch); y = 25 mm (1 inch))

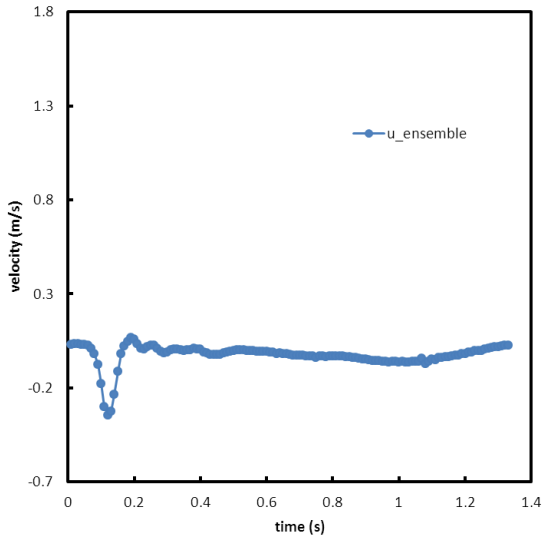

(x = 1 inch, y = 1.5 inch)

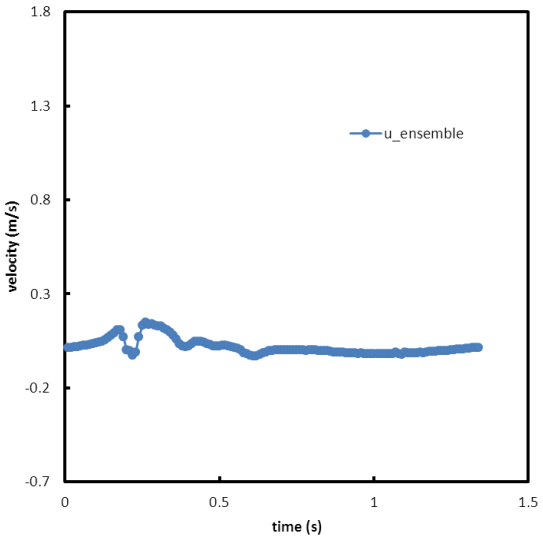

(x = 3 inch, y = 1.5 inch)

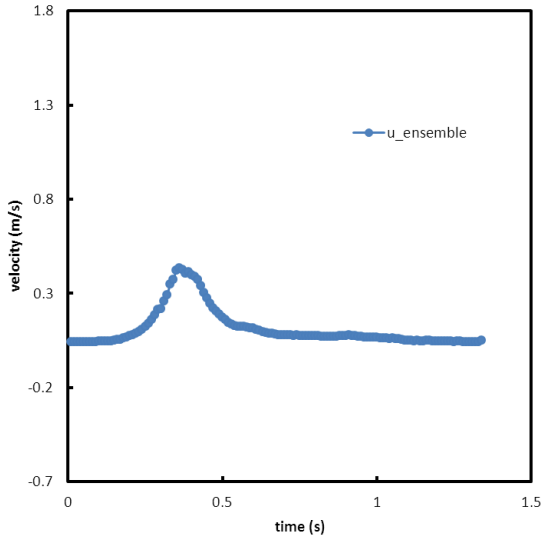

(x = 5 inch, y = 1.5 inch)

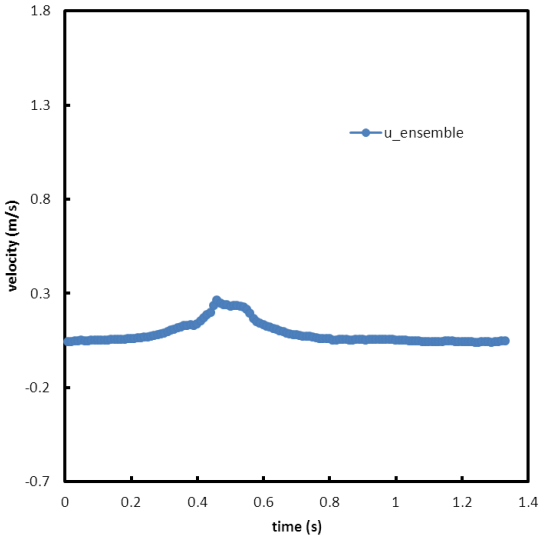

(x = 7 inch, y = 1.5 inch)

Figure 4.5.9 (d) Detail ensemble average velocities of one cycle in x-direction for different points

(x = 25 mm~178 mm (1~7 inch); y = 38 mm (1.5 inch))

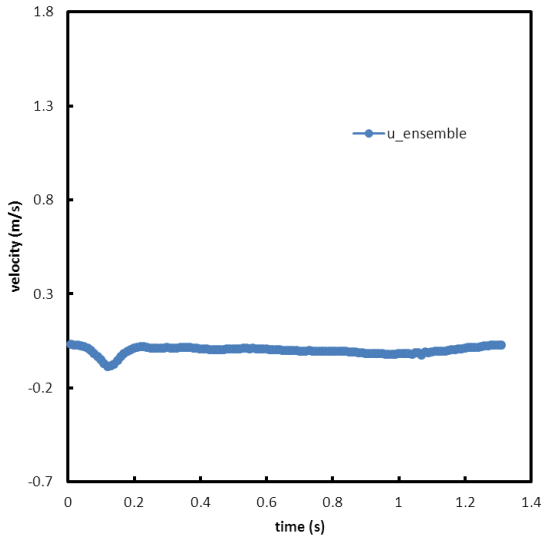

(x = 1 inch, y = 2 inch)

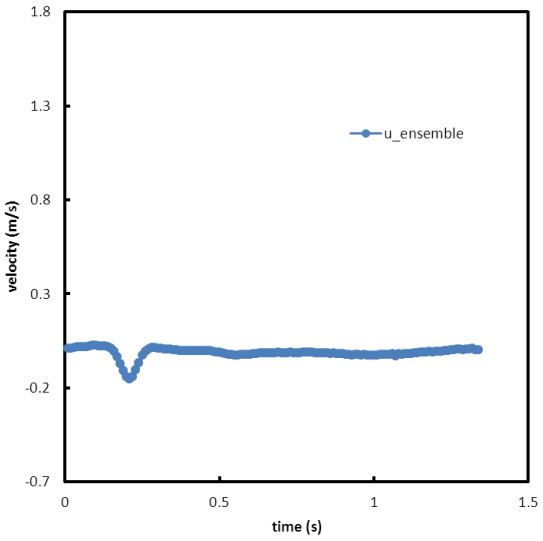

(x = 3 inch, y = 2 inch)

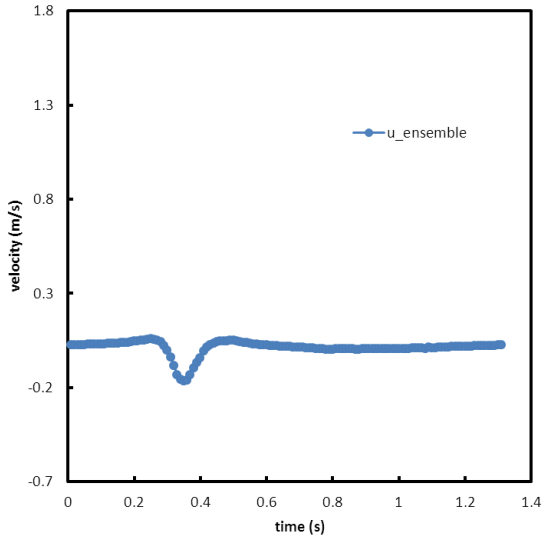

(x = 5 inch, y = 2 inch)

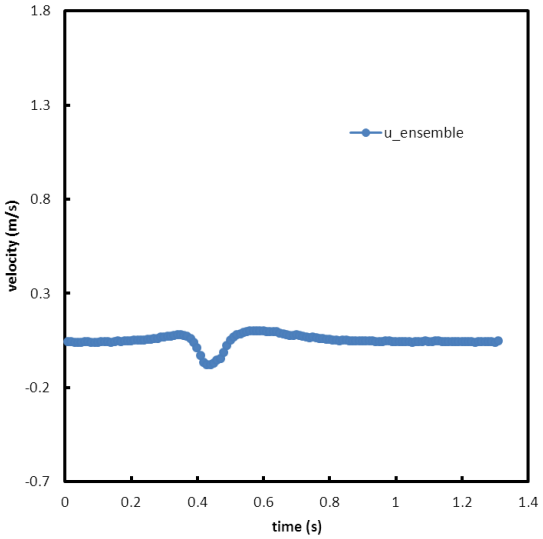

(x = 7 inch, y = 2 inch)

Figure 4.5.9 (e) Detail ensemble average velocities of one cycle in x-direction for different points

(x = 25 mm~178 mm (1~7 inch); y = 51 mm (2 inch))

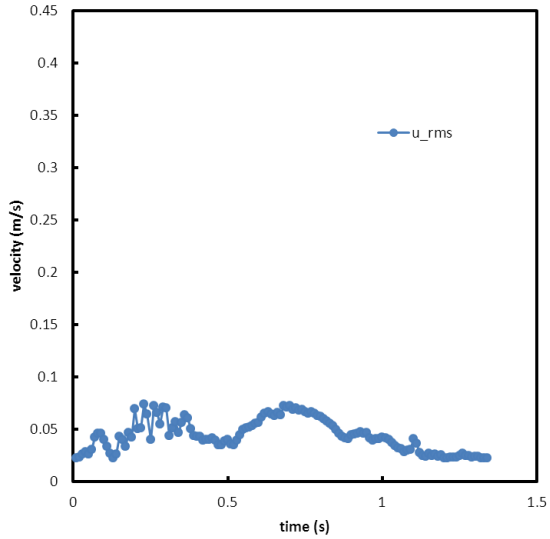

(x = 1 inch, y = 0 inch)

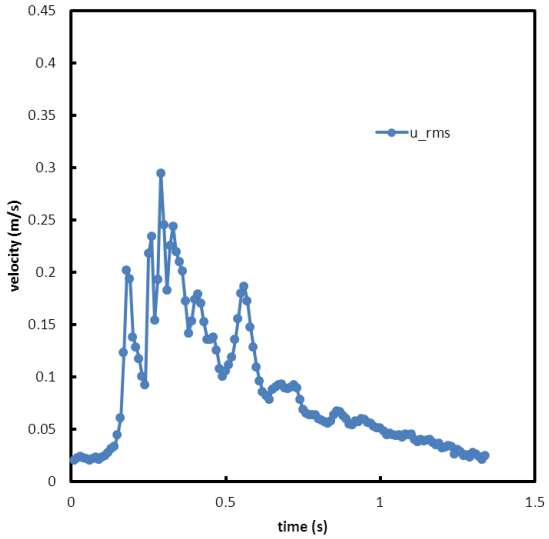

(x = 3 inch, y = 0 inch)

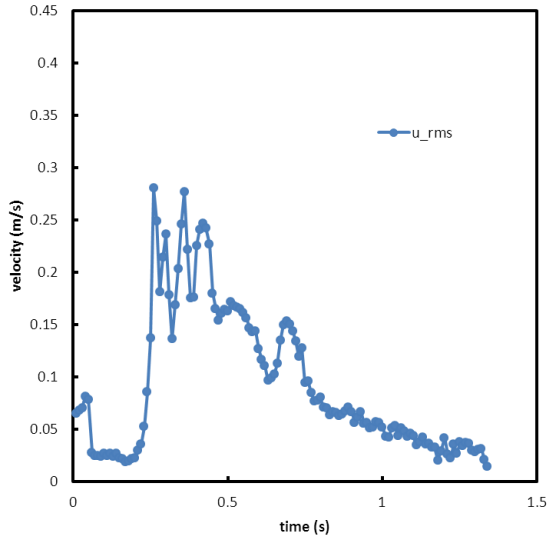

(x = 5 inch, y = 0 inch)

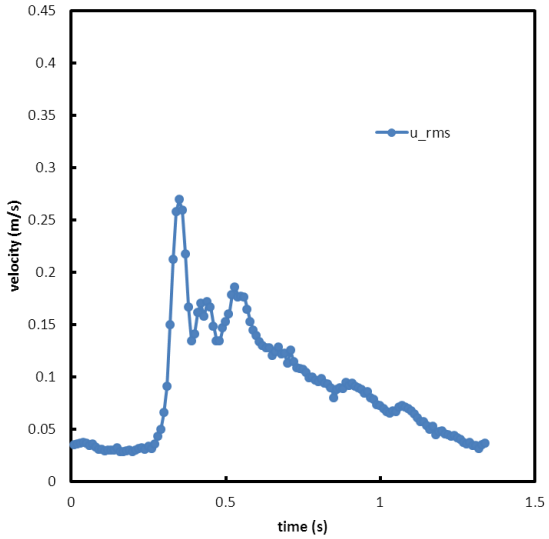

(x = 7 inch, y = 0 inch)

Figure 4.5.10 (a) Detail root mean square (RMS) velocities of one cycle in x-direction for different points

(x = 25 mm~178 mm (1~7 inch); y = 0 mm (0 inch))

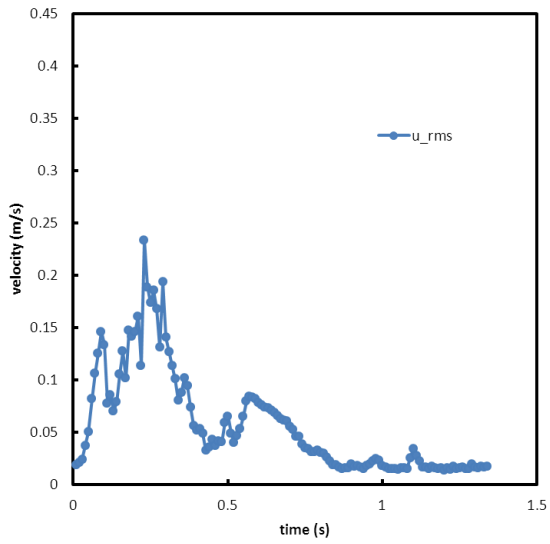

(x = 1 inch, y = 0.5 inch)

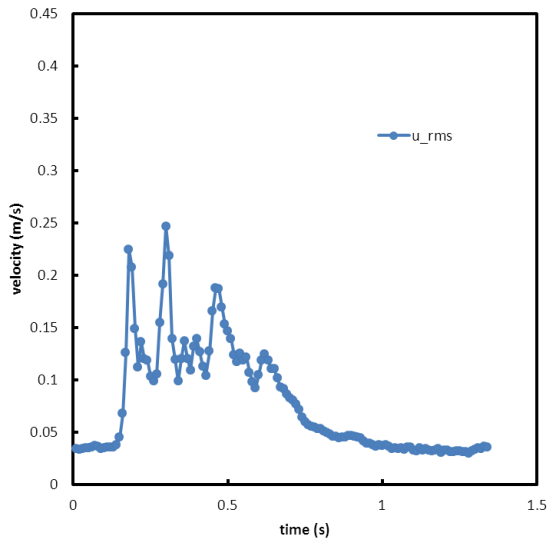

(x = 3 inch, y = 0.5 inch)

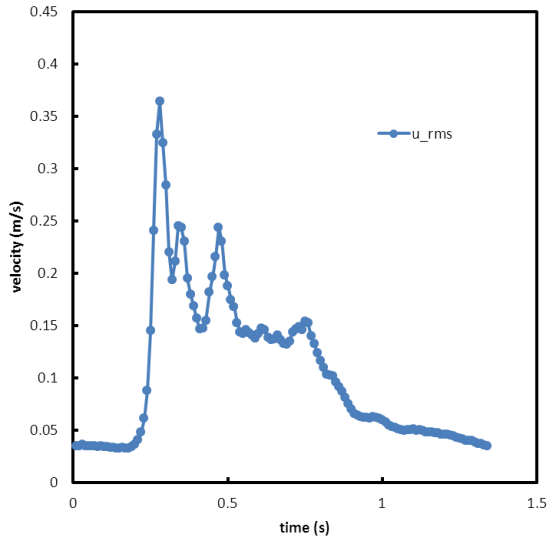

(x = 5 inch, y = 0.5 inch)

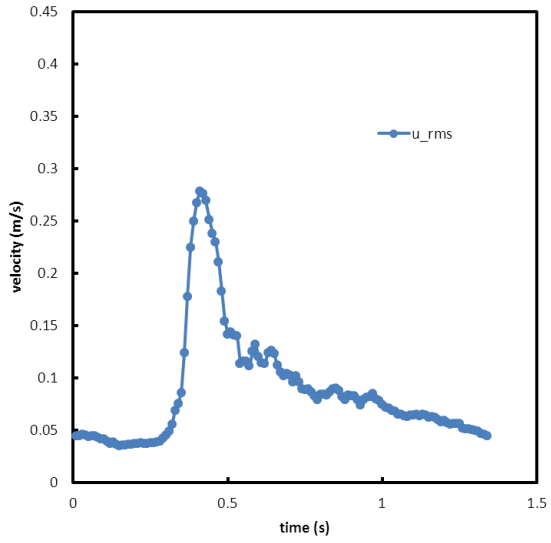

(x = 7 inch, y = 0.5 inch)

Figure 4.5.10 (b) Detail root mean square (RMS) velocities of one cycle in x-direction for different points

(x = 25 mm~178 mm (1~7 inch); y = 13 mm (0.5 inch))

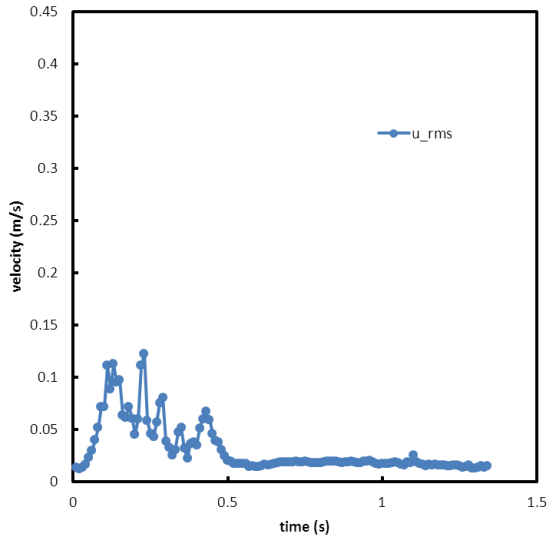

(x = 1 inch, y = 1 inch)

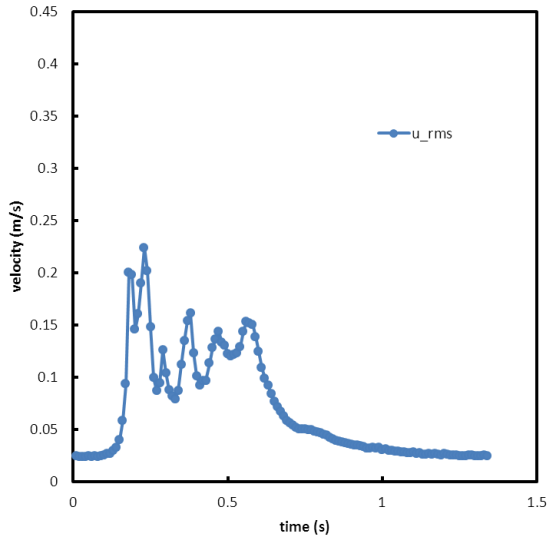

(x = 3 inch, y = 1 inch)

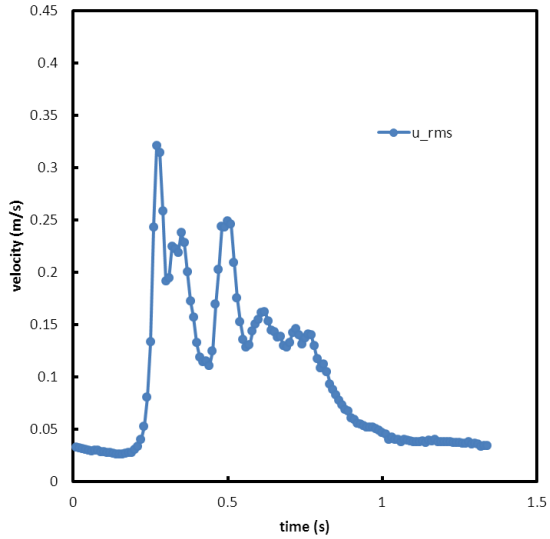

(x = 5 inch, y = 1 inch)

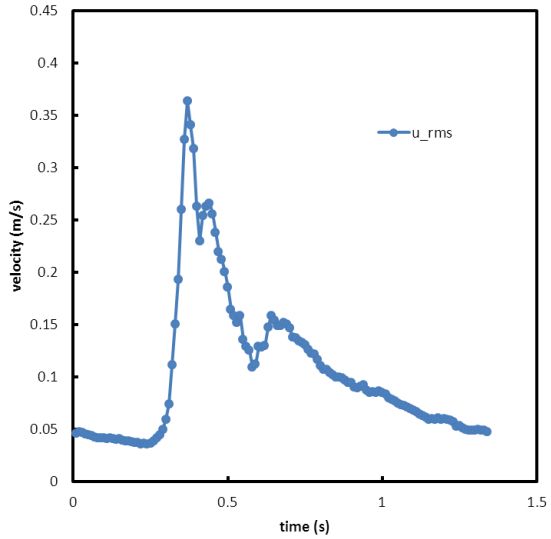

(x = 7 inch, y = 1 inch)

Figure 4.5.10 (c) Detail root mean square (RMS) velocities of one cycle in x-direction for different points

(x = 25 mm~178 mm (1~7 inch); y = 25 mm (1 inch))

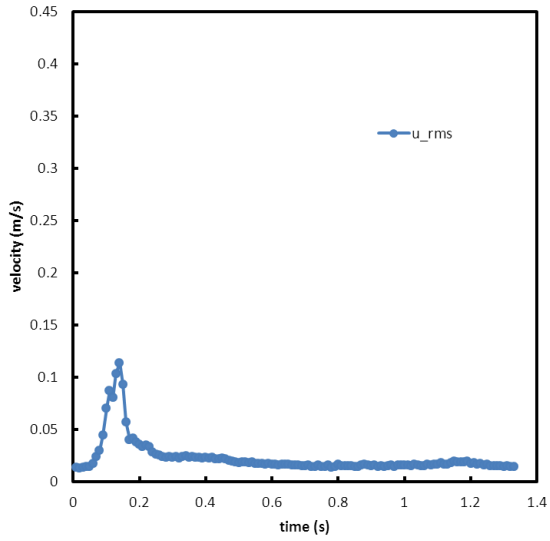

(x = 1 inch, y = 1.5 inch)

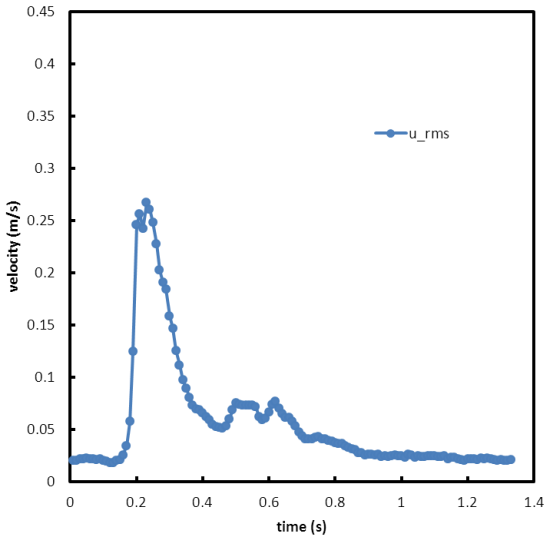

(x = 3 inch, y = 1.5 inch)

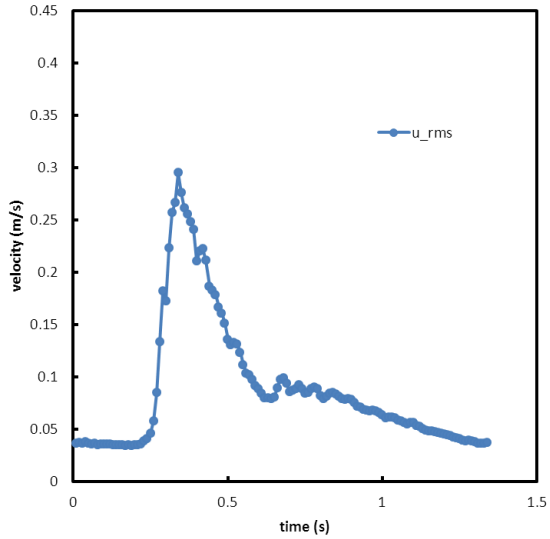

(x = 5 inch, y = 1.5 inch)

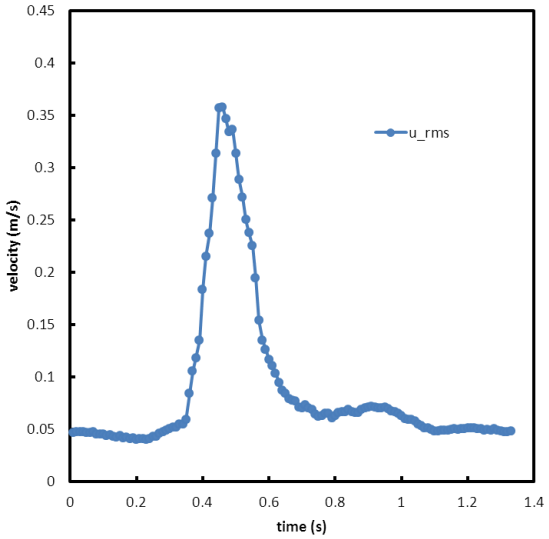

(x = 7 inch, y = 1.5 inch)

Figure 4.5.10 (d) Detail root mean square (RMS) velocities of one cycle in x-direction for different points

(x = 25 mm~178 mm (1~7 inch); y = 38 mm (1.5 inch))

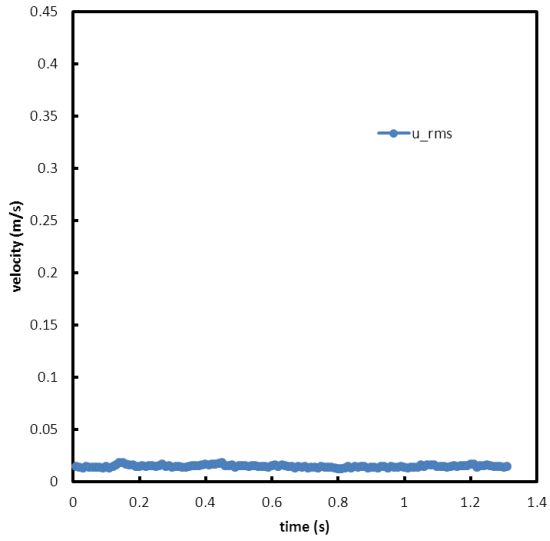

(x = 1 inch, y = 2 inch)

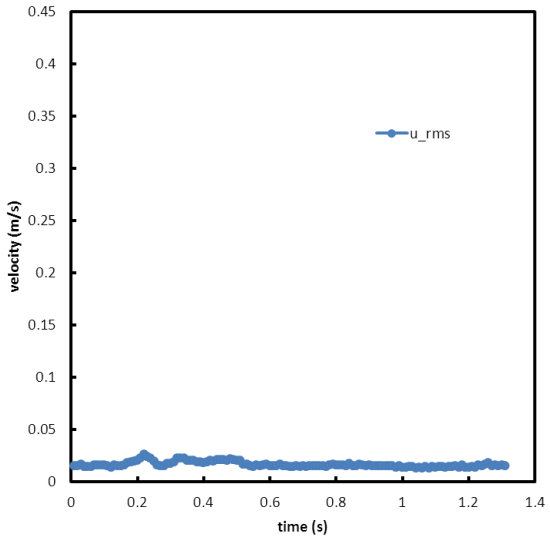

(x = 3 inch, y = 2 inch)

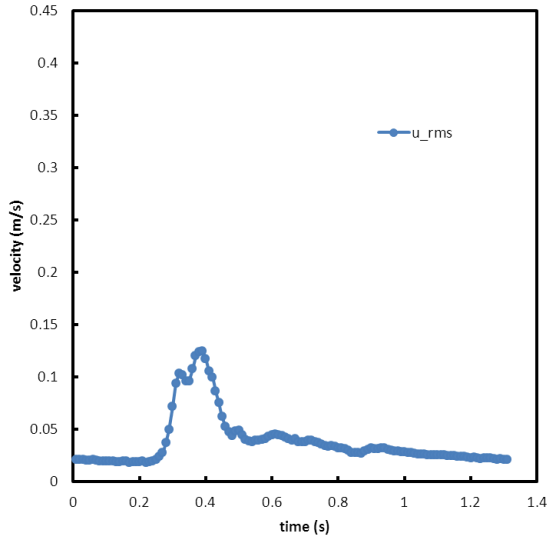

(x = 5 inch, y = 2 inch)

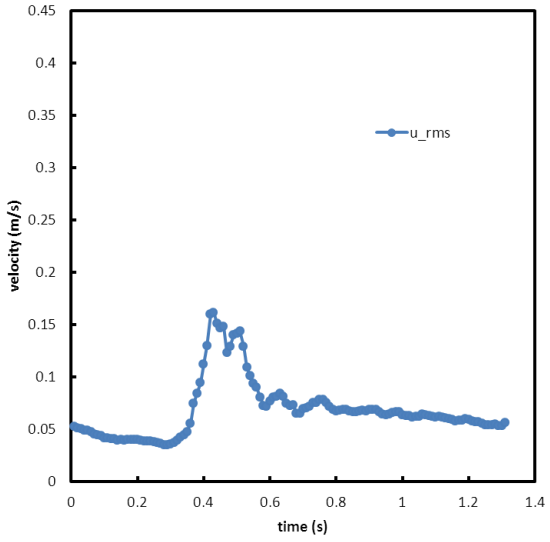

(x = 7 inch, y = 2 inch)

Figure 4.5.10 (e) Detail root mean square (RMS) velocities of one cycle in x-direction for different points

(x = 25 mm~178 mm (1~7 inch); y = 51 mm (2 inch))

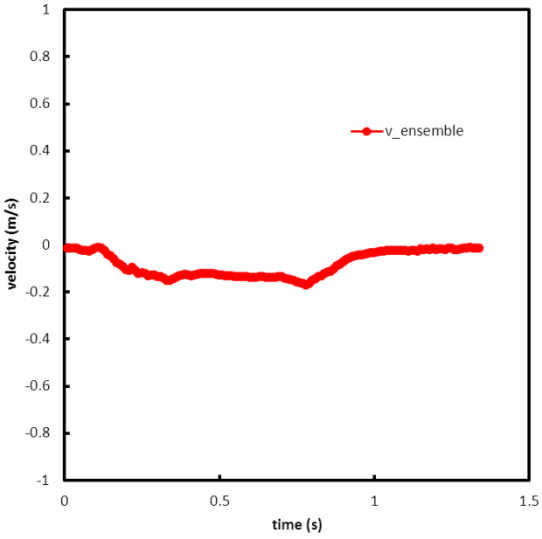

(x = 1 inch, y = 0 inch)

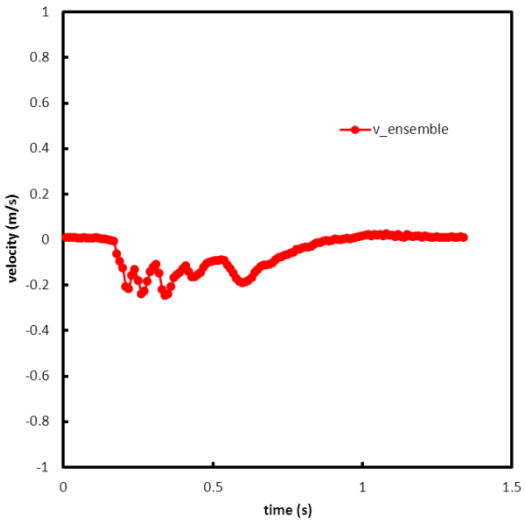

(x = 3 inch, y = 0 inch)

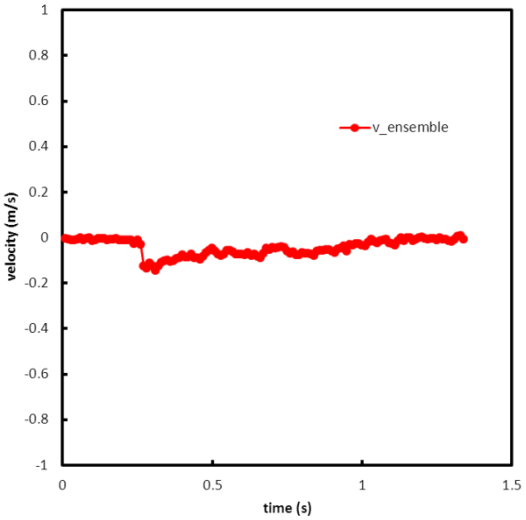

(x = 5 inch, y = 0 inch)

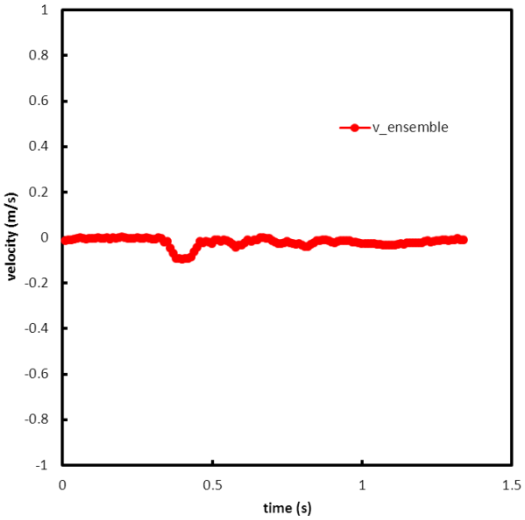

(x = 7 inch, y = 0 inch)

Figure 4.5.11 (a) Detail ensemble average velocities of one cycle in y-direction for different points

(x = 25 mm~178 mm (1~7 inch); y = 0 mm (0 inch))

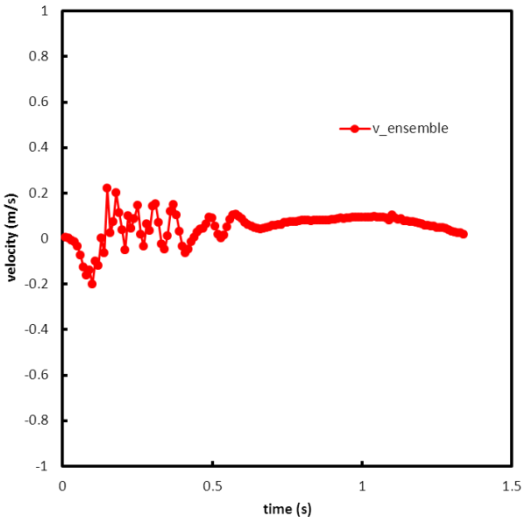

(x = 1 inch, y = 0.5 inch)

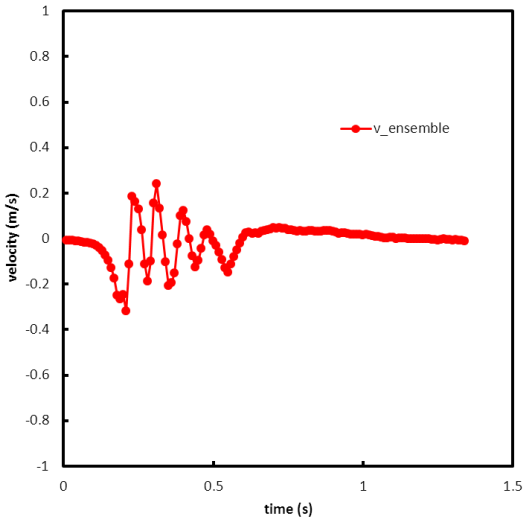

(x = 3 inch, y = 0.5 inch)

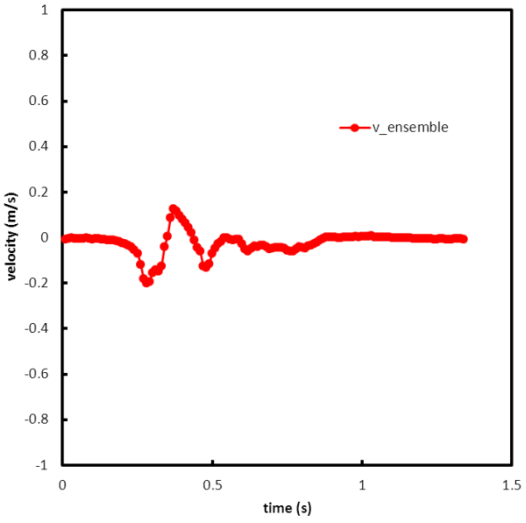

(x = 5 inch, y = 0.5 inch)

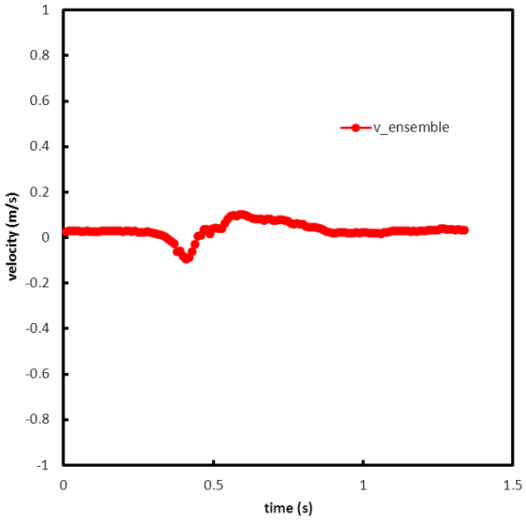

(x = 7 inch, y = 0.5 inch)

Figure 4.5.11 (b) Detail ensemble average velocities of one cycle in y-direction for different points

(x = 25 mm~178 mm (1~7 inch); y = 13 mm (0.5 inch))

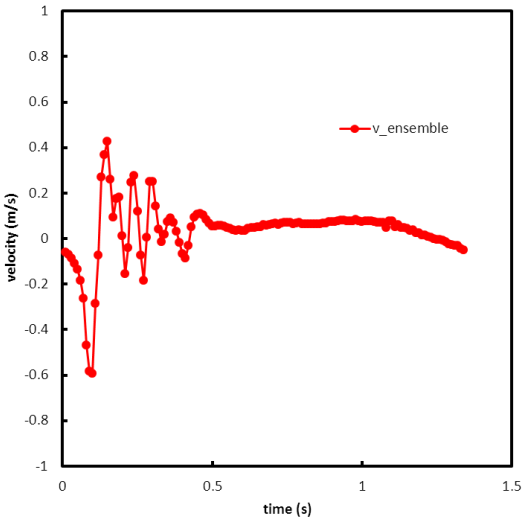

(x = 1 inch, y = 1 inch)

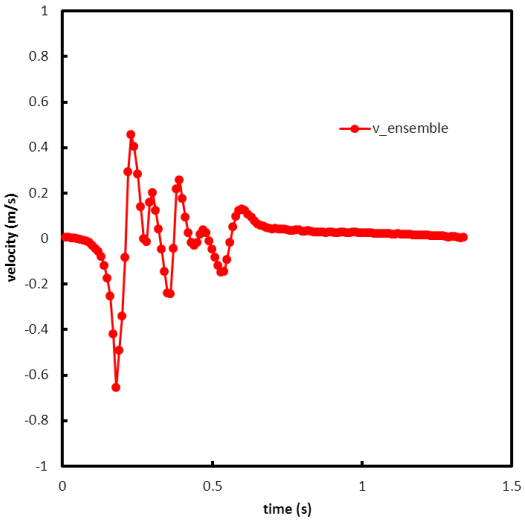

(x = 3 inch, y = 1 inch)

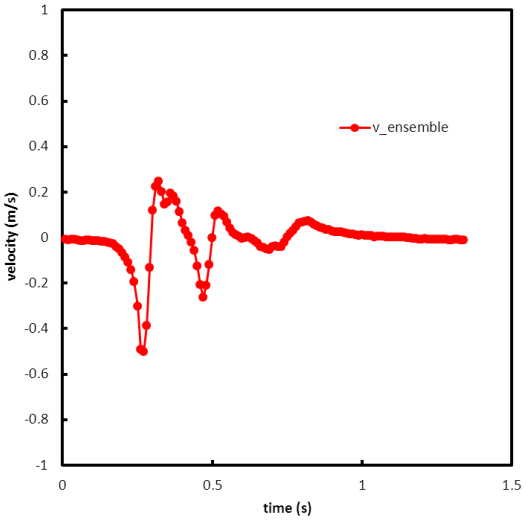

(x = 5 inch, y = 1 inch)

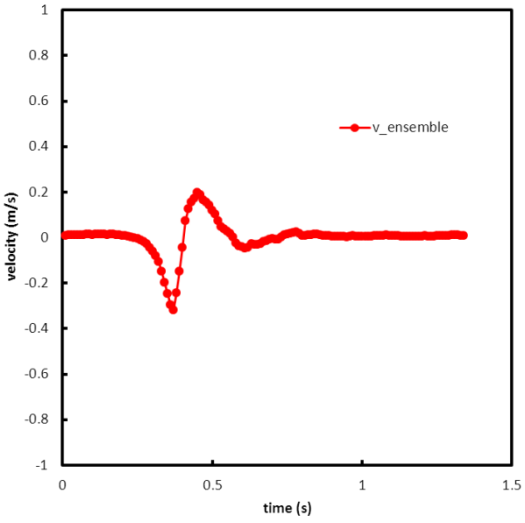

(x = 7 inch, y = 1 inch)

Figure 4.5.11 (c) Detail ensemble average velocities of one cycle in y-direction for different points

(x = 25 mm~178 mm (1~7 inch); y = 25 mm (1 inch))

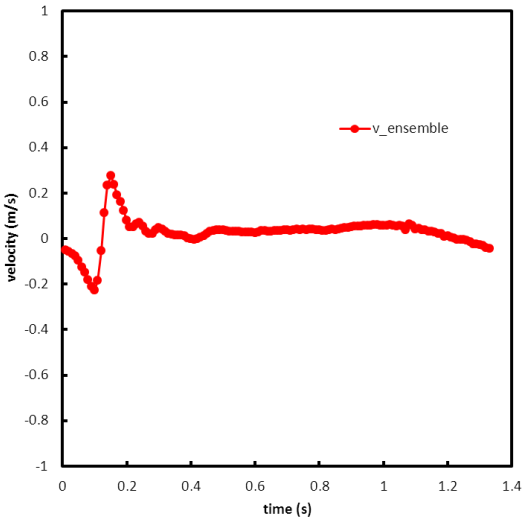

(x = 1 inch, y = 1.5 inch)

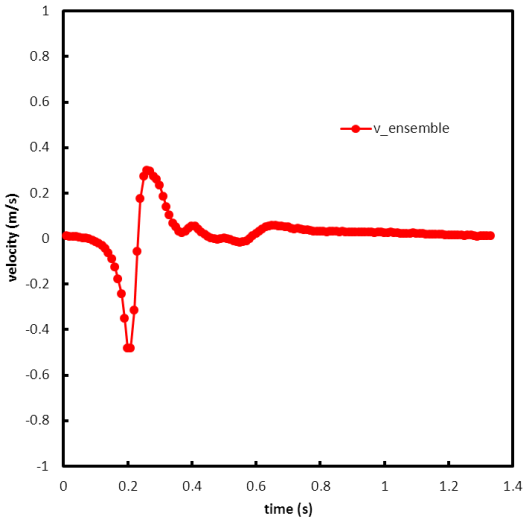

(x = 3 inch, y = 1.5 inch)

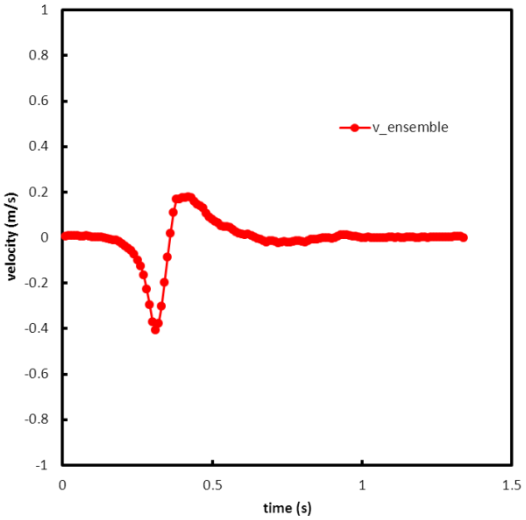

(x = 5 inch, y = 1.5 inch)

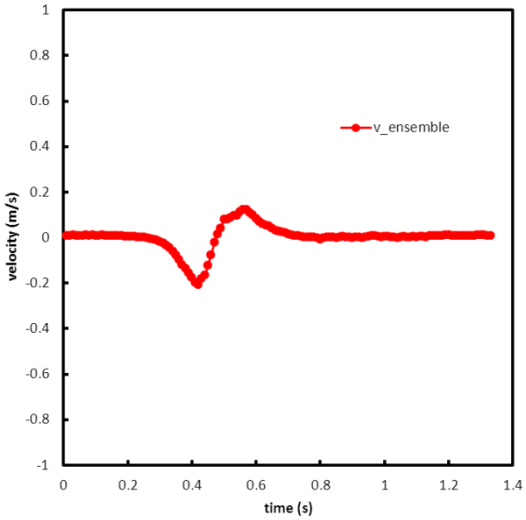

(x = 7 inch, y = 1.5 inch)

Figure 4.5.11 (d) Detail ensemble average velocities of one cycle in y-direction for different points

(x = 25 mm~178 mm (1~7 inch); y = 38 mm (1.5 inch))

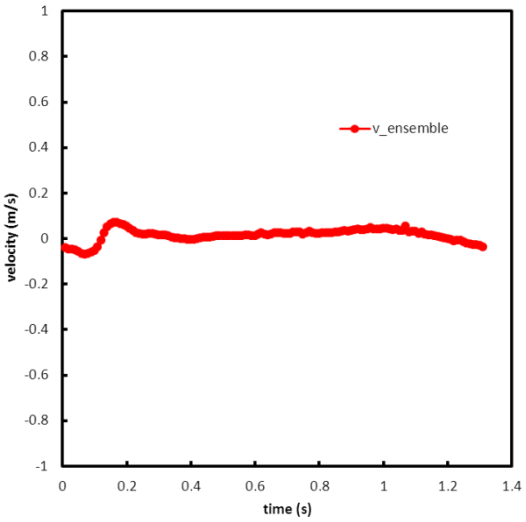

(x = 1 inch, y = 2 inch)

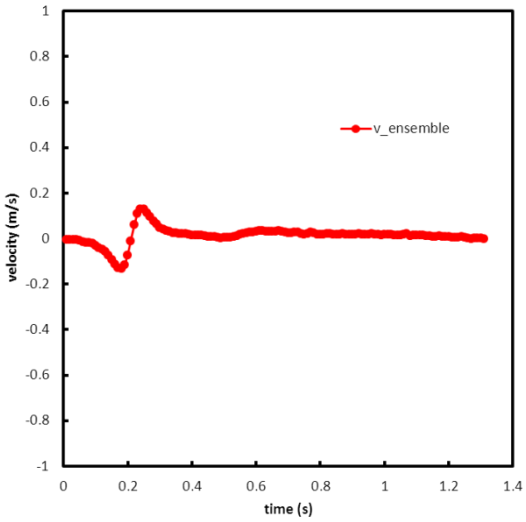

(x = 3 inch, y = 2 inch)

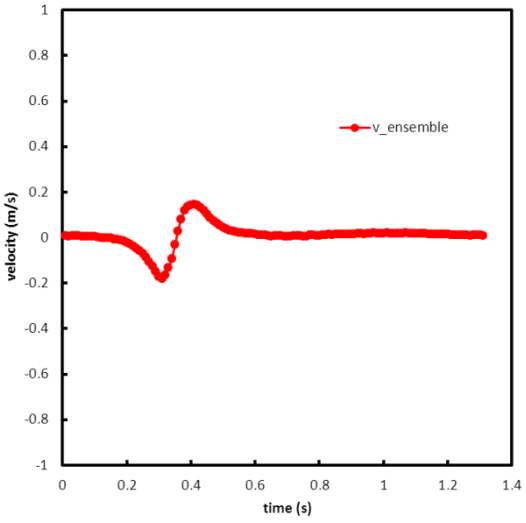

(x = 5 inch, y = 2 inch)

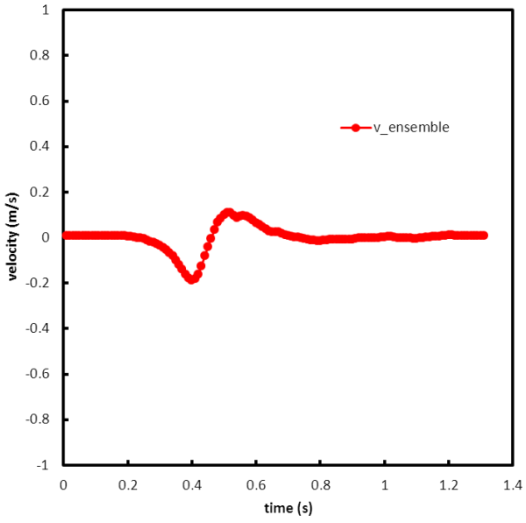

(x = 7 inch, y = 2 inch)

Figure 4.5.11 (e) Detail ensemble average velocities of one cycle in y-direction for different points

(x = 25 mm~178 mm (1~7 inch); y = 51 mm (2 inch))

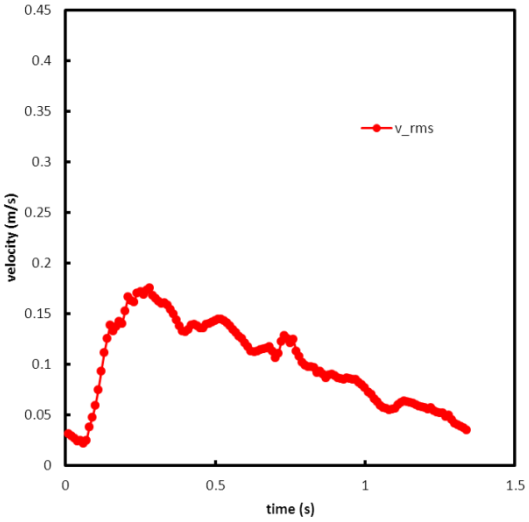

(x = 1 inch, y = 0 inch)

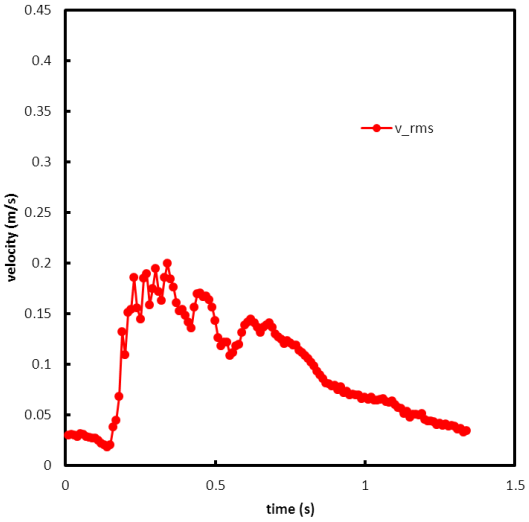

(x = 3 inch, y = 0 inch)

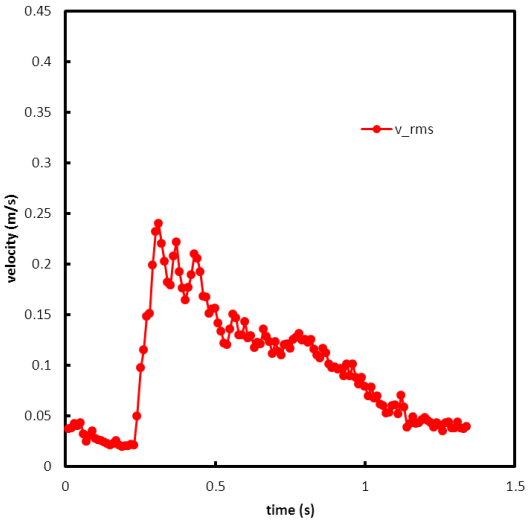

(x = 5 inch, y = 0 inch)

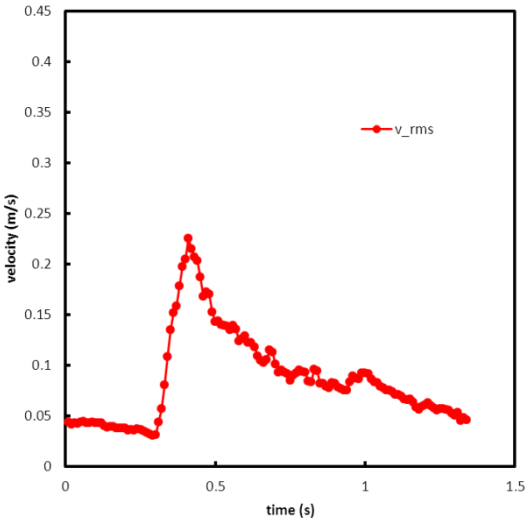

(x = 7 inch, y = 0 inch)

Figure 4.5.12 (a) Detail root mean square (RMS) velocities of one cycle in y-direction for different points

(x = 25 mm~178 mm (1~7 inch); y = 0 mm (0 inch))

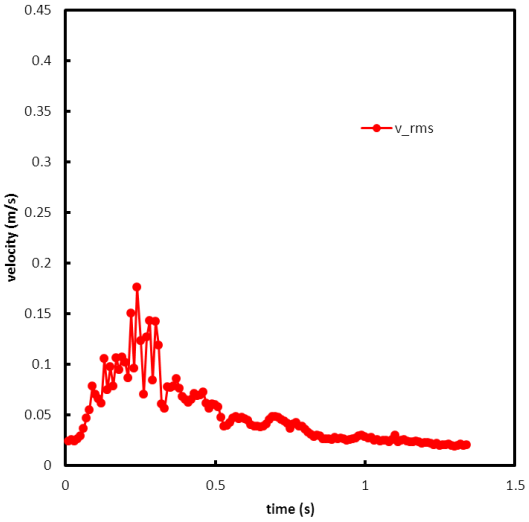

(x = 1 inch, y = 0.5 inch)

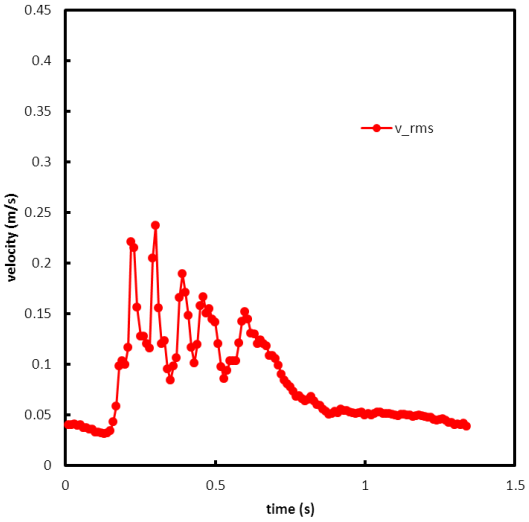

(x = 3 inch, y = 0.5 inch)

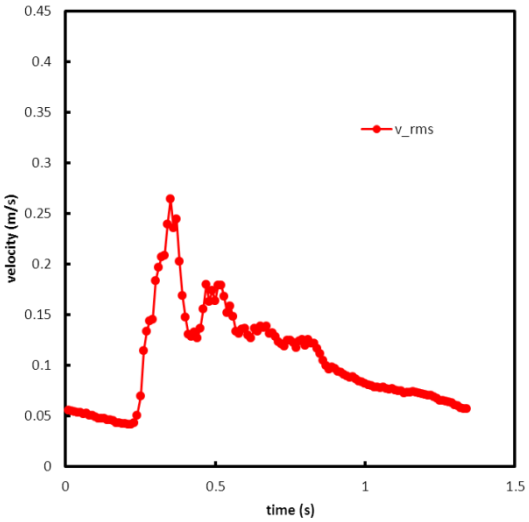

(x = 5 inch, y = 0.5 inch)

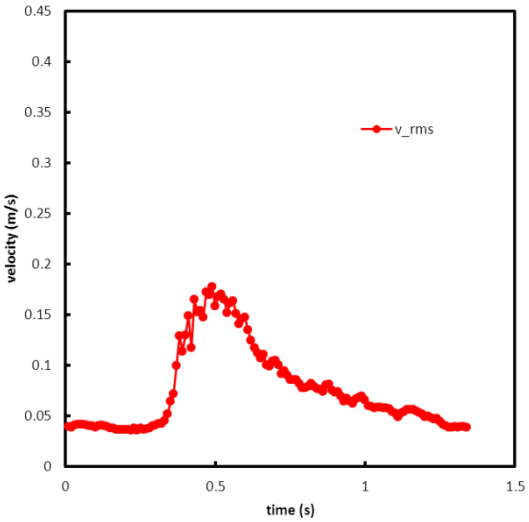

(x = 7 inch, y = 0.5 inch)

Figure 4.5.12 (b) Detail root mean square (RMS) velocities of one cycle in y-direction for different points

(x = 25 mm~178 mm (1~7 inch); y = 13 mm (0.5 inch))

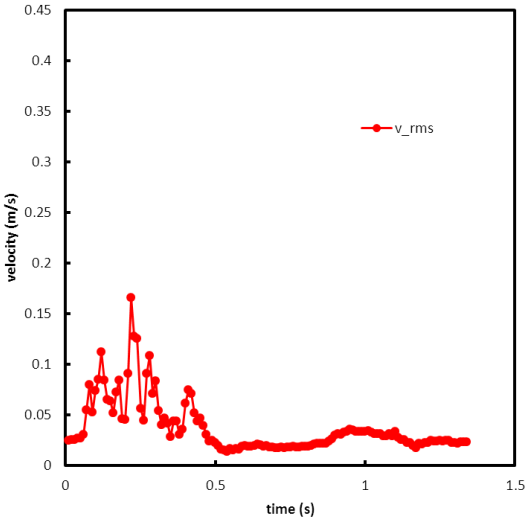

(x = 1 inch, y = 1 inch)

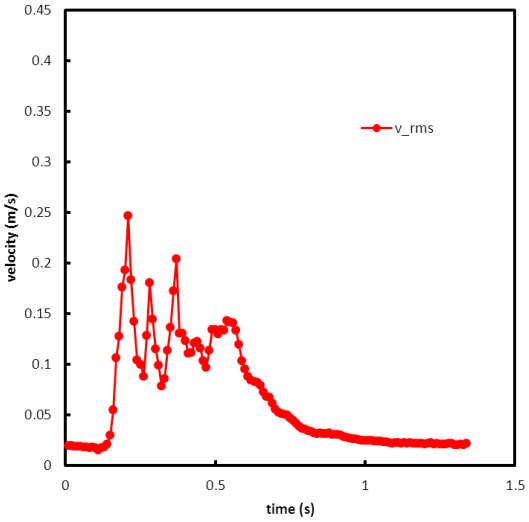

(x = 3 inch, y = 1 inch)

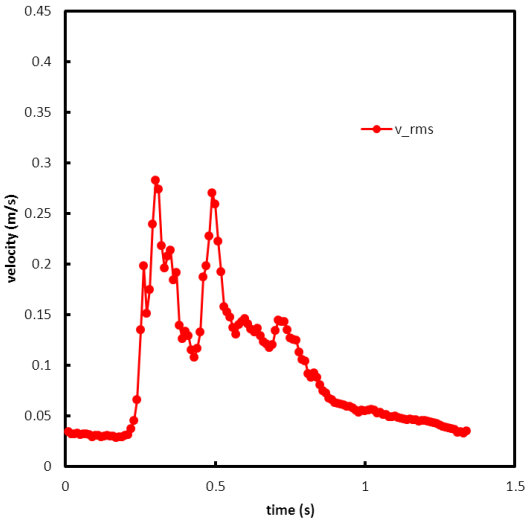

(x = 5 inch, y = 1 inch)

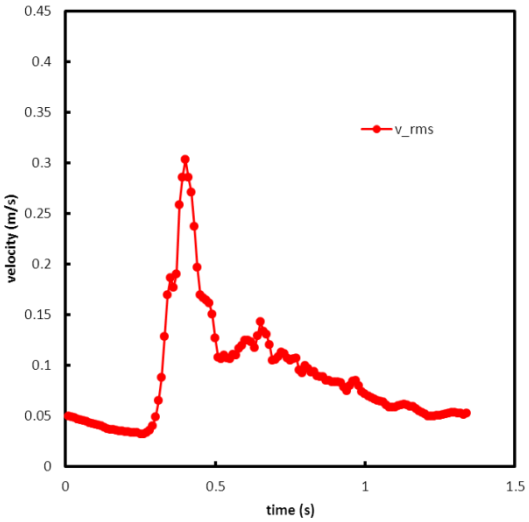

(x = 7 inch, y = 1 inch)

Figure 4.5.12 (c) Detail root mean square (RMS) velocities of one cycle in y-direction for different points

(x = 25 mm~178 mm (1~7 inch); y = 25 mm (1 inch))

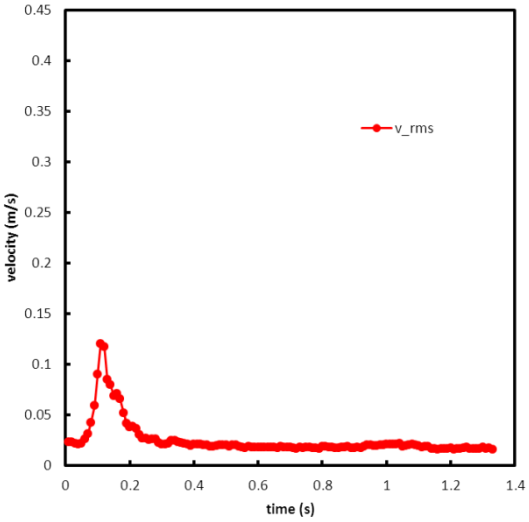

(x = 1 inch, y = 1.5 inch)

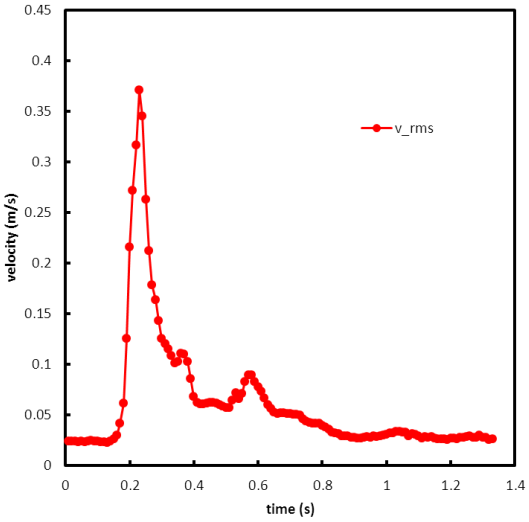

(x = 3 inch, y = 1.5 inch)

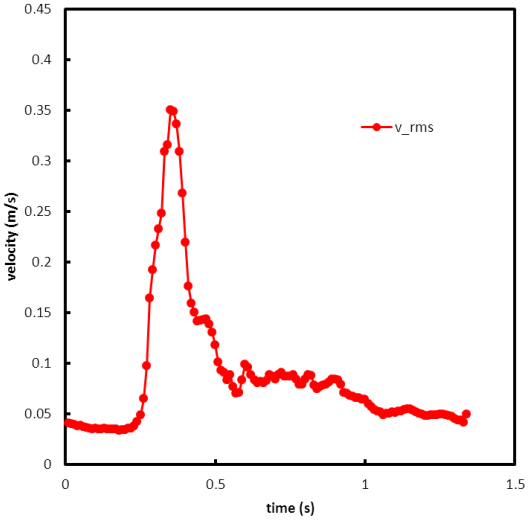

(x = 5 inch, y = 1.5 inch)

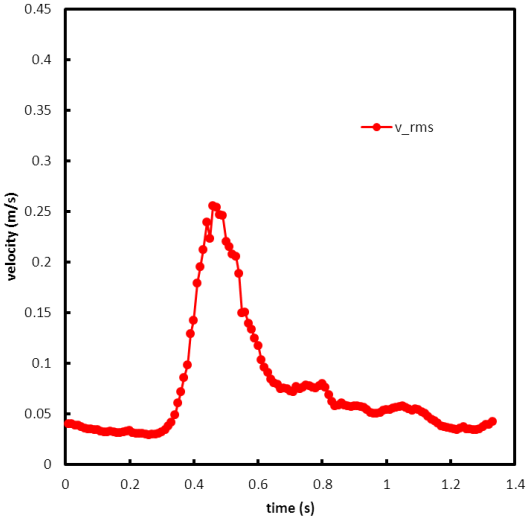

(x = 7 inch, y = 1.5 inch)

Figure 4.5.12 (d) Detail root mean square (RMS) velocities of one cycle in y-direction for different points

(x = 25 mm~178 mm (1~7 inch); y = 38 mm (1.5 inch))

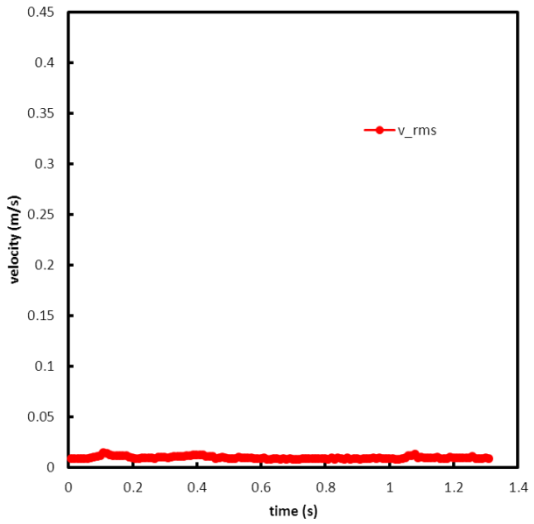

(x = 1 inch, y = 2 inch)

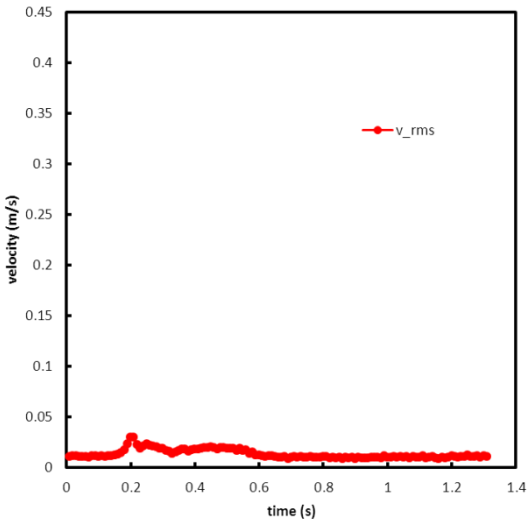

(x = 3 inch, y = 2 inch)

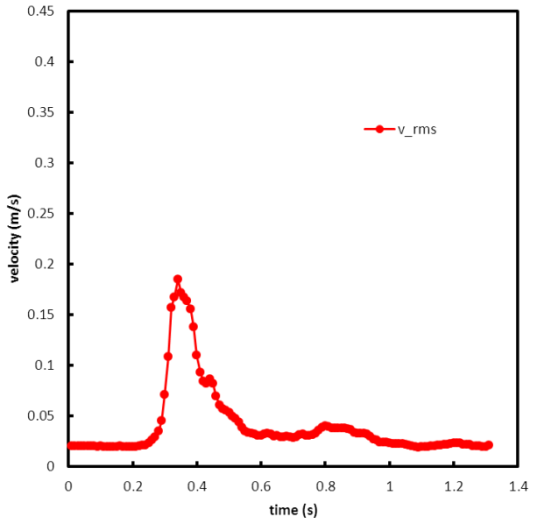

(x = 5 inch, y = 2 inch)

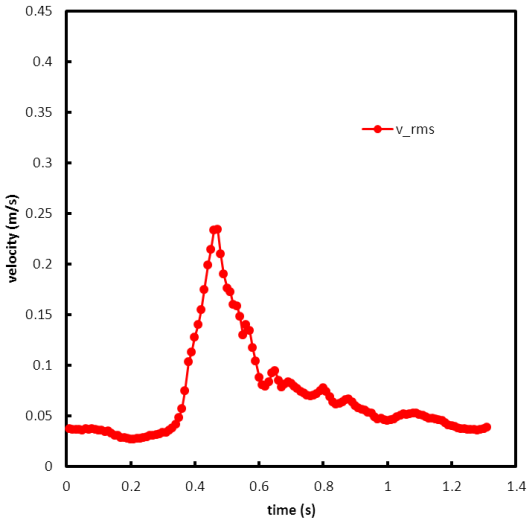

(x = 7 inch, y = 2 inch)

Figure 4.5.12 (e) Detail root mean square (RMS) velocities of one cycle in y-direction for different points

(x = 25 mm~178 mm (1~7 inch); y = 51 mm (2 inch))

Chapter 5 Numerical Simulation of Synthetic Jet Impingement Cooling

5.1 Numerical Model

In this section, a numerical study of synthetic jet impingement cooling is introduced. The numerical model is validated by comparing computed results to the experimental data. It is then used to predict the behavior of the synthetic jet under different conditions. Figure 5.1 shows the three-dimensional synthetic jet model. The moving diaphragm of the jet is modeled as a moving wall by using a layering dynamic mesh which can be achieved with a user defined function in the commercial computational fluid dynamics (CFD) software (ANSYS FLUENT). All of the convective walls of the fin (the impingement surface) are defined as constant temperature boundaries held 10°C higher than the ambient temperature. The boundaries of the enclosure are set to be constant pressure outlet boundaries, which can allow fresh air to come in at constant ambient temperature. In the computation, three-dimensional, incompressible, time-dependent Reynolds-Averaged Navier-Stokes equations (RANS) are solved with the shear-stress-transport (SST), k-ω turbulence kinetic energy term, and a specific dissipation rate term, which is widely used to solve the shear flow problem. This model has been validated by comparing with the experimental data. The first-order implicit Euler discretization scheme is used for the time model. The second-order upwind scheme is employed for other terms in the momentum equation, energy equation, and turbulence terms. The Semi-Implicit Method for Pressure Linked Equations (SIMPLE) algorithm is

employed for pressure-velocity coupling. At each time step, the internal iterations continue until the residuals have been reduced to 10^{-6}.

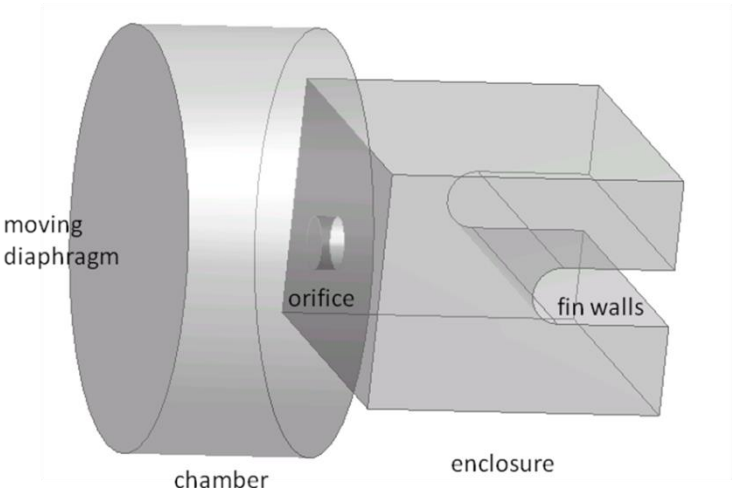

Figure 5.1 The boundaries and computational domain of the numerical simulation

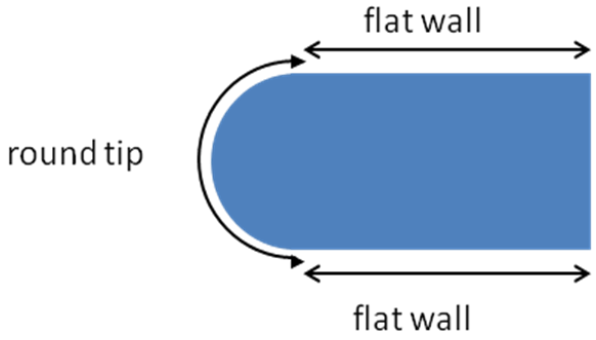

Figure 5.2 Different convective surfaces in the computation

5.2 Grid Independence Study

One specific case is run under different mesh sizes to validate grid independence. The jet is operating at 1420 Hz with a spatial-average peak velocity of 52 m/s. The diameter of the orifice is 1 mm and the distance between the orifice plate and tip of the

channel wall (fin) is 3 mm (z/d = 3). The average heat transfer coefficients of the round tip, flat walls, and all (round tip plus flat wall) convective surfaces for a reference case are compared with a case having an increased number of cells in Table 5.1. The results show good convergence. The maximum difference is less than 5%.

Table 5.1 Heat transfer coefficients with different grid sizes

Number of cells	h_{avg} of round tip (W/m^2K)	h_{avg} of flat walls (W/m^2K)	h_{avg} of all surfaces (W/m^2K)
0.2 million	667	261	376
0.5 million	667	267	379
0.9 million	663	259	373
1.5 million	663	255	371
2.5 million	667	254	369

5.3 Comparison between Computation and Experiment

The average heat transfer coefficients over all convective surfaces measured during the experiment are compared to those obtained from the numerical simulation (Fig. 5.3) for cases of different frequencies. The geometry and the spatially-averaged velocity are the same for the experiments and computations. The results show good agreement, with a maximum difference of less than 10%. The computational results are a little higher than the experimental results in the low-frequency region, while lower in the high-frequency region.

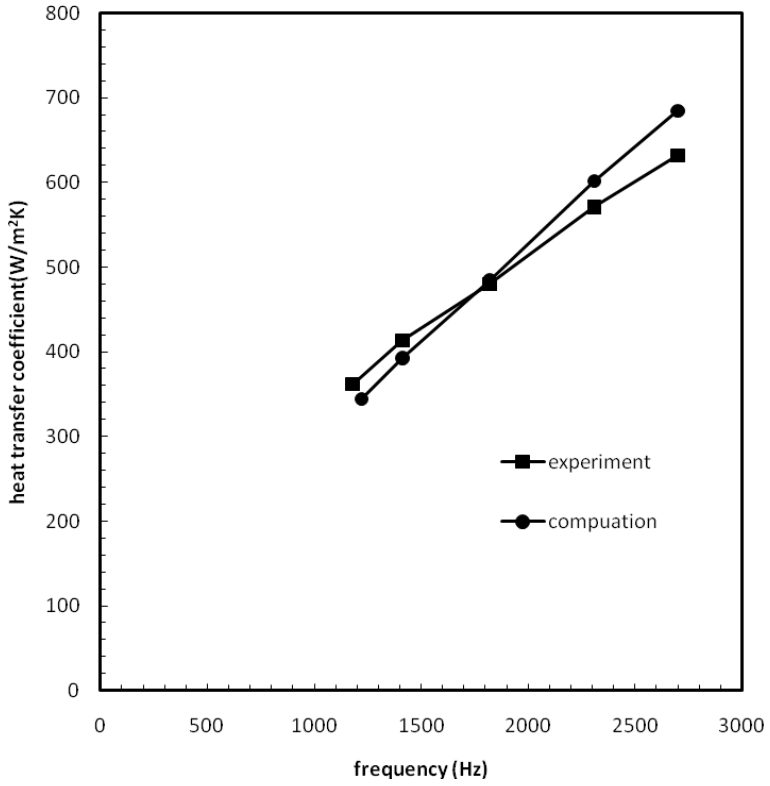

Figure 5.3 Comparison of average heat transfer coefficients between experiment and numerical simulations

5.4 Parametric Study of Synthetic Jet Impingement Cooling

Since the numerical model described above can provide good predictions of the behavior of synthetic jet flow and heat transfer, a parametric study of heat transfer performance is developed using a circular orifice synthetic jet (d = 1 mm). The effects of amplitude and frequency of diaphragm movement are investigated with a constant z/d of 3.0. The effects of the distance between orifice plate and the fin tip are also investigated for fixed amplitude or frequency.

5.4.1 Different Amplitudes at the Same Frequency

The amplitude of diaphragm movement is changed while frequency is held constant.

The change of amplitude is reflected by the variation of spatially-averaged peak velocity of flow from the orifice. The peak jet velocity grows linearly with amplitude. Figure 5.4 shows that heat transfer coefficients of different convective surfaces are characterized by a linear increase with jet peak velocity. This trend exists for different frequency levels, which indicates that the amplitude of diaphragm movement is an important parameter to heat transfer performance. The case with a frequency of 4880 Hz and a peak jet velocity of 23 m/s differs from the others. The heat transfer coefficient is unusually low. A possible reason is that part of the expelled flow is drawn back into the cavity because of the high frequency and low ejection velocity and is not able to impinge on the fin surface in a normal manner. For this case, a particle transit distance is about one nozzle diameter.

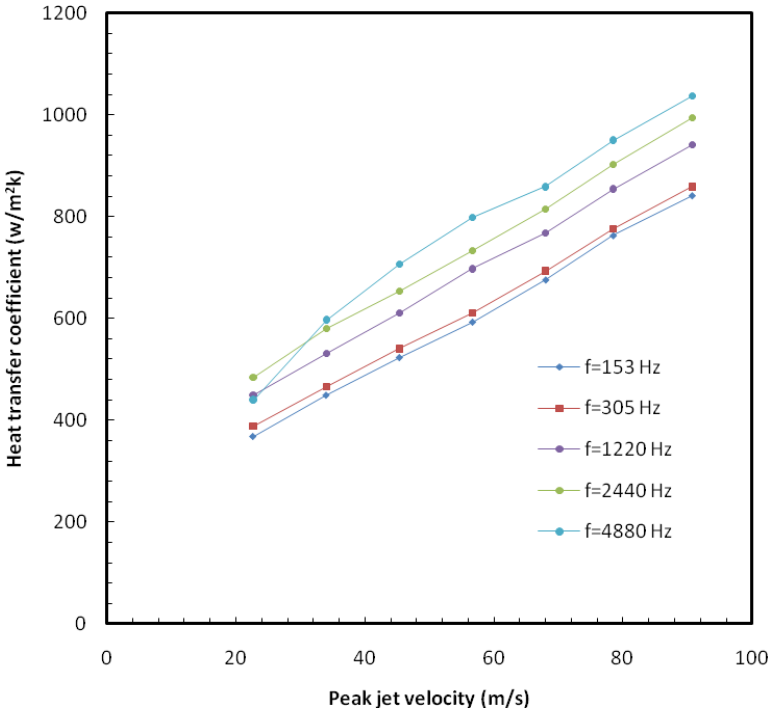

Figure 5.4a Average heat transfer coefficient over round tip for cases with different amplitudes – round tip

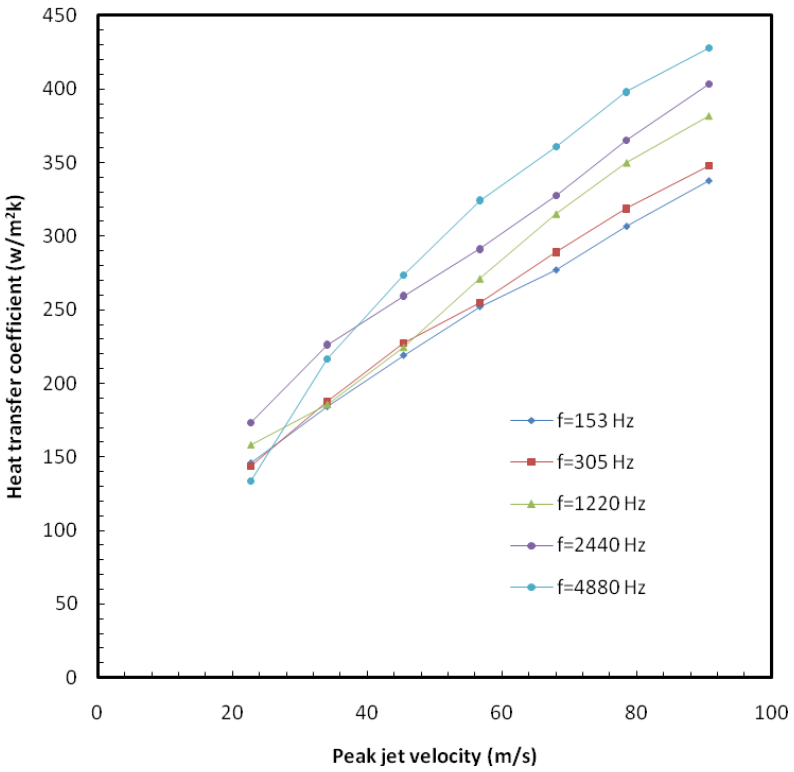

Figure 5.4b Average heat transfer coefficient over flat walls for cases with different amplitudes – flat wall

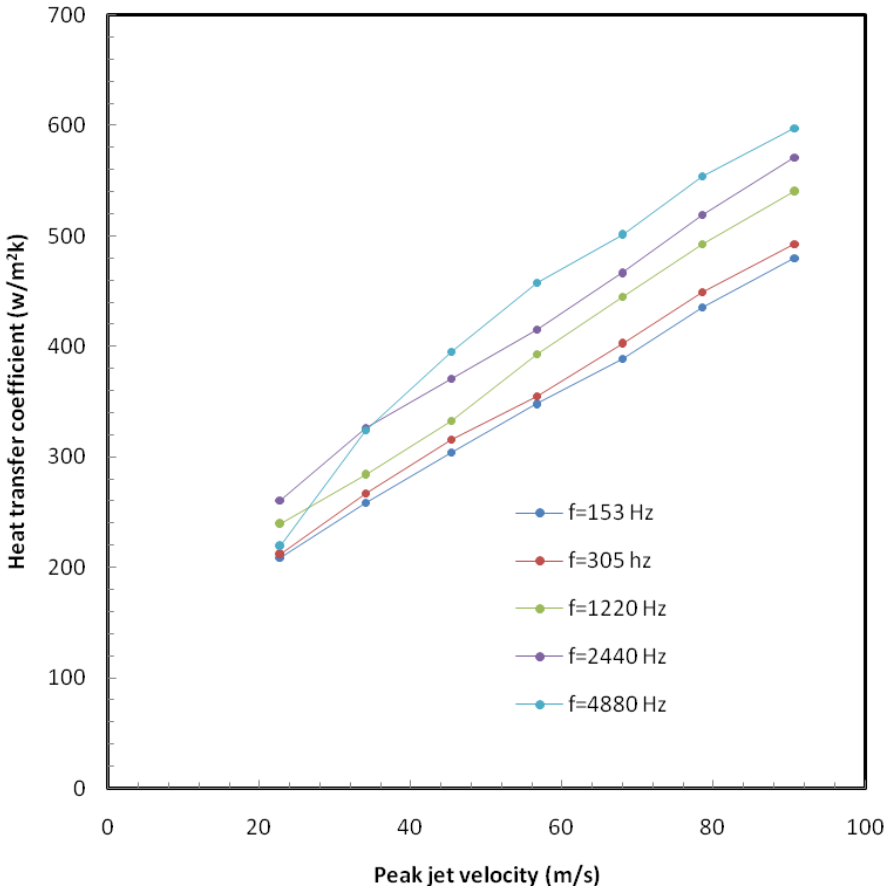

Figure 5.4c Average heat transfer coefficient over all convective surfaces for cases with different amplitudes – round tip and flat wall

5.4.2 Different Frequencies at the Same Flow Rate

In this section, the product of amplitude and frequency is fixed for each curve, which produces a constant jet peak velocity. Under this condition the changing frequency effect is studied. The heat transfer coefficients increase with an increase of frequency. However the increased rate is larger in the high-frequency range and smaller in the low-frequency range. Increasing frequency from 153 Hz to 4880 Hz can only generate a heat transfer coefficient increases of less than 30%. Compared to the effect of amplitude on heat transfer performance, the frequency is found to be less important.

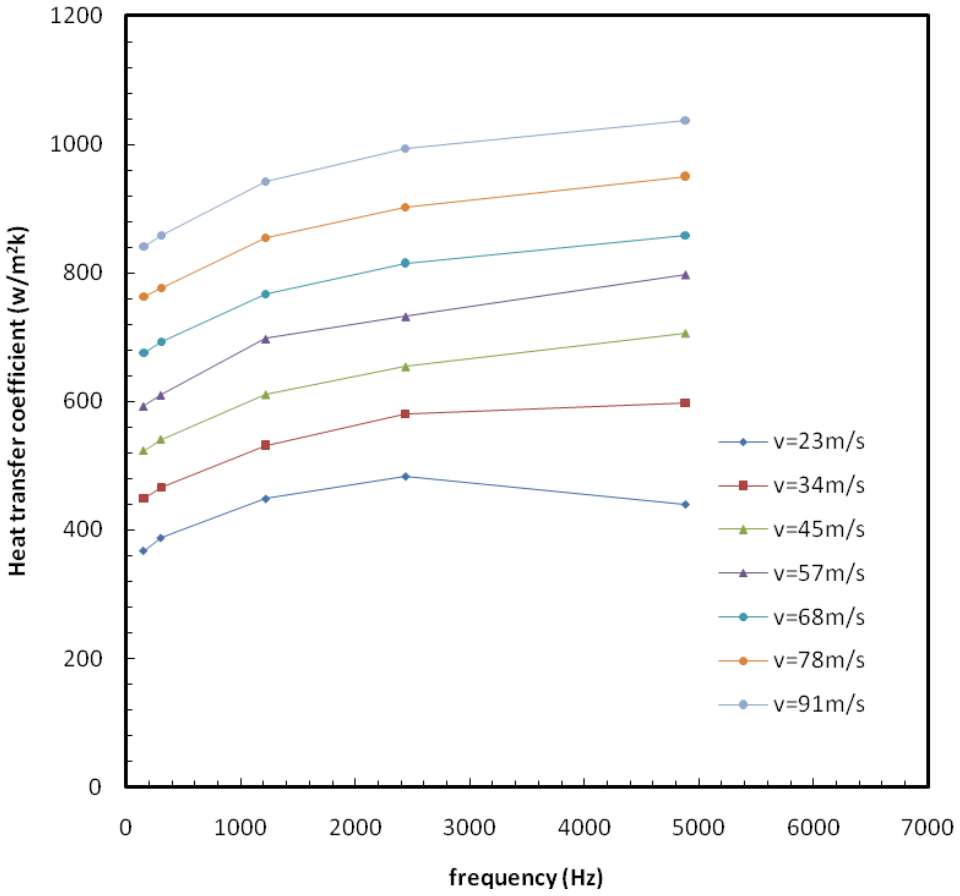

Figure 5.5a Average heat transfer coefficient over the round tip for cases of different frequencies

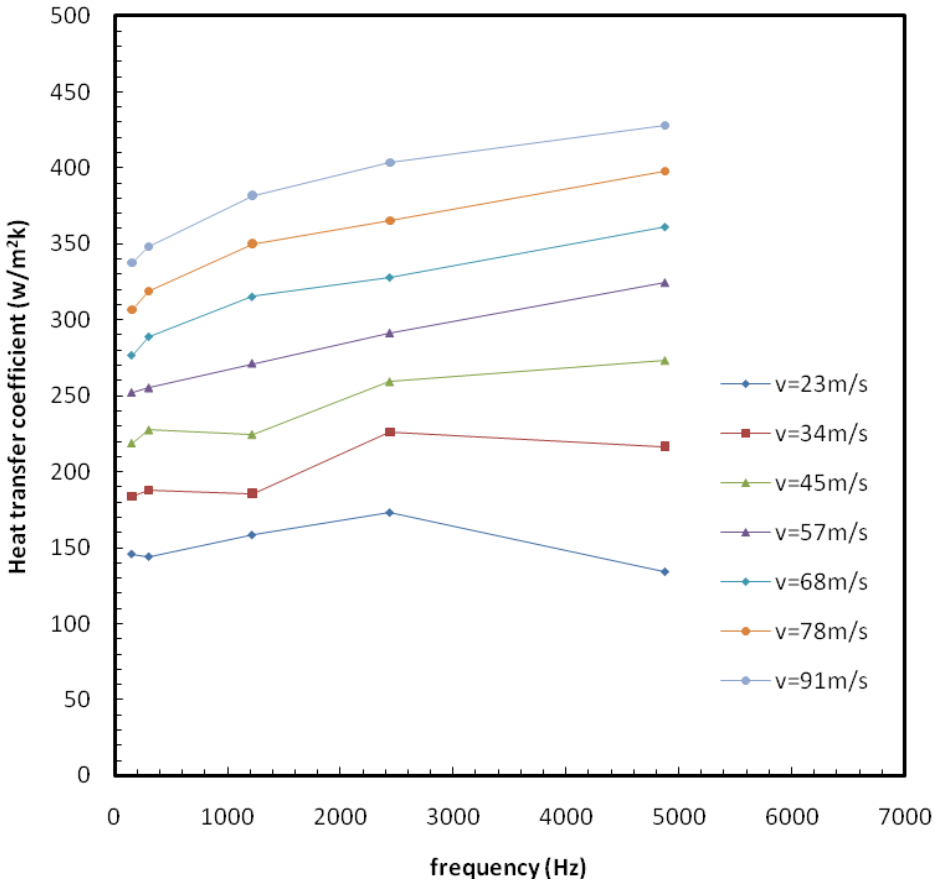

Figure 5.5b Average heat transfer coefficient over the flat walls for cases of different frequencies

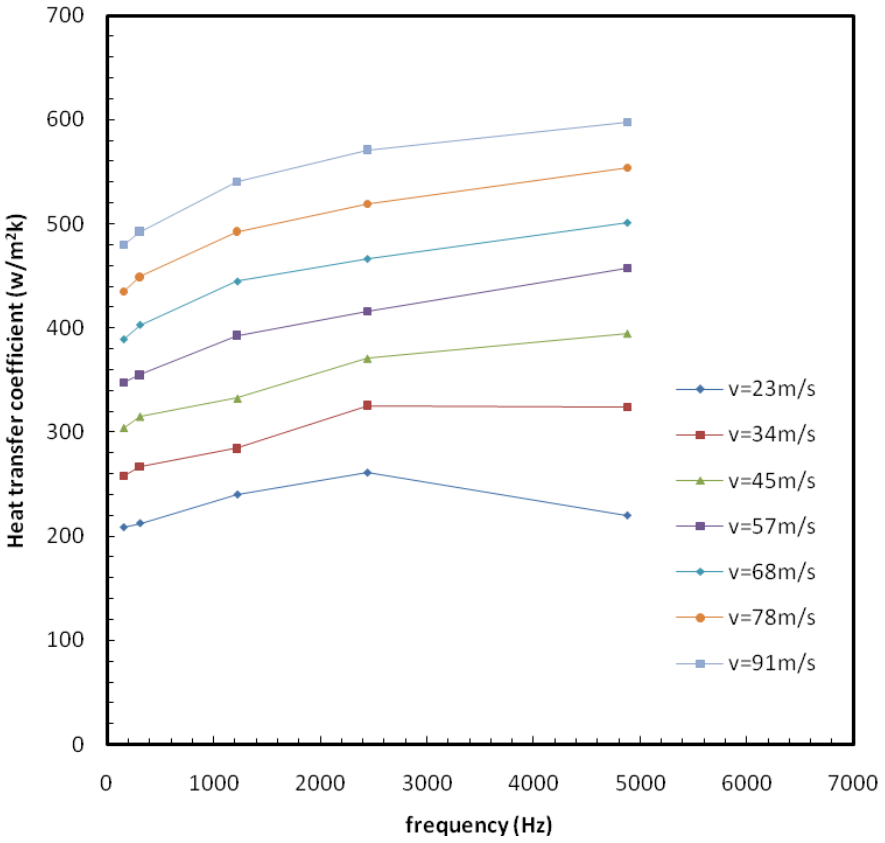

Figure 5.5c Average heat transfer coefficient over all convective surfaces for cases of different frequencies

5.4.3 Different Distances between the Orifice Plate and Fin Tip

The frequency and amplitude of the diaphragm are kept constant in this study (Fig. 5.6). The synthetic jet is operating at 1420 Hz with a spatial-average peak velocity is 52 m/s. The distance between the orifice plate and the fin tip (see Fig. 5.1) is changed from case to case to obtain the effects on heat transfer coefficient. The diameter of the orifice is 1 mm. Figure 5.6 plots the heat transfer coefficients of different convective surfaces with various ratios of axial distance to orifice diameter. It is observed that the cooling performance is not strongly sensitive to changes in axial distance. The maximum difference in heat transfer coefficient is less than 10% in the z/d range 1-7. The outcome

of this study is promising for electronic cooling applications since space is limited for most modules. A change in trend is noted at about z/d = 4-5. This may be due to the impact point of the jet shear layer moving off (with increasing z/d) the tip region. When the fin to be cooled is moved away from the orifice with a z/d values from 1 to 4, the shear layer is more focused on the fin, which causes increases in heat transfer performance. However, when the fin is moved further away from the orifice, with a z/d from 4 to 6, the turbulence will dissipate causing a decrease of heat transfer performance.

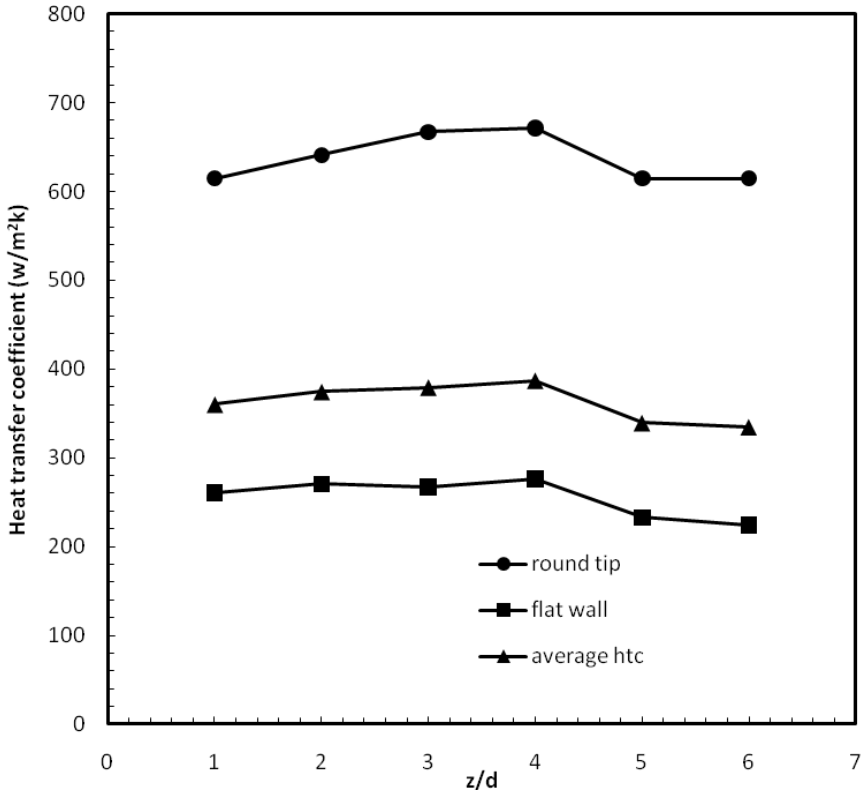

Figure 5.6 Heat transfer coefficients over different convective surfaces at different distances between the orifice and the fin tip

5.4.4 Correlations for the Synthetic Jet

Correlations are developed using regression analysis from the computational data for heat transfer coefficients for the round tip (see Fig. 5.7). The average Nusselt number as a

function of average Reynolds number can be described with the following equation. This applies for one tip-radius-to-orifice-radius ratio, R/r = 1.1.

$$Nu_{avg} = 0.414 \times (\mathrm{Re}_{avg})^{0.54} \tag{5.1}$$

where

$$Nu_{avg} = \frac{h_{avg} d}{k} \tag{5.2}$$

The predicted values are compared to the computational data in Fig. 5.7 The diagonal line is for a perfect match and the plot shows that the equation predicts the relationship reasonably well, since most of the data are close to the diagonal line

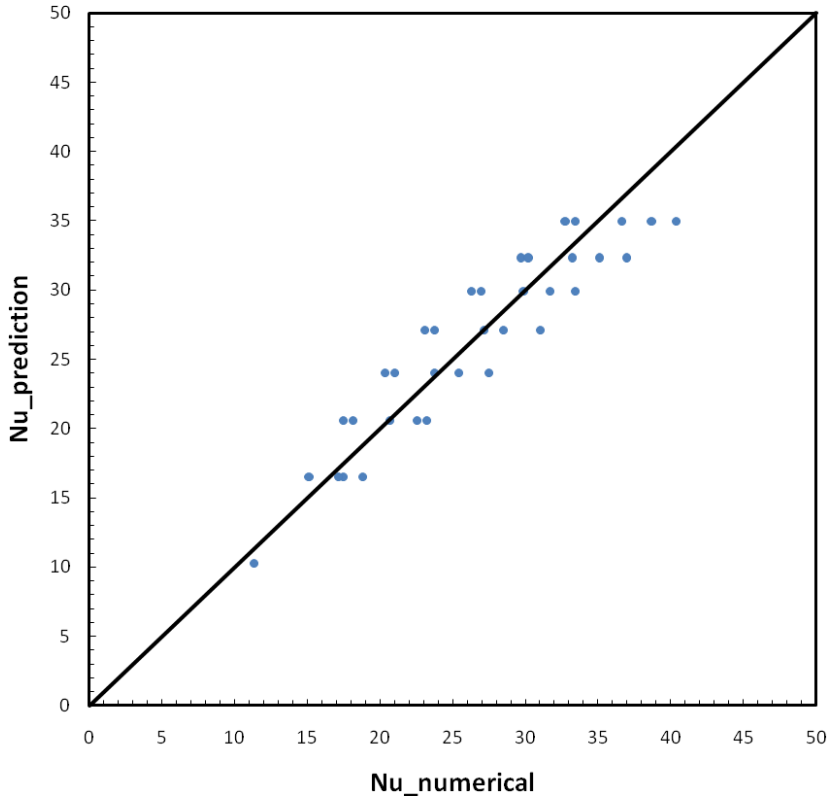

Figure 5.7 Comparison of predicted values and compuational values

5.5 Conclusions

The heat transfer performance using synthetic jet impingement to cool a portion of a fin was investigated computationally.

A numerical model was first validated by comparing its results to experimental data. Then effects on heat transfer of different important parameters were tested. It was found that the amplitude of diaphragm movement was more important in augmenting heat transfer than was the operating frequency. However, the heat transfer coefficient was shown to increase also with frequency. The cooling performance of synthetic jet impingement was found to be rather insensitive to changes in axial distance. Finally, a correlation was developed from the cases computed for average Nusselt number vs. average Reynolds number.

Chapter 6 Fluidic power study of the synthetic jets and agitators

6.1 Introduction

Besides heat transfer enhancement of synthetic jets, the fluidic power consumption is an important parameter to the designers for the cooling device which is important. Thus, fluidic power consumption of synthetic jets and flow agitators is studied numerically and presented herein. The oscillating diaphragm of the synthetic jet or the oscillating plate of the agitator is realized as a moving wall in the numerical model. Dynamic meshes are used in the CFD commercial software ANSYS FLUENT [99] to re-mesh the fluid domain as the moving parts change the flow path geometry. Results of a parametric study are presented for fluidic power consumption with variations in frequency, amplitude, and geometry.

6.2 Synthetic Jets

6.2.1 Numerical Model

In our group, a piezo-bow structure is used to drive a synthetic jet module with 9×25 orifices (Figure 6.2). The dimensions of the diaphragm are 36×100 mm^2. Each orifice is 1×1 mm^2 square and the x-direction and y-direction spacings are 4 mm. A single unit with a cavity dimension of 4×4 mm^2 is used for the analysis of the whole module, capitalizing on symmetry of the geometry (Figure 3). In the model, the oscillating diaphragm of the synthetic jet is modeled as a moving wall by using a layering dynamic mesh, which can be configured with a user defined function in the commercial

Computational Fluid Dynamics (CFD) software ANSYS FLUENT. Movement of the diaphragm is sinusoidal, which matches well with the real situation. All the side walls of the cavity are defined as symmetric boundaries so that the single unit represents well one channel of the whole module (Figure 3).

The flow outside the orifice is calculated with constant pressure boundaries, which allows flow to come in and out simulating a synthetic jet discharging to open air (Figure 3). Three-dimensional, incompressible, time-dependent Reynolds-Averaged Navier-Stokes equations (RANS) are solved with the shear-stress-transport (SST), k-ω turbulence model, which is found to calculate the synthetic jet flow accurately. Fifty time steps are calculated for each cycle and internal iterations continue until the residuals are reduced to 10^{-6}. The surface-averaged static pressure on the diaphragm and the diaphragm velocity are recorded after each time step and the instantaneous fluidic power is calculated using the equation:

$$P = p \times V \times A \tag{6.1}$$

where p is the surface-averaged static pressure of the diaphragm, V is the diaphragm velocity and A is the area of the diaphragm. The calculated instantaneous fluidic power in one cycle is plotted in Figure 6.4. The diaphragm is vibrating at 1000Hz. The peak-to-peak amplitude is 1.2 mm. The instantaneous fluidic power reaches its peak when the velocity of the diaphragm is maximum.

To validate grid independence, one specific case is run under different mesh sizes. The synthetic jet is vibrated at 500 Hz with a peak-to-peak amplitude of 1.6 mm. The orifice is 1×1 mm^2 square. The time-averaged power consumption is compared with those of

cases having increased number of cells (Table 6.1). The results show good convergence. The maximum difference is less than 5%.

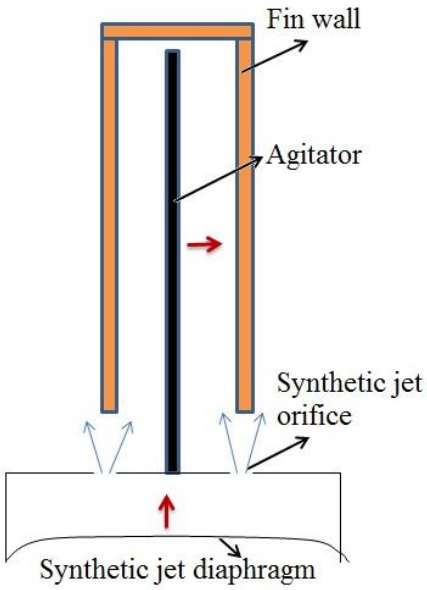

Figure 6.1 Schematic of a single channel within a multi-channel heat exchanger unit having an agitator and synthetic jets

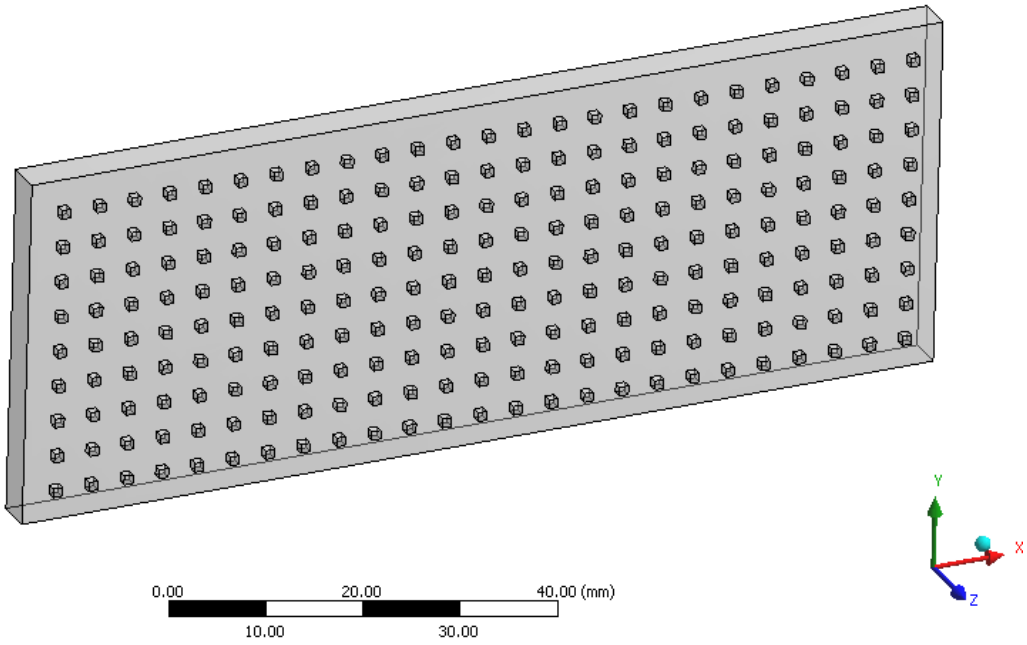

Figure 6.2 A 3-D view of the synthetic jet with 9×25 orifices

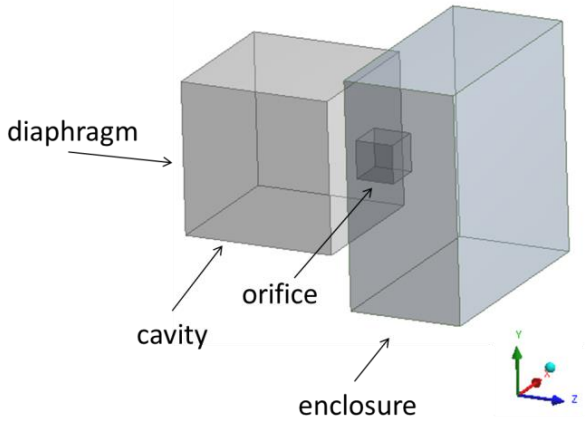

Figure 6.3 Numerical model to calculate the synthetic jet flow

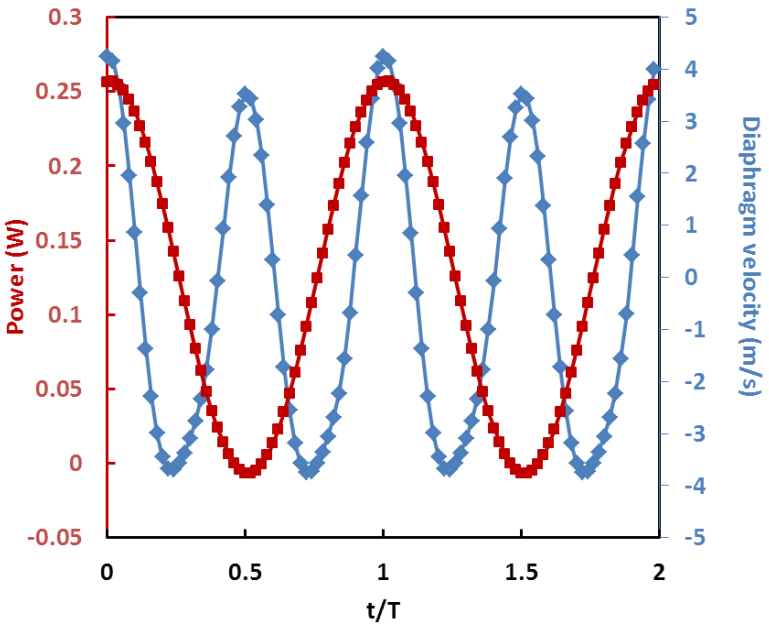

Figure 6.4 Instantaneous power of the synthetic jet over two cycles

Table 6.1 Average fluidic power consumption with different numbers of cells

Number of cells	P_{avg} (W)
200000	0.0334
400000	0.0335
800000	0.0333
1600000	0.0335

6.2.2 Parametric Study

Using the numerical model, a parametric study of the fluidic power consumption was conducted. The effects of the amplitude and frequency of the oscillating diaphragm were documented. Three different frequencies (500, 1000 and 2000 Hz) were tested at various amplitudes. It was found that the power is proportional to the cube of the amplitude (Figure 6.5a) or cube of the frequency (Figure 6.5b). To understand whether the frequency or the amplitude is more important in determining the power, another comparison was done in which the product of the amplitude and frequency was held

constant. The power consumption with the same frequency-amplitude product, but plotted with different frequencies, then different amplitudes indicated that it is the product of frequency and amplitude (only) that determines the power level (Figure 6.6). Since the flow is incompressible, the volume change of the cavity with displacement of the diaphragm equals the volume flow through the orifice. The equation can be written as:

$$2\pi f \times a/2 \times A_{dia} \times \sin(2\pi ft) = V_{jet} \times A_{jet} \tag{6.2}$$

The peak jet velocity is proportional to the product of frequency and amplitude, with fixed diaphragm and orifice areas.

The effects of the orifice geometry were also studied. Three geometries, circular, rectangular and square were compared (Figure 6.7). The orifice areas were unchanged. The diaphragm was driven at 500 Hz with various amplitudes. It was found that the power consumption was nearly the same for each case indicating that the orifice shape is not an important factor toward power consumption so long as the orifice area is unchanged (Figure 6.8).

Next, the efficiency of a synthetic jet is computed. It is defined as the ratio of kinetic energy of the departing jet flow (only the departing jet part of the cycle), E_k, (Equation 6.3) to the energy consumed on the diaphragm during one full cycle ($\eta = E_k/E_{dia}$). The energy E_{dia} is computed using equation (6.4). Figure 6.9 shows the efficiencies of a synthetic jet with a square orifice (1×1 mm^2) under various conditions. The efficiency is very similar from case to case indicating that the efficiency is not strongly dependent on the operational condition of the synthetic jet. The efficiency is found to be high (about

80%), indicating that the synthetic jet is an efficient active device for electronics cooling. This analysis includes only the diaphragm, cavity, and orifice plate. It does not include losses in the mechanism that drives the diaphragm.

$$E_k = \int_0^{T/2} \iint_A V_n dA \times \frac{1}{2} \rho V^2 dt \tag{3}$$

$$E_{dia} = \int_0^T p \times A_{dia} \times V_{dia} dt \tag{4}$$

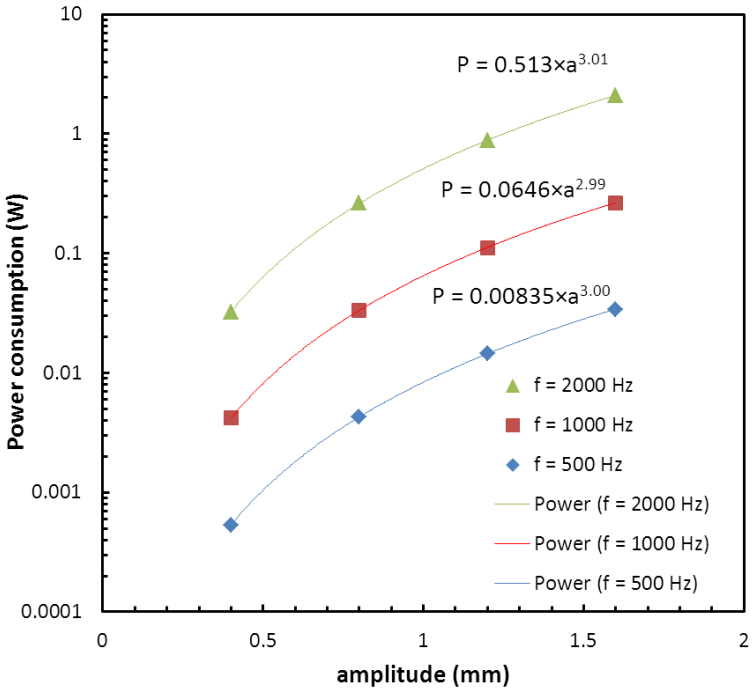

Figure 6.5a Time-averaged power consumption of the synthetic jets at various amplitudes

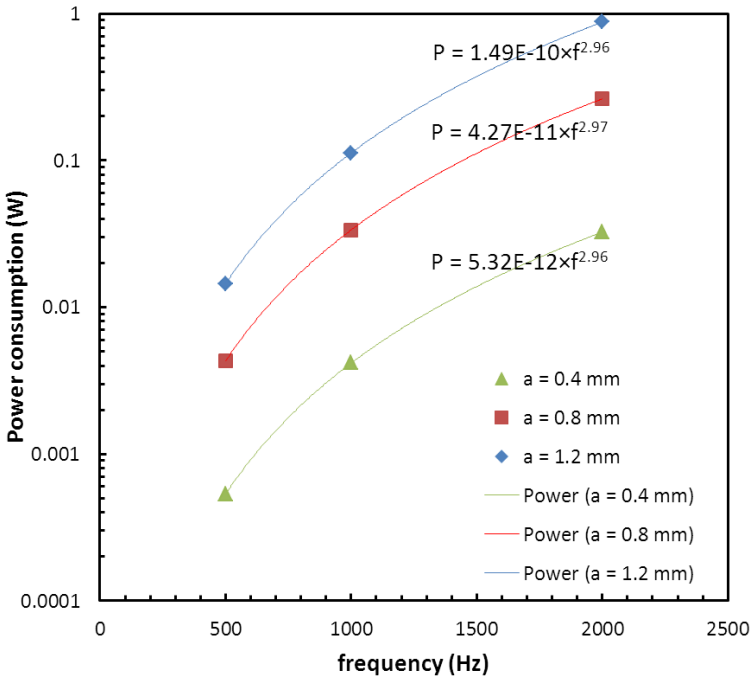

Figure 6.5b Time-averaged power consumption of the synthetic jets at various frequencies

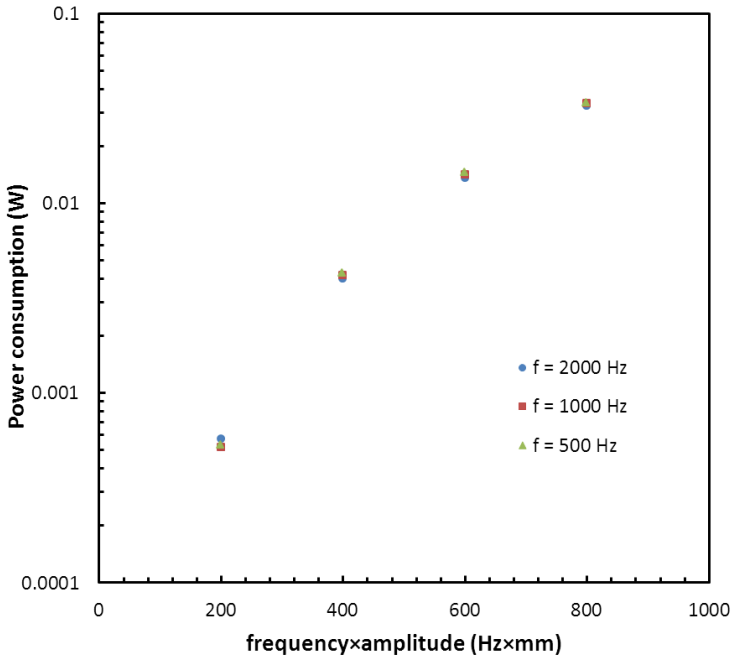

Figure 6.6 Time-averaged power consumption of the synthetic jets at various levels of the product of frequency and amplitude

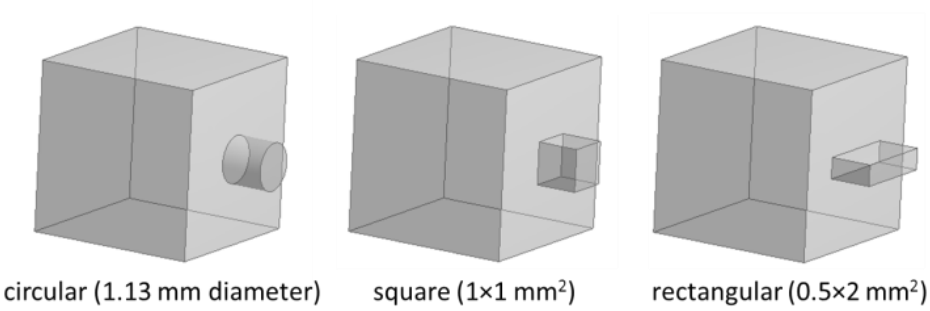

Figure 6.7 Geometries of different orifice shapes

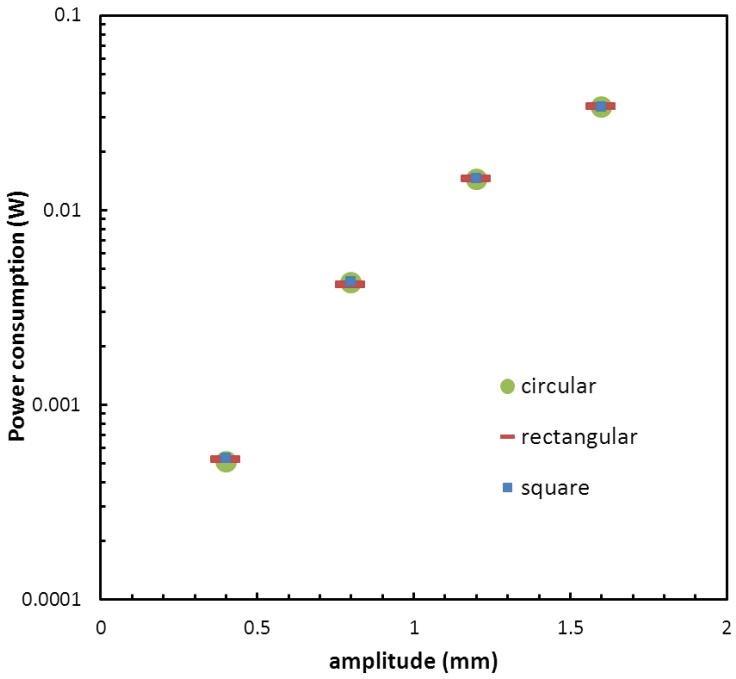

Figure 6.8 Power consumption of the synthetic jets with different orifice shapes

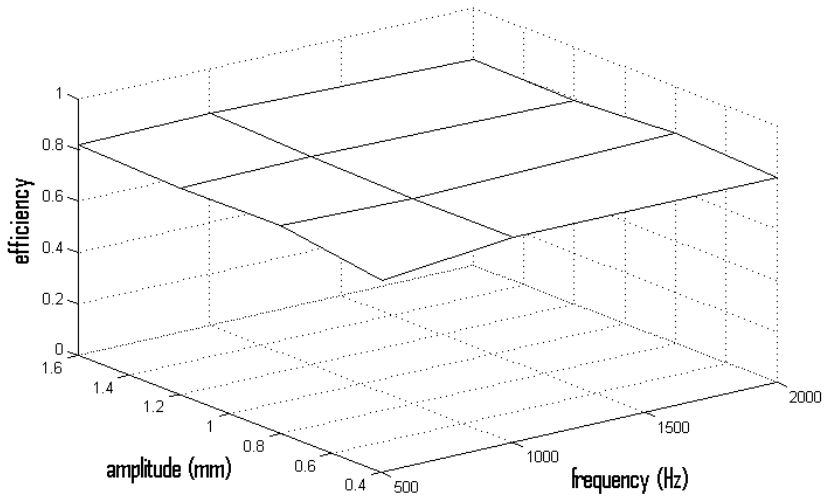

Figure 6.9 Power consumption of the synthetic jets with different orifice shapes

6.3 Oscillating Plate Agitator

The fluidic power consumption of an oscillating plate in a single channel is also studied. Figure 6.9 shows a 3-D view of the numerical model. The channel is 4.3 mm wide, 20 mm high and 50 mm long. The oscillating plate is 1.5 mm thick, 19 mm high and 48 mm long. Thus, the tip gap size between the plate and base of the channel is 1.0 mm. The actuated plate is moving in a translational mode with sinusoidal movement. The flow field is continuously being re-meshed to account for movement of the actuated plate. This is the same methodology as used to simulate the synthetic jet. The fluid flow within the channel is calculated using a transient, pressure-based solver with the shear-stress-transport (SST), k-ω turbulence model. The SIMPLE algorithm is used to solve pressure-velocity coupling. Time step size is chosen in such a way that there are 200 time steps for each cycle. For each time step, the internal iterations continue until the residuals have

been reduced to 10^{-6}. The total force on the plate in the x-direction and the plate velocity in the x-direction are recorded after each time step so that the instantaneous fluidic power can be calculated using the equation:

$$P = F_x \times V_x \tag{6.5}$$

Figure 6.11 shows the instantaneous power consumed by the agitator over one cycle when the frequency is 1000 Hz and the peak-to-peak amplitude is 0.4 mm. The power curve shows a peak when the agitator velocity reaches its maximum, similar to the synthetic jet (Figure 6.11) results. To validate grid independence, one specific case is run under different mesh sizes. The agitator is vibrated at 1000 Hz with a peak-to-peak amplitude of 0.8 mm. The time-averaged power consumption compared with that of cases having increased number of cells is shown in Table 6.2. The results show good convergence. The maximum difference is less than 10%. The power consumed by plate agitators to work against the fluid pressure field is found to be proportional to almost the cube of the amplitude or the frequency, as computed for the synthetic jet case (Figure 6.12).

One explanation for this is that the pressure drop caused by the moving parts is due to the inertial losses of the flow which are proportional to the square of the velocity (equation 6.6). The force is linear with the pressure drop (equation 6.7) and the power is the product of the force and velocity (equation 6.8).

$$\Delta p \propto V^2 \tag{6.6}$$

$$F \propto \Delta p \tag{6.7}$$

$$P \propto F \times V \tag{6.8}$$

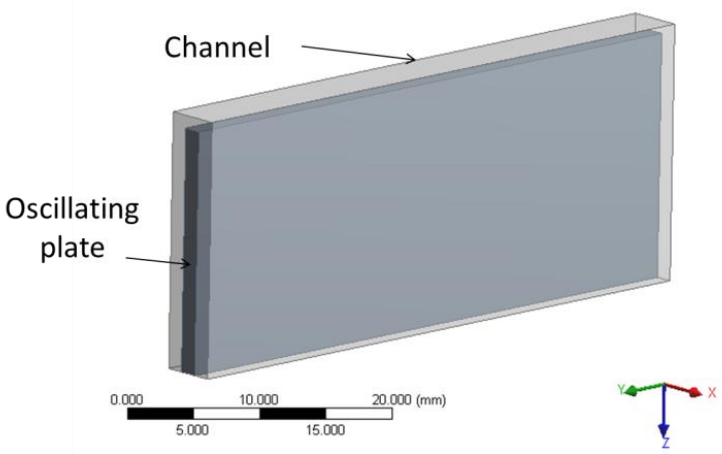

Figure 6.10 Schematic of the agitator in a single channel

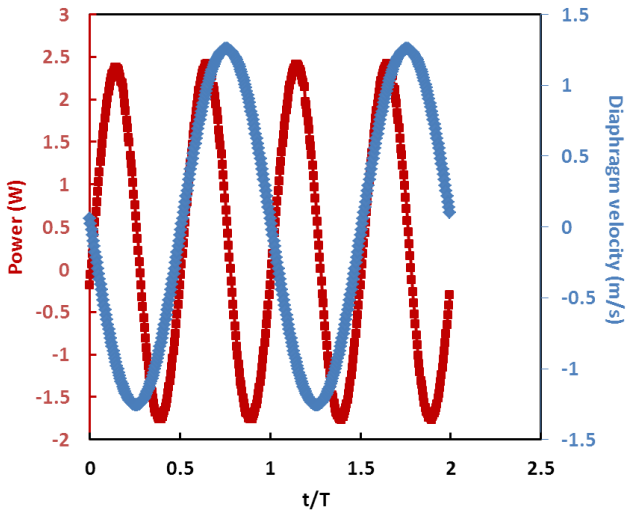

Figure 6.11 Instantaneous power of the agitator in two cycles

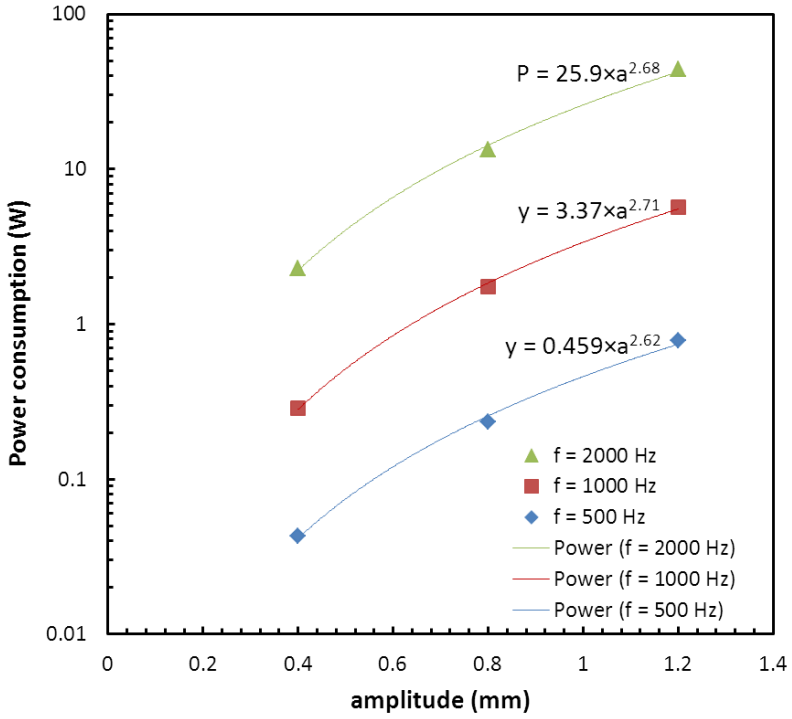

Figure 6.12a Power consumption of the oscillating agitator at various amplitudes

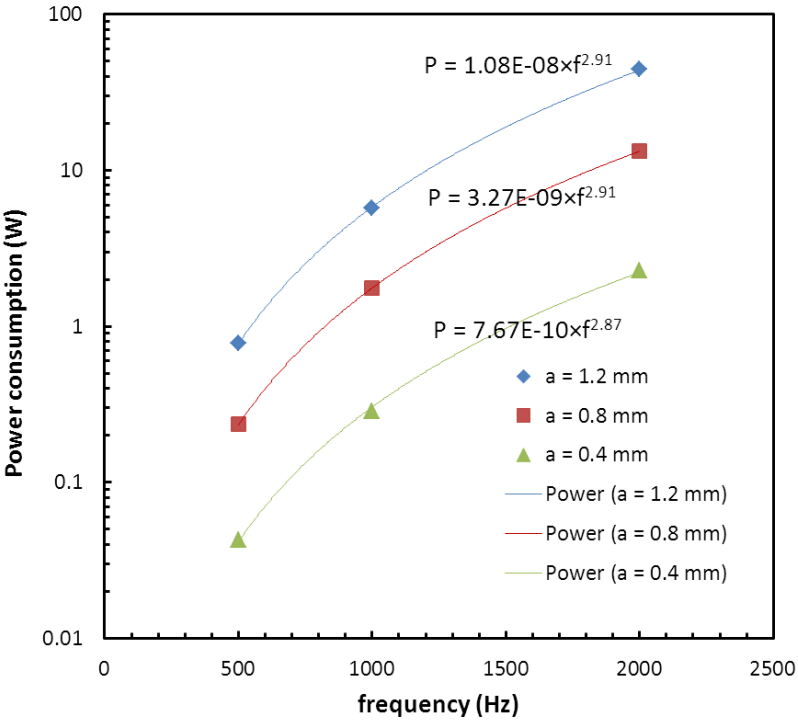

Figure 6.12b Power consumption of the oscillating agitator at various frequencies

Table 6.2 Average fluidic power consumption with different numbers of cells

Number of cells	P_{avg} (W)
100000	1.82
200000	1.75
400000	1.72
800000	1.71

6.4 Conclusions

The fluidic power of active devices such as synthetic jets and oscillating plate agitators used in enhancing heat transfer has been studied numerically. The dynamic mesh method in the CFD software was used to remesh the fluid domain as the diaphragm of the synthetic jet or oscillating plate of the agitator is moving. The instantaneous fluidic power consumption of both synthetic jets and oscillating plate agitators show sinusoidal curves. The time-averaged fluidic power consumption by the synthetic jets is proportional to the cube of the amplitude or cube of the frequency. The frequency and amplitude are found to be equally important to fluidic power consumption. Synthetic jet orifices of three different shapes (circular, square and rectangular) with the same orifice area were tested to find that the orifice shape is not an important factor to the fluidic power if the orifice area is the same. The efficiency of a synthetic jet, defined as the ratio of kinetic energy of the departing flow to energy supplied to the diaphragm over a full cycle, is independent of operating conditions and is high (about 80%). The time-averaged fluidic power consumption of the agitator is also proportional to the cube of the amplitude or cube of the frequency.

Chapter 7 Acoustic Measurement and Noise Reduction

7.1 Introduction

The agitator plates and synthetic jets have been found to be very effective in enhancing heat transfer. However, these active devices, especially when they are operating at high frequencies, generate noise that adds to the noise of the traditional fans. The noise issue has been studied. An one-dimensional analytical model is used to calculate transmission losses for different muffler designs. The sound level is calculated for each to find the optimal design. Noise levels of piezoelectrically-driven agitators and synthetic jets under different operating conditions are measured using a microphone. The acoustic characteristics of these active devices are obtained using Fast Fourier Transform (FFT) analysis. Base on the power spectrum, a circular expansion chamber, one of the candidate muffler designs, is offered for noise reduction.

7.2 Acoustic Measurements

7.2.1 Introduction of Agitator and Synthetic Jets

The agitator and the synthetic jets are driven by an oval loop shell amplifier coupled with a piezo stack actuator (Figure 7.1). When the piezo stack actuator contracts and expands in the horizontal direction with a sine-wave voltage input, the oval loop shell transforms the movement of the piezo stack actuator to the vertical direction and magnifies its amplitude at the same time [101]. The agitator is formed when a carbon fiber composite blade is attached to the oval loop shell actuator (Figure 7.2). When the

oval loop shell actuator is connected to a jet frame with multiple orifices on it (Figure 7.3), the synthetic jets are realized [102]. The impinging synthetic jets are found to be effective in enhancing heat transfer of an air-cooled heat sink with channel flow [103].

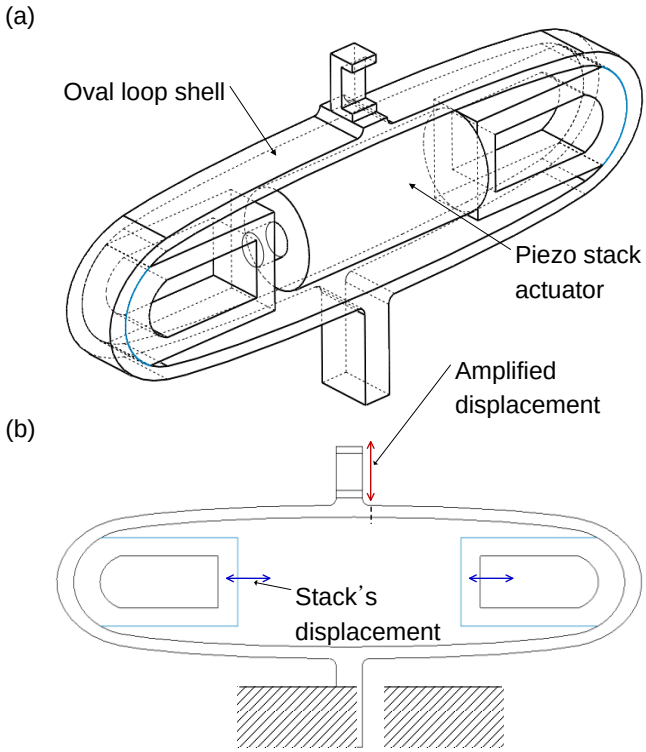

Figure 7.1 A 3-D view (a) and side view (b) of the oval loop shell actuator

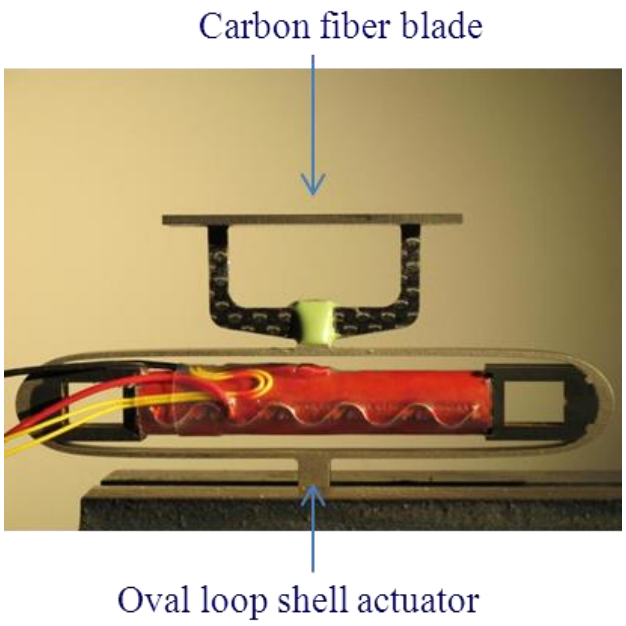

Figure 7.2 actual agitator

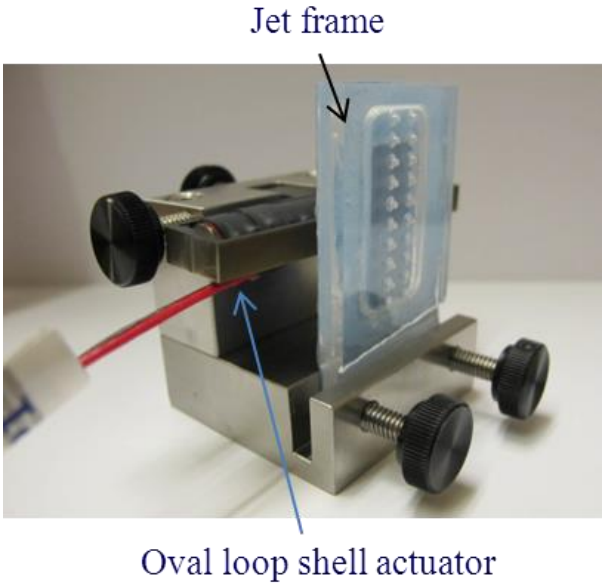

Figure 7.3 actual synthetic jets

7.2.2 Acoustic Experimental Results

The noise levels of the agitator and synthetic jets are measured using a 12.5 mm (0.5 inch) diameter Free-field microphone (Type 40AE) from GRAS Sound & Vibration. The microphone is put one meter away from the active devices. The unsteady pressure fluctuation is recorded by the microphone and the root-mean-square (RMS) pressure fluctuation is calculated. With a reference pressure of 20 μPa, the sound pressure level, widely used to describe the noise level in acoustics becomes: $SPL = 10\log_{10}[p_{rms}^2 / p_{ref}^2]$ in the dB scale. The noise levels of the agitator operating at two different resonance frequencies (600 Hz and 900 Hz) are measured at various input voltages (Figure 7.4). The RMS pressure fluctuation is found to increase almost linearly with an increasing peak voltage input (Figure 7.5). The maximum noise level of the agitator is found to be as high as 100 dB which is harmful to the human ear. The sound level of the agitator operating at higher frequencies is found to be much larger than when operating at lower frequencies. The maximum noise level of the synthetic jet in our design is found to be about 85 dB with a maximum input of 200 volts. Using the Fast Fourier Transformation (FFT) analysis, the power spectrum of the unsteady pressure fluctuation is obtained. Figure 7.6 shows the power spectrum for operating at a bow structure resonance frequency of 900 Hz and a voltage input of 72 V. It is found that the acoustic energy resides within narrow ranges of several specific frequencies which are integer multiples of the operating frequency of the agitator (900 Hz). However, almost 90% of the total acoustic energy is in the first frequency peak, which is the operating frequency of the agitator (Table 7.1). The noise reduction of this specific frequency is of primary importance to overall noise reduction. Figure 7.7 shows the acoustic characteristics of noise generated by the

synthetic jets operating at a resonance frequency of 1250 Hz and a peak voltage of 80V. As with the agitator drive, the acoustic energy is concentrated in several narrow bands of frequencies that are integer multiples of the operating frequency of the synthetic jets (1250 Hz). Most acoustic energy (around 90%) is found in the first two peak frequencies (1250 and 2500 Hz -- see Table 7.2).

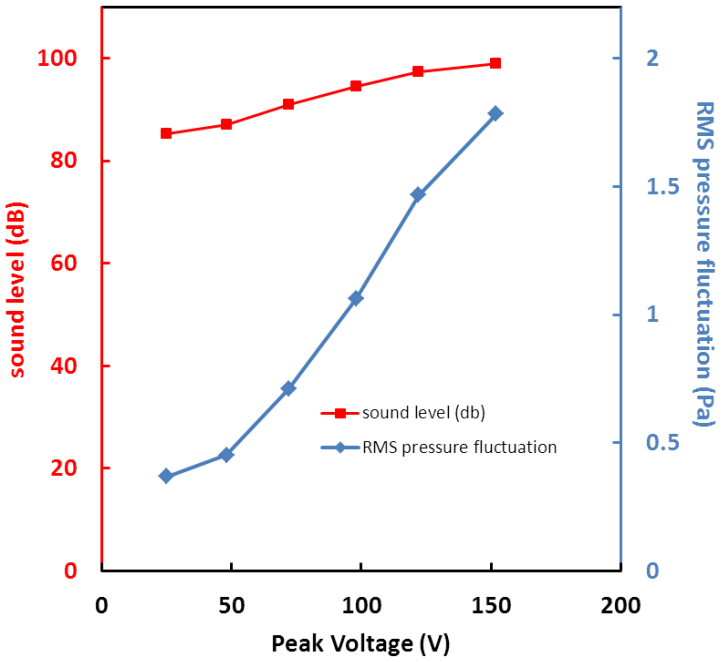

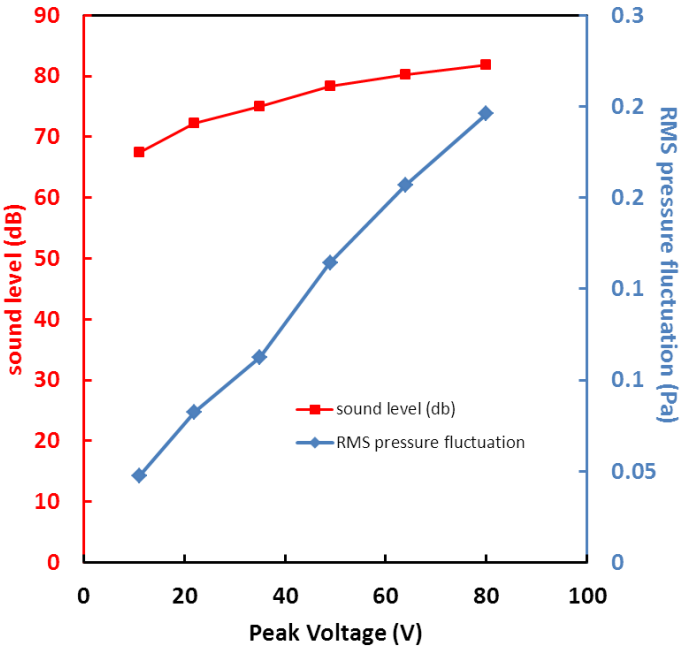

Figure 7.4 A-weighted sound pressure levels of the agitator with different driving voltages. The agitator is operating at 900 Hz (a) and 600 Hz (b)

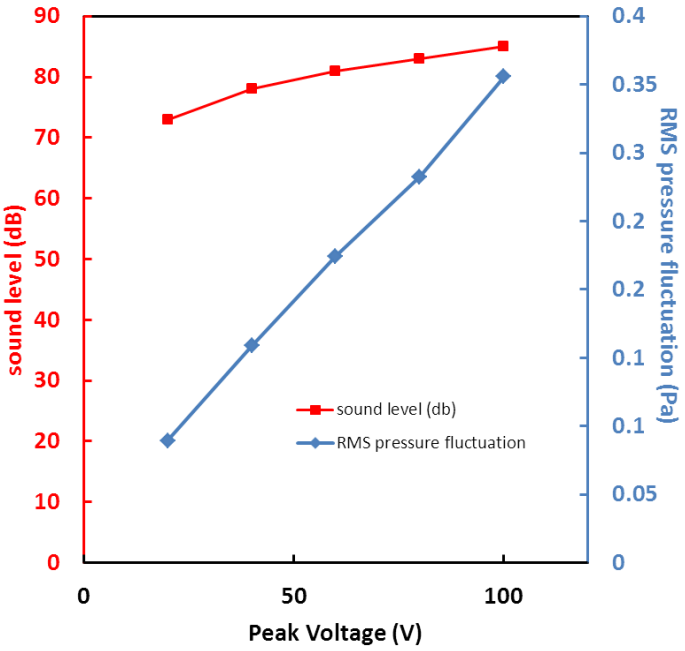

Figure 7.5 A-weighted sound pressure level (SPL) of synthetic jets operated at different

driving voltages and 1250 Hz frequency

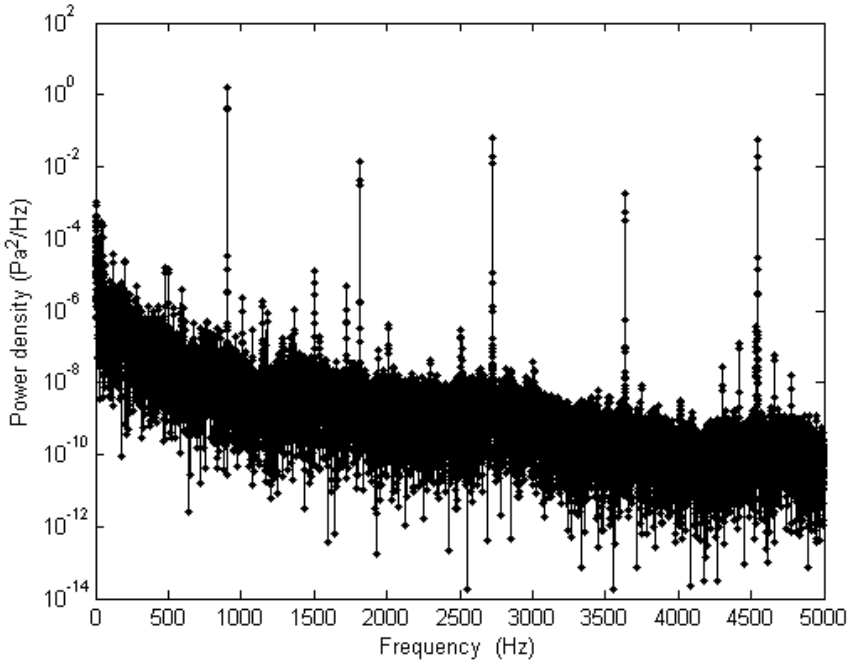

Figure 7.6 Power spectrum of the pressure fluctuation of the synthetic jets when the agitator is operating at the bow drive resonance frequency of 900 Hz and a peak voltage of 72 V

Table 7.1 Ratios of power in the first peak frequency (900 Hz) band to total power for operation at different input voltages and at the bow drive resonance frequency of 900 Hz

Voltages (V)	**Ratio (%)**
25	**85**
48	**89.3**
72	**92.3**
98	**90.9**

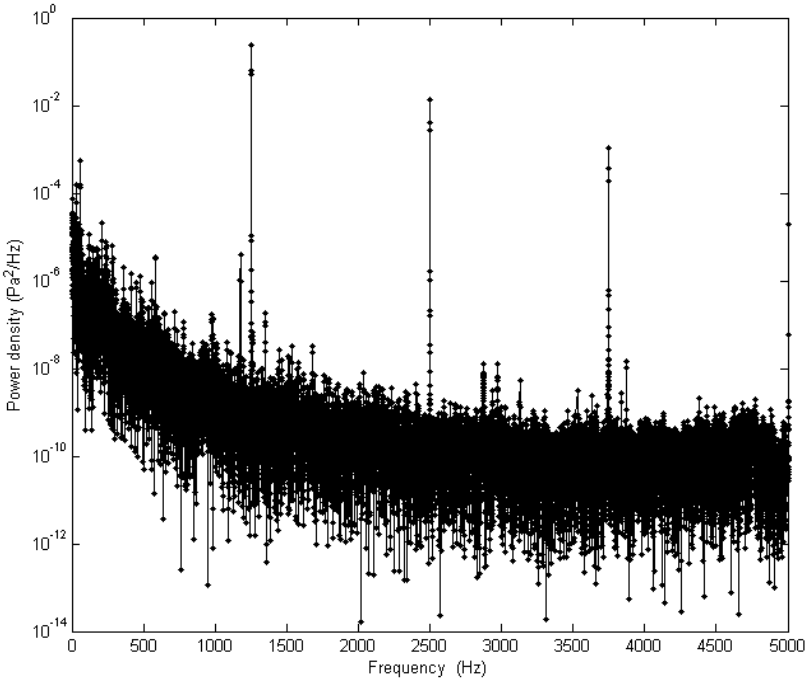

Figure 7.7 Power spectrum of the pressure fluctuation of the synthetic jets (synthetic jets are operating at the resonance frequency of 1250 Hz with an input voltage of 80)

Table 7.2 Ratios of the power in the peak frequency bands to the total power for different input voltages (the synthetic jets are operating at the resonance frequency of 1250 Hz)

Voltages (V)	Ratio of the first peak (1250 Hz)	Ratio of the second peak (2500 Hz)	Sum of the first and second peaks
20	**83.3%**	**6.18%**	**89.5%**
40	**75.7%**	**11.9%**	**87.6%**
60	**68.6%**	**16.1%**	**84.7%**
80	**68.3%**	**18.6%**	**86.9%**

7.3 Noise Reduction

7.3.1 Noise Reduction of Different Types of Enclosures

The well-sealed enclosures are found to be effective in insulating noise with high frequency. It showed large transmission losses (TL) in cases documented in the literature. Thus, we tested aluminum boxes with various thicknesses for noise control (Fig. 7.8). The sound level of the synthetic jet was measured using a microphone sensor in the ambient to have a value of 82 db. The synthetic jet was operated at a frequency of 1250 Hz and a peak-to-peak voltage of 80 V. To measure the sound reduction of each aluminum box, the synthetic jet was put in the box and the box lid was well sealed. The sound level with the synthetic jet in the box and the sound reduction level are recorded in Table 7.3. It was observed that the sound reduction increased with an increase of thickness of the aluminum box walls. The sound reduction of the aluminum box with 4 mm thick walls was as high as 26 db. A double wall design was tested with two aluminum boxes, one inside the other, with porous material put in the space between the inner and outer walls (Fig. 7.8 d)). The combination of two aluminum boxes was able to reduce the transmission of sound waves effectively and the porous material was able to dissipate part of the energy. This design was measured to have a sound reduction of 30 db.

Although the box with double walls was found to be very effective in reducing noise, it can't be used in the cooling system unless openings are made to allow the flow to go through. Thus, the muffler, a popular noise reduction device which is able to allow through flow, is applied with the enclosures to reduce noise from the cooling system.

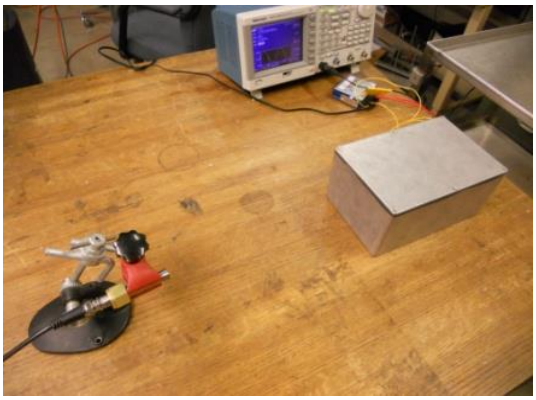

(a) 2 mm thick

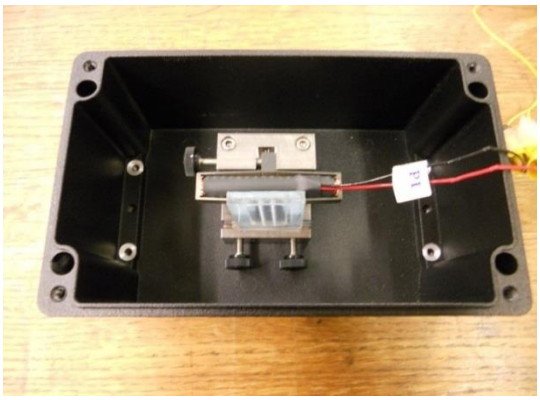

(c) 4 mm thick

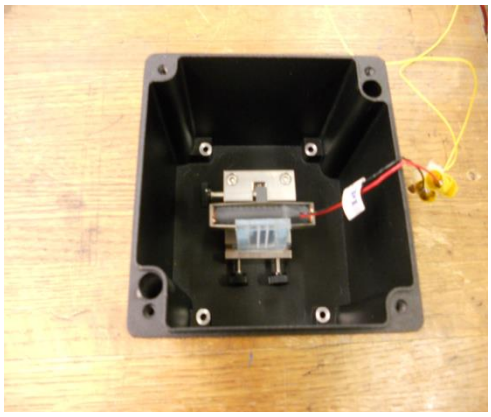

(b) 3 mm thick

(d) double leaf box

Figure 7.8 Different boxes

Table 7.3 Sound reduction measurements for different boxes

	Sound level with the box	**Sound reduction**
2 mm Aluminum box	**62 dB**	**18 dB**
3 mm Aluminum box	**58 dB**	**22 dB**
4 mm Aluminum box	**54 dB**	**26 dB**
double leaf box	**50 dB**	**30 dB**

7.3.2 Noise Reduction Using Mufflers

Most acoustic energy is found in narrow bands of several frequencies that include the operating frequency of the piezoelectrically-driven agitators or synthetic jets. The circular expansion chamber, a candidate muffler design, is proposed to decrease the noise, since it is able to decrease the noise level effectively at selected frequencies with proper choices of dimensions. A circular expansion chamber is basically made of three tubes with different diameters (Figure 7.9).

A reflected sound wave due to a change in cross section which is different in phase from the incident sound wave is generated [23]. The incident wave can be canceled by the reflected wave when the muffler is properly designed. Then, the sound level is decreased. The transmission loss (TL) is widely used to describe the performance of a muffler [22].

$$TL = 20\log_{10}[p_i / p_t] \tag{7.1}$$

where p_i is the RMS pressure fluctuation at the noise source side of the muffler and p_t is the RMS pressure fluctuation at the other side of the muffler. The transmission loss describes the amount of incident sound wave that is muffled. It can be obtained numerically or experimentally. The transmission loss of a circular expansion chamber can be obtained by solving the one-dimensional wave equation [26].

$$TL = 10\log_{10}\left[1+\frac{1}{4}\left(\frac{D^2}{d^2}-\frac{d^2}{D^2}\right)^2 \sin^2 kL\right] \tag{7.2}$$

where D, d, and L are dimensions of the expansion chamber (Figure 7.9) and k is the wave number of the sound wave ($k = 2\pi f/c$) and c is the speed of sound. It was found that equation (7.2) can predict transmission loss accurately at low frequencies [26]. According to the equation, the expansion ratio (D/d) affects only the amplitude of the transmission loss (Figure 7.9); while the length of the expansion chamber affects the frequency characteristics (Figure 7.11). The transmission loss exhibits multiple dome-shaped characteristics in the frequency domain displaying increasing transmission loss with increases in expansion ratio (D/d).

The analytical model was used to design the expansion chamber of the muffler used for reduction of the agitator and synthetic jet actuators' noise. Figure 7.12 shows the muffler design sequence. The power spectrum of the measured pressure signal is first filtered using an A-weighting filter, a filter that is designed to weight toward the frequencies to which the human ear is sensitive. The A-weighted power spectrum is then reduced by the transmission loss, as obtained from equation (7.2), associated with the particular expansion chamber. Finally, the RMS pressure fluctuation is evaluated by calculating the total area under the power spectrum curve so that the sound pressure level is obtained ($SPL = 10\log_{10}[p_{rms}^2 / p_{ref}^2]$).

By applying the above processes, the performance characteristics of different expansion chamber designs can be compared for the specific noise of the agitator and synthetic jets. The synthetic jets operating at a resonance frequency of 1250 Hz with a voltage of 80 V input and the agitator operating at 900 Hz with a voltage of 72 V are used for the analysis. Figures 7.13 and 7.14 show the expansion chamber lengths that give

lowest sound levels. The choice of expansion chamber length is independent of the expansion ratio (D/d), since the expansion ratio does not affect the frequency characteristics of the transmission loss. However, the sound level is found to decrease with increasing expansion ratios. The expansion chamber with the optimal length and maximum expansion ratio is able to reduce the sound level from 83 dB to 59 dB for the synthetic jet noise and from 91 dB to 67 dB for the agitator noise.

To verify the performance of the expansion chamber design obtained analytically, the expansion chamber with an expansion ratio of 6 (D= 152 mm or six inches, d= 25 mm or one inch) and a length, L, of 51 mm (two inches) was fabricated and tested. It is constructed from a metal tube and two metal plates with 25 mm (one inch) diameter circular holes on them (Figure 7.15). The measured sound level of the synthetic jets in an isolated box is 83 dB without the expansion chamber. When the expansion chamber is added, the noise level is decreased to 63 dB, which is close to the analytical value of 59 dB.

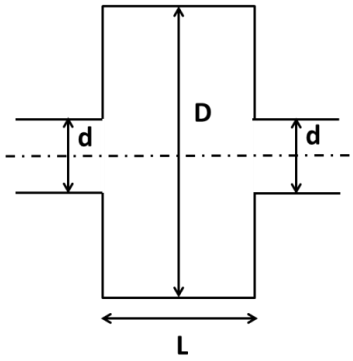

Figure 7.9 The expansion chamber geometry

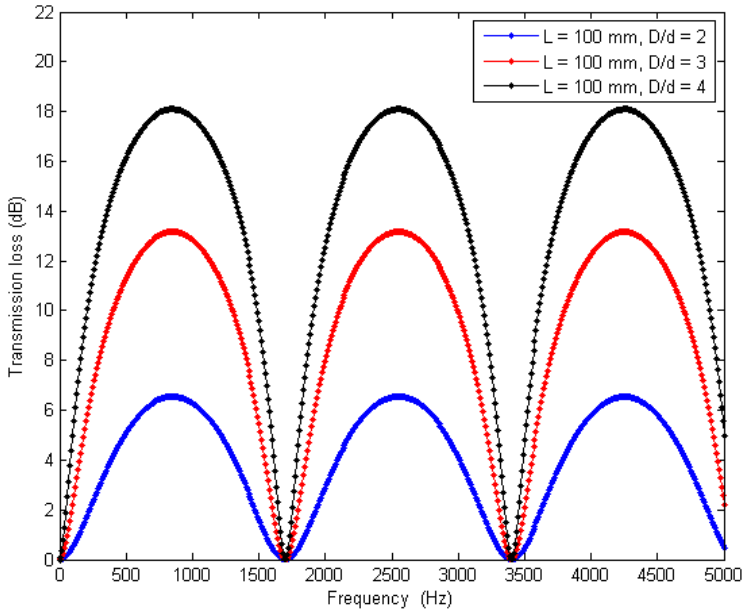

Figure 7.10 Transmission loss vs. frequency the expansion chambers of different expansion ratios (D/d) but with the same length

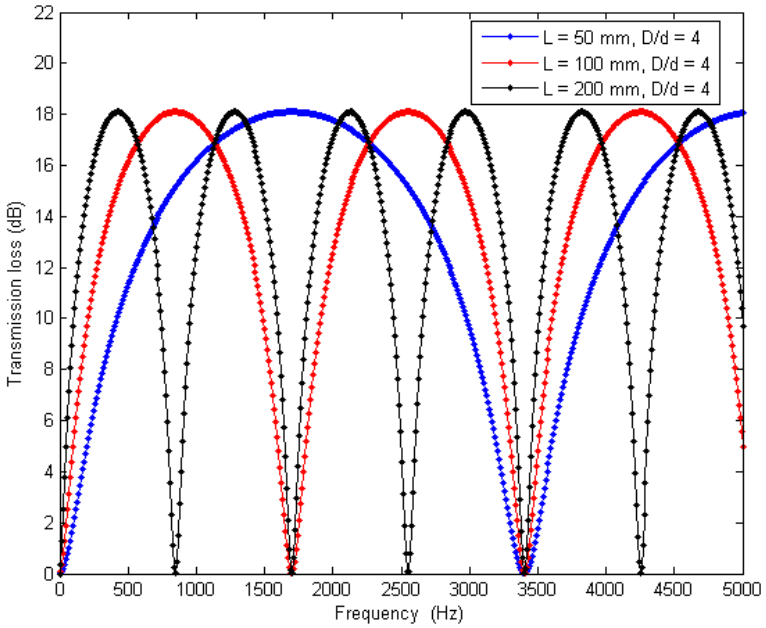

Figure 7.11 Transmission loss vs. frequency of expansion chambers of different lengths but with the same expansion ratio (D/d).

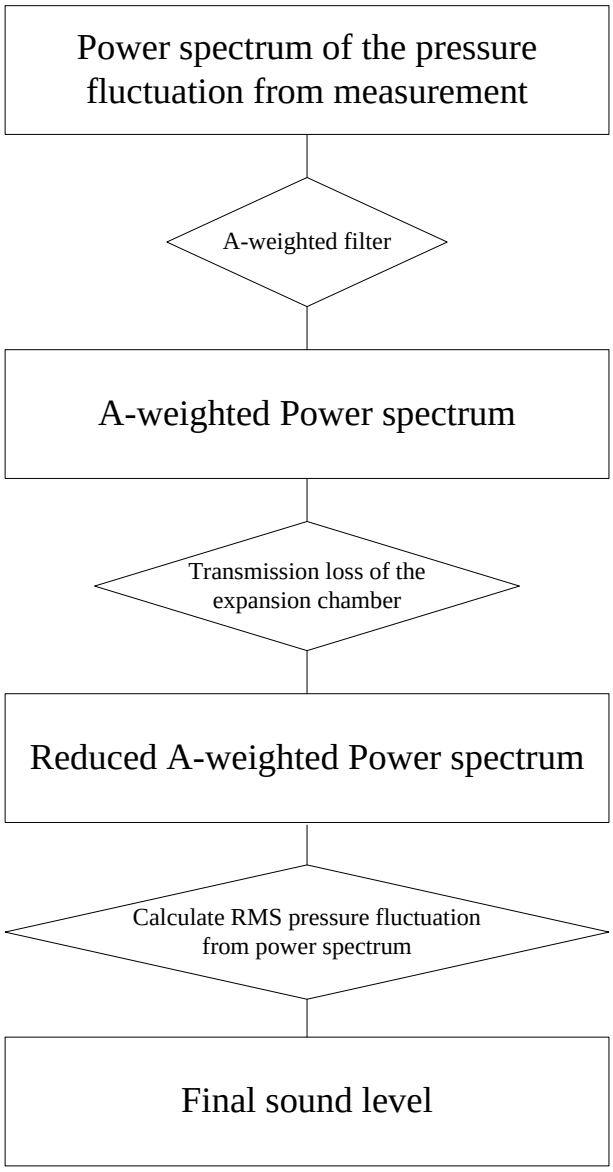

Figure 7.12 The process to calculate the sound level of the active devices after the expansion chamber is applied

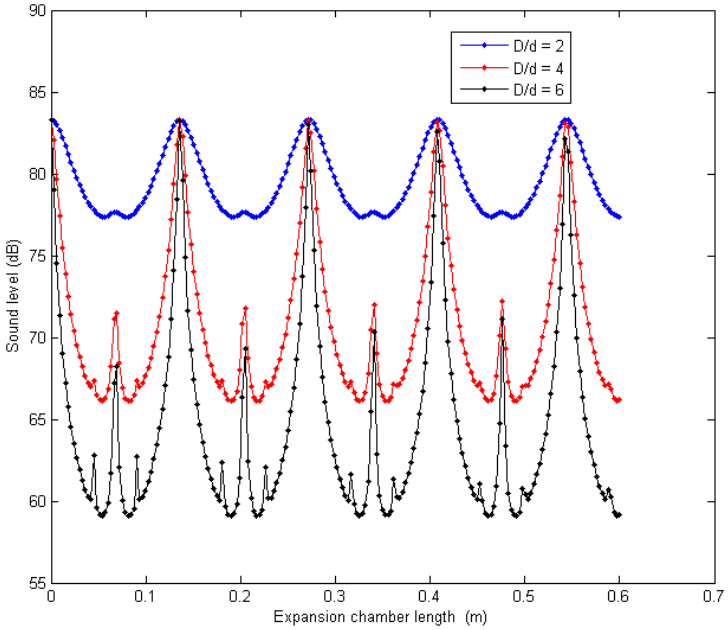

Figure 7.13 Sound level of the agitators after an expansion chamber is applied (synthetic jets are operating at the drive resonance frequency of 1250 Hz with a voltage of 80 V input)

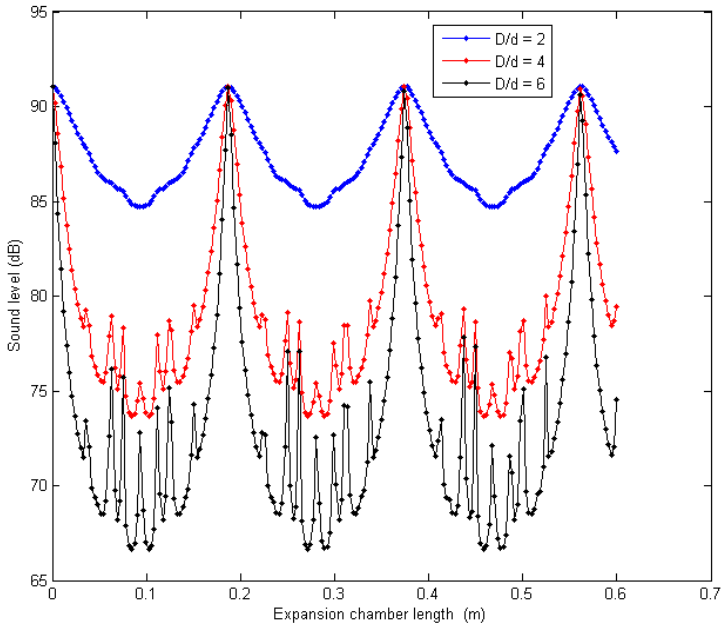

Figure 7.14 Sound levels of the agitator drives after the expansion chamber is applied

(agitators are operating at a resonance frequency of 900 Hz with a voltage of 72 V input)

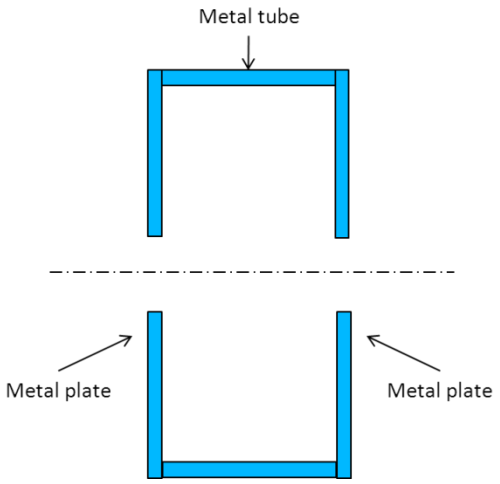

Figure 7.15 Schematic of the fabricated expansion chamber

7.3.3 Noise Reduction of the System

The mufflers have been found to decrease the noise effectively so that they are used to decrease the noise level of the actual cooling module. The noise of the whole cooling includes the noise from two synthetic jets and two agitators running (four piezo-bows totally). The two synthetic jets are operating at about 840 Hz and the two agitators are operating at about 800 Hz. The noise level of the whole cooling module is about 91 dB. A box has been used for the noise reduction measurement of the muffler in the application of the whole module (Figure 16 and Figure 17). The inlet orifice diameter (d) is 2 inches. In the sound test facility, a muffler is put on the two ends of the box which is a setup close to the real system. Four cases are tested to find the noise reduction performance of the muffler (Figure 18) and Table 7.4 shows the measurement results. The noise of the whole cooling module in the open air is first measured and the level is

about 91 dB (case 1). The cooling module is then put inside a box and the box is well sealed. The measured sound level is about 72 dB (case 2). Then, a 51 mm (2-inch) diameter hole is drilled on both sides of the box to simulate the real case which allows channel flow to go through. The noise level is found to increase to 81 dB which indicates that the hole is an important factor for the noise (case 3). The mufflers are then added to reduce the noise level (case 4). It is found that the noise level can be decreased to 65 dB by adding the mufflers.

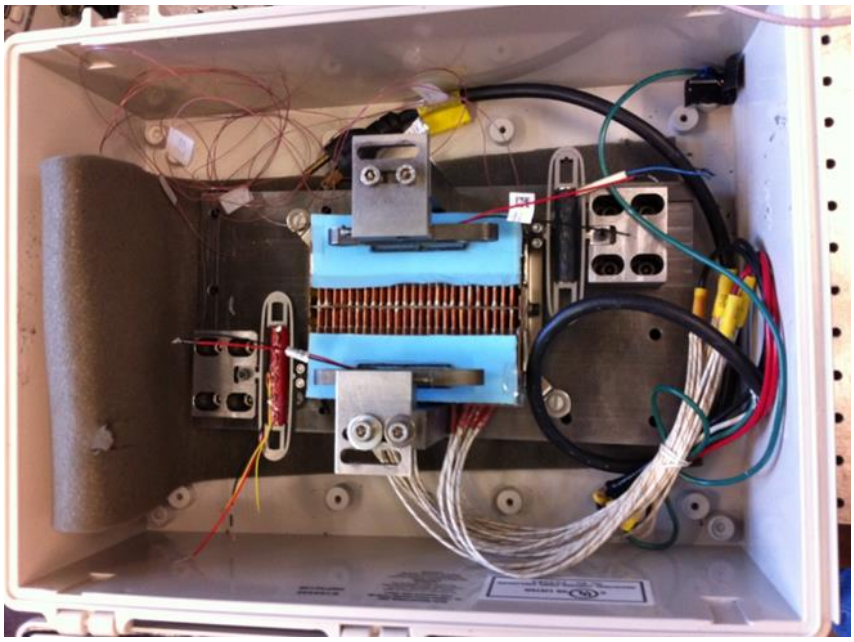

Figure 7.16 Whole cooling module inside a box

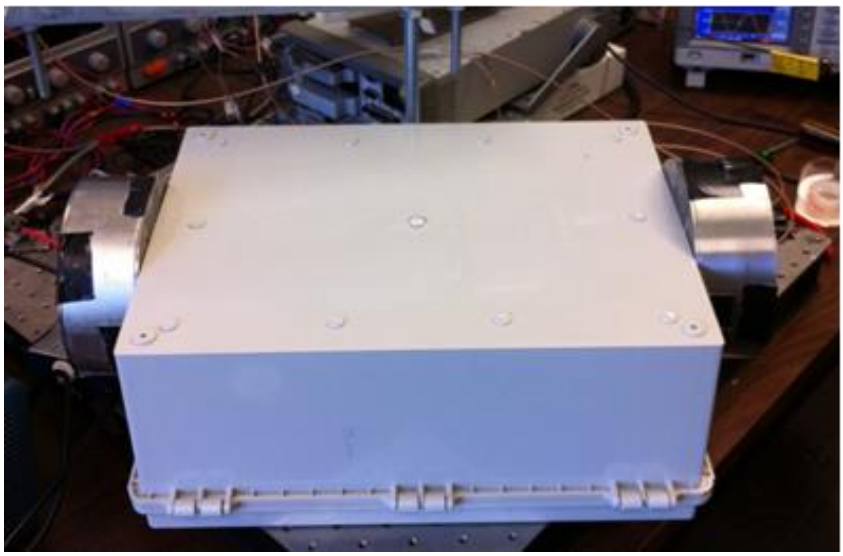

Figure 7.17 The noise reduction test module

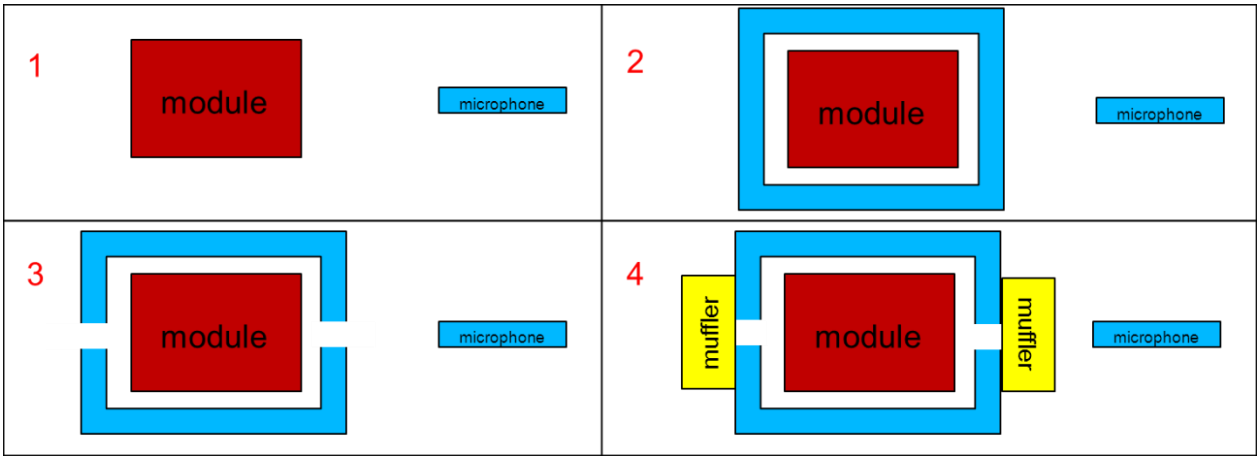

Figure 7.18 The picture of the sound test facility

Table 7.4 The test results of the different cases

case	description	Noise level (dB)
1	The whole module in the open air without a box	91
2	The whole module inside a box without holes	72
3	The whole module inside a box with 2-inch holes on each side	81
4	The whole module inside a box with 2-inch holes and a muffler on each side	65

7.4 Conclusions

Agitators and synthetic jets driven by oval loop shell actuators are applied to enhance heat transfer in electronics cooling modules. The noise levels they generate are measured using a microphone held one meter away from the active drive devices. Their sound pressure levels are found to increase with increases linearly with input voltages and remarkably more steeply with frequency. The maximum noise level of the agitator operating at the higher resonance frequency of 900 Hz is as high as nearly 100 db.

A fast Fourier transform analysis is applied to document the acoustic characteristics. In the power spectrum plot, the acoustic energy is found to concentrate in narrow ranges at several specific frequencies which are integer multiples of the operating frequency of the active device drives. For the agitator, most acoustic energy (around 90%) is found in a narrow range about the operating frequency of the agitator. For the synthetic jets, most of the acoustic energy (around 90%) is found in a narrow band about the operating frequency of the synthetic jets and another near twice the operating frequency.

Based on the acoustic characteristics of the noise generated by the agitator and synthetic jet drives, a circular expansion chamber, one of several candidate mufflers considered, is offered to reduce the noise. A one-dimensional analytical model is used to calculate the transmission losses for different muffler designs. The model is able to generate transmission loss for different frequencies when dimensions of the expansion chamber are supplied. It is found that transmission loss of the expansion chamber is related to only the expansion ratio and the length of the chamber, and the frequency of the sound. The transmission loss increases with increases in expansion ratio of the muffler. The length of the expansion chamber is found to affect only the frequency

attenuation characteristics. The analytical model is combined with the power spectrum of the noise generated by the agitator drives of the synthetic jet drives to determine the sound level when the expansion chamber is applied. The related performance characteristics of different expansion chamber designs are determined. It is found that optimal expansion lengths exist, providing the greatest sound level attenuation. The expansion chamber with an optimal length and expansion ratio (D/d) of 6 decreases the sound level of the synthetic jets from 83 dB to 59 dB and decreases the sound level of the agitator drives from 91 dB to 67 dB. To verify the performance of the expansion chamber design, which was obtained analytically, we fabricated an expansion chamber with an expansion ratio of 6 and a length of 51mm, two inches). This expansion chamber decreased the noise level from 83 dB to 63 dB, as verified experimentally. The reduced sound level of the measurement is close to that obtained analytically (59 dB), indicating that the analysis is able of predicting the performance of different expansion chamber designs.

The mufflers are finally applied to reduce the noise of the whole cooling system with two agitators and two synthetic jets running. The four piezo bows are running at about 800 Hz. The acoustic measurement found that the noise level can be reduced from 91 dB to 65 dB

Chapter 8 Conclusions

The present study has investigated synthetic jet impingement as an alternative cooling method for electronics cooling compared to other traditional cooling technologies. The possibility of the synthetic jet in the application of electronics cooling has been investigated. The practical cooling device using synthetic jets has been designed, fabricated, and tested. Compared with previous studies of synthetic jets, this work provides a new aspect view by using experimental and numerical methods. The flow visualization and the fluid mechanics measurements are used to explain the heat transfer phenomena. The synthetic jet has been found very effective in heat transfer enhancement. The heat transfer performances of synthetic jet impinging on a fin have been studied and analyzed under various conditions (e.g. various frequencies and various orifice shapes). The specific unsteady synthetic jet flows have been measured using a Laser Doppler Anemometer (LDA) and flow visualization has been taken to support the design and heat transfer measurements. The high noise emission of the actual synthetic jet has been found and a muffler has been designed to reduce the noise.

8.1 Heat Transfer

A mock-up synthetic jet is fabricated to investigate the synthetic jet cooling mechanism. The size of the scaled jet is 44 times that of the actual one. Consequently, the frequency of the mock-up jet is $1/44^2$ the actual frequency, which makes the scaled jet easier to operate and realize. The synthetic jet is impinging flow on a fin and the average heat transfer coefficient over the fin is measured. It is found that the heat transfer

coefficient increases almost linearly with increases of operating frequency of the synthetic jet, which makes the frequency an important parameter in designing synthetic jets for cooling. A high frequency (2700 Hz) jet is able to provide a heat transfer coefficient of 650 W/m^2K. Synthetic jets with two circular orifices provide the highest heat transfer performance among all orifice geometries studied (square, two square, circular, two circulars, slot, two slots, and star shape). The cases with different orifice shapes kept the same total orifice area and operating conditions. The case with two circular orifices is able to provide high heat transfer performance on both the fin tip region and the fin side wall region of a heat exchanger cooling channel.

Using numerical simulation, the heat transfer performance of synthetic jet impinging flow combined with a channel flow was studied. The synthetic jet flow impinged on the cooling fin while the channel flow is perpendicular to the jet impinging flow. The numerical simulation is realized by the commercial software ANSYS Fluent and has been validated by comparing with experiment. It was found that the heat transfer performance in the fin tip region was influenced significantly by the synthetic jet impinging flow while channel flow had little effect in this region. A maximum heat transfer enhancement of 400% synthetic jets was found. The channel flow was found to be more effective in cooling the fin side walls. Synthetic jets were not able to penetrate much further along the fins from the tips and have very little effect on the fin side walls. The heat transfer increase in the fin tip wall region by the synthetic jets is less than 10%. Synthetic jets are more effective in cooling if they are close to the surface.

8.2 Fluid Mechanics

Flow visualization of the unsteady synthetic jet flow is documented. The flow characteristics and development of synthetic jet impinging flow are clearly seen. When the diaphragm of the synthetic jet starts to push flow out of the orifice, a starting vortex is found near the orifice at the first quarter of total cycle. When the diaphragm continues to move towards the orifice, the vortex is found to move downstream by entraining and enrolling surrounding air at the same time (at the second quarter of total cycle). Finally, these vortices dissipate and the entire flow field is quiescent when the diaphragm is moving backwards from the orifice and draws flow into the orifice during the last two quarters of the cycle. Because the sink flow is much weaker than the impinging jet flow and it has little effect on the flow field far from the orifice. Flow visualization of the two-slot synthetic jet showed that the starting vortices from the two slots are toward inclined each other, induce one another and finally merge together as the vortices are move downstream. The closer the two slots are, the nearer to the orifice the merging point is. However, when the two slots are too far away the two flows will not affect each other and will move downstream independently.

A Laser Doppler Velocimetry (LDV) system is used to make detail velocity measurements of the synthetic jet impinging flow. The ensemble-averaged velocities and the Root Mean Square (RMS) velocities are used to capture the flow characteristics. In the core region, the ensemble-averaged velocities are at a high level while the RMS velocities are at a low level. In the shear layer region, the impinging flow out of the orifice starts to roll up the quiescent surrounding flow and form vortices that make the

velocity fluctuations increase. However, in the region far away from the orifice, magnitudes of the ensemble-averaged velocities and the RMS velocity fluctuations decrease, due to turbulence dissipation. In the region far away from the centerline, the flow domain is relatively quiescent. Both ensemble-averaged velocities and RMS velocity fluctuations in the far field are at a lower level compared to other regions.

8.3 Noise

The actual synthetic jets driven by piezoelectric stacks are found to be very effective in heat transfer enhancement. However, high noise emission levels are found by a measuring with a microphone. They are due to the high vibrational frequencies. The sound pressure levels increase linearly with input voltage to the piezoelectric actuator and with operating frequency. The noise level can go as high as 90 dB when the synthetic jets are operating at 1250 Hz. By applying a Fast Fourier Transform (FFT) analysis, the acoustic energy is found. It concentrates in narrow ranges at several specific frequencies that are integer multiples of the operating frequency of the active device drives. Almost 80% of the total acoustic energy is in a narrow band about the operating frequency.

A circular expansion chamber, one of several candidate muffler designs, is used for noise reduction based on the acoustic characteristics of the synthetic jet. The muffler is able to provide significant noise reduction at specific frequencies that can be predicted by a numerical model. The numerical model is used to optimize the muffler to provide the largest noise reduction. Several optimal muffler lengths have been found using this method. Based on the optimization results, a muffler is fabricated with an expansion ratio of 6 and a length of 51mm (two inches). The acoustic measurement showed that the

muffler is able to decrease the noise level form 83 dB to 63 dB. In the final cooling configurations, the mufflers are able to reduce the noise level from 91 dB to 65 dB with four piezoelectric stacks operating at about 800 Hz.

References

[1] G.E. Moore, Cramming more components onto integrated circuits, Proceedings of the IEEE, Volume 86, Issue 1(1965) 114-117.

[2] E. Stanford, Power Delivery Challenges in Computer Platforms, Intel, 2006.

[3] NEMI Technology Roadmaps, 2002

[4] Lasance, C. J. M., The Need for a Change in Thermal Design Philosophy, Electronics Cooling, 1 (1995), 2, pp. 24-26

[5] S.S. Anandan, V. Ramalingam, Thermal Management of Electronics: A Review of literature, Thermal Science 12 (2008) 5-26.

[6] T.A. Shedd, A.G. Pautsch, Spray impingement cooling with single- and multiple-nozzle arrays. Part II: Visualization and empirical models, International Journal of Heat and Mass Transfer, 48(15) (2005) 3176-3184.

[7] M. Fabbri, V.K. Dhir, Optimized Heat Transfer for High Power Electronic Cooling Using Arrays of Microjets, Journal of Heat Transfer, 127(7) (2005) 760-769.

[8] S. Toda, A study of mist cooling, Heat Transfer: Japanese Research, 1 (1972) 39-50.

[9] C. Bonacina, G. Comini, S. Del Giudice, Evaporation of atomized liquid on hot surfaces, Letters in Heat and Mass Transfer, 2(5) (1975) 401-406.

[10] B. Elison, B.W. Webb, Local heat transfer to impinging liquid jets in the initially laminar, transitional, and turbulent regimes, International Journal of Heat and Mass Transfer, 37(8) (1994) 1207-1216.

[11] K.A. Estes, I. Mudawar, Correlation of sauter mean diameter and critical heat flux for spray cooling of small surfaces, International Journal of Heat and Mass Transfer, 38(16) (1995) 2985-2996.

[12] Y. Pan, B.W. Webb, Heat Transfer Characteristics of Arrays of Free-Surface Liquid Jets, Journal of Heat Transfer, 117(4) (1995) 878-883.

[13] K. Oliphant, B.W. Webb, M.Q. McQuay, An experimental comparison of liquid jet array and spray impingement cooling in the non-boiling regime, Experimental Thermal and Fluid Science, 18(1) (1998) 1-10.

[14] M. Fabbri, S. Jiang, V.K. Dhir, A Comparative Study of Cooling of High Power Density Electronics Using Sprays and Microjets, Journal of Heat Transfer, 127(1) (2005) 38-48.

[15] L. Lin, R. Ponnappan, Heat transfer characteristics of spray cooling in a closed loop, International Journal of Heat and Mass Transfer, 46(20) (2003) 3737-3746.

[16] M. Visaria, I. Mudawar, Theoretical and experimental study of the effects of spray inclination on two-phase spray cooling and critical heat flux, International Journal of Heat and Mass Transfer, 51(9-10) (2008) 2398-2410.

[17] M. Visaria, I. Mudawar, Application of Two-Phase Spray Cooling for Thermal Management of Electronic Devices, Components and Packaging Technologies, IEEE Transactions on, 32(4) (2009) 784-793.

[18] A.G. Pautsch, T.A. Shedd, Spray impingement cooling with single- and multiple-nozzle arrays. Part I: Heat transfer data using FC-72, International Journal of Heat and Mass Transfer, 48(15) (2005) 3167-3175.

[19] J. R. Thome, State of the Art Overview of Boiling and Two Phase Flows in Microchannels, Heat Transfer Engineering, 27(9) (2006) 4-19

[20] M. B. Bowers, I. Mudawar, Two Phase Electronic Cooling Using Mini Channel and Micro Channel Heat Sinks: Part 1-Design Criteria and Heat Diffusion Constraints, Journal of Electronic Packaging, 116 (1994) 290-297

[22] M. B. Bowers, I. Mudawar, Two Phase Electronic Cooling Using Mini Channel and Micro Channel Heat Sinks: Part 2-Flow Rate and Pressure Drop Constraints, Journal of Electronic Packaging, 116 (1994) 298-305

[23] I.Mudawar, Two Phase Microchannel Heat Sinks: Theory, Applications and Limitations, Journal of Electronic Packaging, 133 (2011) 041002

[24] K. Adamiak, A. Mizuno, M. Nakano, Electrohydrodynamic flow in optoelectrostatic micropump: experiment versus numerical simulation, IEEE Transactions on Industry Applications 45 (2009) 615-622.

[25] V. Singhal, S.V. Garimella, A. Raman, Microscale pumping technologies for microchannel cooling systems, Applied Mechanics Reviews 57 (2004) 191-221.

[26] P. Dixit, N. Lin, J.M. Miao, W.K. Wong, T.K. Choon, Silicon nanopillars based 3D stacked microchannel heat sinks concept for enhanced heat dissipation applications in MEMS packaging, Sensors and Actuators A Physical 141 (2008) 685-694.

[27] L.N. Jiang, J. Mikkelsen, J.M. Koo, D. Huber, S.H. Yao, L. Zhang, P. Zhou, J.G. Maveety, R. Prasher, J.G. Santiago, T.W. Kenny, K.E. Goodson, Closed-loop electroosmotic microchannel cooling system for VLSI circuits, IEEE Transactions on Components and Packing Technologies 25 (2005) 347-355.

[28] J. Schutze, H. Ilgen, W.R. Fahrner, An integrated micro cooling system for electronic circuits, IEEE Transactions on Industrial Electronics 48 (2001) 281-285.

[29] P. Dixit, N. Lin, J. Miao, W.K. Wong, K.C. Teo, Concept and analytical analysis of silicon micro/nanopillars based 3-D stacked microchannel heat sink for advanced heat dissipation applications, in: 2007 Electronic Components and Technology Conference (2007) 1149-1154. [30] S.V. Garimella, Advances in mesoscale thermal management technologies for microelectronics, Microelectronics Journal 37 (2006) 1165-1185.

[31] C.H. Amon, S.C. Yao, C.F. Wu, C.C. Hsieh, Microelectromechanical system-based evaporative thermal management of high heat flux electronics, Journal of Heat Transfer-Transactions of the ASME 127 (2005) 66-75.

[32] E. Baird, K. Mohseni, Digitized heat transfer: a new paradigm for thermal management of compact micro systems, IEEE Transactions on Components and Packaging Technologies 31 (2008) 143-151.

[33] T. Acikalin, S.V. Garimella, A. Ranman, and J. Petroski, Characterization and optimization of the thermal performance of miniature piezoelectric fans, International Journal of Heat and Fluid Flow Vol. 8 (2006) 806-820.

[34] M. Kimber, S.V. Garimella, and A. Raman, Local Heat Transfer Coefficients Induced by Piezoelectrically Actuated Vibrating Cantilevers, ASME Journal of Heat Transfer Vol. 129 (2007) 1168-1176.

[35] K. Kimber and S.V. Garimella, Measurement and Prediction of the Cooling Characteristics of a Generalized Vibrating Piezoelectric Fan, International Journal of Heat and Mass Transfer 52 (2009) 4470-4478.

[36] K. Kimber and S.V. Garimella, Cooling Performance of Arrays of Vibrating Cantilevers, ASME Journal of Heat Transfer Vol. 131 (2009) 1401-1408.

[37] S.-F. Liu, R.-T. Huang, W.-J. Shen, and C.-C. Wang, Heat Transfer by a

Piezoelectric Fan on a Flat Surface Subject to the Influence of Horizontal/Vertical Arrangement, International Journal of Heat and Mass Transfer Vol. 52 (2009) 2565-2570.

[38] T. Acikalin, S. V. Garimella, "Analysis and Prediction of the Thermal Performance of Piezoelectrically Actuated Fans", Heat Transfer Engineering, 30(6): 487-498, 2009

[39] Cien-Nan Lin, Analysis of Three-Dimensional Heat and Fluid Flow induced by Piezoelectric Fan, International Journal of Heat and Mass Transfer 55 (2012) 3043-3053

[40] H. K. Ma, H. C. Su, C. L. Liu, W. H. Ho, Investigation of a Piezoelectric fan Embedded in a Heat Sink, International Communications in Heat and Mass Transfer 39 (2012) 603-609

[41] T. Y. Kim, Dong-Kwon Kim, S. J. Kim, Scroll heat sink: A Novel Heat Sink with the Moving Fins inserted between the Cooling Fins, International Journal of Heat and Mass Transfer, 51 (2008) 3267-3274

[42] J. Kim, S. J. Kim, Heat Transfer Characteristics of a Centrifugal Heat Sink, International Journal of Heat and Mass Transfer 56 (2013) 188-196

[43] J. M. Allison, W. L. Staats, M. McCarthy, D. Jenicek, A. K. Edoh, J. H. Lang, E. N. Wang, J. G. Brisson, Enhancement of Convective Heat Transfer in an Air Cooled Heat Exchanger using Interdigitated Impeller Plates, International Journal of Heat And Mass Transfer 54 (2011) 4549-4559

[44] T. Yeom, T. W. Simon, L. Huang, M. North, T. Cui, "Piezoelectric Translational Agitation for Enhancing Forced-Convection Channel-Flow Heat Transfer," International Journal of Heat and Mass Transfer 55 (2012) 7398-7409

[45] Y. Yu, T. W. Simon, S. Agrawal, M. North, T. Cui, "A Computational Study of Active Heat Transfer Enhancement of Air Cooled Heat Sinks by Actuated Plates,"

Proceedings of ASME International Mechanical Engineering Congress and Exposition, IMECE 64526, Denver, USA, 2011

[46] Y. Yu, T. W. Simon, M. Zhang, T. Yeom, M. North, T. Cui, " Enhancing Heat Transfer of Air Cooled Heat Sinks using Piezoelectrically driven Agitators and Synthetic Jets," Proceedings of ASME International Mechanical Engineering Congress and Exposition, IMECE 64544, Denver, USA, 2011

[47] T. Yeom, T. W. Simon, Y. Yu, M. North, T. Cui, "Convective Heat Transfer Enhancement on a Channel Wall with a High Frequency, Oscillating Agitator," Proceedings of ASME 154 International Mechanical Engineering Congress and Exposition , IMECE 64379, Denver, USA,2011

[48] T. Yeom, T. W. Simon, Y. Yu, M. Zhang, S. Agrawal, L. Huang, T. Zhang, M. North. T. Cui, " An Active Heat Sink System with Piezoelectric Translational Agitators and Micro Pin Fin Arrays" Proceedings of ASME International Mechanical Engineering Congress and Exposition, IMECE 88449, Houston, Texas, 2012

[49] Y. Yu, T. W. Simon, M. North, T. Cui, "Comparison of Heat Transfer Enhancement by Actuated Plates in Heat Sink Channels," Proceedings of the ASME 2012 Summer Heat Transfer Conference, HT 58280, Puerto Rico, USA, 2012

[50] S. Agrawal, T. Simon, M. North, T. Cui , "An Experimental Study on the Effects of Agitation on Forced-Convection Heat Transfer," ASME International Mechanical Engineering Congress and Exposition, Denver, Colorado, IMECE 2011-64558

[51] S. Agrawal, T. Simon , M. North, T. Cui , "An experimental study on the effects of agitation in generating flow unsteadiness and enhancing convective heat transfer," HT 2012-58273, ASME Summer Heat Transfer Conference, July 2012, Puerto Rico, USA

[52] Y. Yu, T. Simon, and T. Cui, A parametric study of heat transfer in an air-cooled heat sink enhanced by actuated plates, International Journal of Heat and Mass Transfer 64 (2013) 792-801

[53] A. Glezer, M. Amitay, Synthetic Jets, Annu. Rev. Fluids Mech. 34 (2002) 503-529.

[54] B.L. Smith, A. Glezer, The formation and evolution of synthetic jets, Physics of Fluids, 10 (1998) 2281-2297.

[55] B.L. Smith, A. Glezer, Jet vectoring using synthetic jets, J. Fluid Mech. 458 (2002) 1-34.

[56] R. Holman, Y. Utturkar, Formation Criterion for Synthetic Jets, AIAA Journal 43 (2005) 2110-2116.

[57] Y. utturkar, R. Holman, R. Mittal, B. Carroll, M. sheplak, L. Cattafesta, 41st Aerospace Sciences Meeting & Exhibit (2003) 1-9.

[58] M. Chaudhari, B. Puranik, A. Agrawal, Heat transfer characteristics of synthetic jet impingement cooling, International Journal of Heat and Mass Transfer 53 (2010) 1057-1069

[59] M. Chaudhari, B. Puranik, A. Agrawal, Frequency response of a synthetic jet cavity, Experimental Thermal and Fluid Science 33 (3) (2009) 439-448.

[60] M. Chaudhari, B. Puranik, A. Agrawal, Effect of orifice shape in synthetic jet based impingement cooling, Experimental Thermal and Fluid Science 34 (2010) 246-256.

[61] M. Chaudhari, B. Puranik, A. Agrawal, Multiple orifice synthetic jet for improvement in impingement heat transfer, International Journal of Heat and Mass Transfer 54 (2011) 2056-2065.

[62] M. Chaudhari, B. Puranik, A. Agrawal, Heat Transfer Analysis in a Rectangular Duct Without and With Cross-Flow and an Impinging Synthetic Jet, IEEE TRANSACTIONS ON COMPONENTS AND PACKAGING TECHNOLOGIES, Volume 33, Issue 2 (2010) 488-497.

[63] A. Pavlova, M. Amitay, Electronic Cooling Using Synthetic Jet Impingement, Journal of Heat Transfer, 128 (2006) 897-907.

[64] J. Garg, M. Airk, S. Weaver, T. Wetzel, S. Saddoughi, Journal of Electronic Packaging, 127 (2005) 503-511.

[65] Y. Utturkar, M. Arik, C. E. Seeley, M. Gursoy, An Experimental and Computational Heat Transfer Study of Pulsating Jets, Journal of Heat Transfer, 130 (2008) 062201-1~062201-10.

[66] M. Arik, Local Heat Transfer Coefficients of a High-Frequency Synthetic Jets during Impingements Cooling over Flat Surfaces, Heat Transfer Engineering, 29 (9) (2008) 763-773.

[67] M. Arik, An investigation and feasibility of impingement heat transfer and acoustic abatement of meso scale synthetic jets, Journal of Applied Thermal Engineering 27 (2007) 1483-1494.

[68] Y. Wang, G. Yuan, Y. Yoon, M. G. Allen, S. Bidstrup, Active Cooling Substrates for Thermal Management of Microelectronics, IEEE TRANSACTIONS ON COMPONENTS AND PACKAGING TECHNOLOGIES, Volume 28, Issue 3 (2005) 477-483.

[69] Y. Wang, G. Yuan, Y. Yoon, M. G. Allen, S. Bidstrup, Optimization of Synthetic Jet Fluidic Structures in Printed Wiring Boards, Journal of Electronic Packaging, 128 (2006) 353-359.

[70] D. B. Go, R. K. Mongia, Experimental Studies on Synthetic Jet Cooling Enhancement for Portable Platforms, 11th IEEE Intersociety Conference on Thermal and Thermomechanical Phenomena in Electronic Systems, I-THERM (2008) 528-536.

[71] A. Qayoum, V. Gupta, P.K. Panigrahi, K. Muralidhar, Perturbation of a laminar boundary layer by a synthetic jet for heat transfer enhancement, International Journal of Heat and Mass Transfer, 53 (2010) 5035-5037.

[72] P.Valiorgue, T.Persoons, A. McGuinn, D.B. Murray, Heat transfer mechanisms in an impinging synthetic jet for a small jet-to-surface spacing, Experimental Thermal and Fluid Science 33 (2009) 597-603.

[73] M.B. Gillespie, W.Z. Black, C. Rinehart, A. Glezer, Local Convective Heat Transfer From a Constant Heat Flux Flat Plate Cooled by Synthetic Air Jets, Journal of Heat Transfer 128 (2006) 990-1000.

[74] R. Mahalingam, Modeling of Synthetic Jet Ejectors for Electronics Cooling, 23rd Annual IEEE Semiconductor Thermal Measurement and Management Symposium (2007) 196-199.

[75] R. Mahalingam, N. Rumigny, A. Glezer, Thermal Management Using Synthetic Jet Ejectors, IEEE TRANSACTIONS ON COMPONENTS AND PACKAGING TECHNOLOGIES, Volume 27, Issue 3 (2004) 439-444.

[76] R. Mahalingam, A. Glezer, Design and Thermal Characteristics of a Synthetic Jet Ejector Heat Sink, Journal of Electronic Packaging, Transactions of the ASME 127 (2005) 172-177.

[77] D. Jagannatha, R. Narayanaswamy, T.T. Chandratilleke, Analysisi of a Synthetic Jet-Based Electronic Cooling Module, Numerical Heat Transfer, Part A 56 (2009) 211-229.

[78] K. Navaratnam, D. Lee, S. Parameswaran, Application of a Novel Moving-Grid Methodology to Model the Interaction of a Synthetic Jet with a Turbulent Boundary Layer, Numerical Heat Transfer, Part B 49 (2006) 105-123.

[79] M. Dghim, M.B. Chiekh, B.N. Sassi, CFD modeling of a Synthetic Jet Actuator, Int. Symp. On Convective Heat and Mass Transfer in Sustainable Energy, Tunisia (2009).

[80] Y. Zhou, B. Wang, Research on Fluidic Dynamic Characteristics of the Piezoelectric Synthetic Jet Actuator, Journal of Intelligent Material Systems and Structures 19 (2008) 351-357.

[81] T.T Chandratilleke, D. Jagannatha, R. Narayanaswamy, Performance Analysis of a Synthetic Jet-microchannel Hybrid Heat Sink for Electronic Cooling, 11th Electronics Packaging Technology Conference (2009) 630-635.

[82] N. Beratlis, M.K. Smith, Optimization of Synthetic Jet Cooling for Microelectronics Applications, Annual IEEE Semiconductor Thermal Measurement and Management Symposium (2003) 66-73.

[83] R.C. Behera, P. Dutta, K. Srinivasan, Numerical Study of Interrupted Impinging Jets for Cooling of Electronics, IEEE TRANSACTIONS ON COMPONENTS AND PACKAGING TECHNOLOGIES, Volume 30, Issue 2 (2007) 275-284.

[84] Y. Wang, G.Yuan, Y. Yoon, M.G. Allen, S.A. Bidstrup, Large eddy simulation (LES) for synthetic jet thermal management, International Journal of Heat and Mass Transfer 49 (2006) 2173-2179.

[85] D.W. Gerlach, D. Gerty, R. Mahalingam, Y.K. Joshi, A. Glezer, A Modular Stackable Concept for Heat Removal From 3-D Stacked Chip Electronics by Interleaved Solid Spreaders and Synthetic Jets, IEEE TRANSACTIONS ON ADVANCED PACKAGING Volume 32, Issue 2 (2009) 431-439.

[86] N. Erbas, O. Baysal, Micron-Level Actuators for Thermal Management of Microelectronic Devices, Heat Transfer Engineering 30 (2009) 138-147.

[87] V. Timchenko, J. Reizes, E. Leonardi, An evaluation of synthetic jets for heat transfer enhancement in air cooled micro-channels, International Journal of Numerical Methods for Heat & Fluid Flow, Volume 17, Issue 3, (2006) 263 – 283.

[88] V. Timchendo, J.A. Reizes, E. Leonardi, F. Stella, Heat Transfer Enhancement using Synthetic Jet Actuators in Forced Convection Water Filled Micro-Channels, Proceedings of the 3rd IASME/WSEAS Int. Conf. on HEAT TRANSFER, THERMAL ENGINEERING AND ENVIRONMENT, Corfu, Greece, (2005) 294-299.

[89] V. Timchendo, J.A. Reizes, E. Leonardi, F. Stella, Synthetic Jet forced Convection Heat Transfer Enhancement in Micro-Channels, International Journal of Numerical Methods for Heat & Fluid Flow, Volume 17 (2007) 263-83.

[90] Lyon, R.H. and Bergles, A.E., 2006, "Noise and Cooling in Electronics Packages," IEEE Transactions on Components and Packaging Technologies, Vol. 29, No. 3, pp. 535-542.

[91] Seeley C.E., Arik M., Hedeen R., Utturkar Y., Wetzel T., Shih M., "Coupled

acoustic and heat transfer modeling of a synthetic jet," in: 47th AIAA/ASME/ASCE/AHS/ASC Structures, Structural Dynamics, and Materials Conference, 1-4 May 2006, Newport, Rhode Island.

[92] Munjal, M. L. "Acoustics of ducts and mufflers," John Wiley & Sons (2002).

[93] Miles J., "The Reflection of Sound due to a Change in Cross Section of a Circular Tube," Journal of the Acoustical Society of America, Vol. 16, pp. 14-19, (1944).

[94] EI-Sharkawy A. I., and Nayfeh A. H., "Effect of an expansion chamber on the propagation of sound in circular ducts," Journal of the Acoustical Society of America, Vol. 63, pp. 667-674, (1978).

[95] Kim Y., and Kang S., "Green's solution of the acoustic wave equation for a circular expansion chamber with arbitrary locations of inlet, outlet port, and termination impedance," Journal of the Acoustical Society of America, Vol. 94, pp. 473-490, (1993).

[96] Selamet A., Radavich P.M., "The effect of length on the acoustic attenuation performance of concentric expansion chamber : an analytical, computational and experimental investigation", Journal of Sound and Vibration, Vol 201(4), pp. 407-426, (1997).

[97] Denia F.D., Albelda J., and Fuenmayor F.J., "Acoustic behavior of elliptical chamber mufflers", Journal of Sound and Vibration, Vol. 241(3), pp. 401-421, (2001).

[98] Denia F.D., and Selamet A., "Acoustic behavior of short elliptical chambers with end central inlet and end offset or side outlet", Journal of Sound and Vibration, Vol. 245(5), pp. 953-959, (2001).

[99] ANSYS FLUENT 13, Ansys, Inc., Canonsburg, Pennsylvania, USA.

[100] Kline S.J., McClintock F.A., 1953, "Describing Uncertainties in Single Sample

Experiments," Mech. Eng. (Am. Soc. Mech. Eng.), 75, pp. 3-8.

[101] Yeom T., Simon T. Zhang M., North M., and Cui T., "High frequency, large displacement, and low power consumption piezoelectric translational actuator based on an oval loop shell", Sensors and Actuators A: Physical, 176, pp. 99-109, (2012).

[102] Zhang M., Yeom T., Yu Y., Huang L., Simon T., North M., Cui T., " Development of Synthetic Jet Arrays for Heat Transfer Enhancement in Air-Cooled Heat Sinks for Electronics Cooling", in: Proceedings of ASME 2012 Summer Heat Transfer Conference, HT2012-58092, July 8-12, Rio Grande, Puerto Rico, USA, 2012.

[103] Huang L., Simon T., Zhang M., Yu Y., North M., Cui T., "Heat Transfer Enhancement By Synthetic Jet Arrays In Air-Cooled Heat Sinks For Use In Electronics Cooling", in: Proceedings of ASME 2012 Summer Heat Transfer Conference, HT2012-58278, July 8-12, Rio Grande, Puerto Rico, USA, 2012.